A Diagnostic Study of Chlorine X-Ray Line Emission from the COMPASS-D Tokamak.

Ian Mark Melnick

Submitted for the Degree of PhD

University College London

September 1995

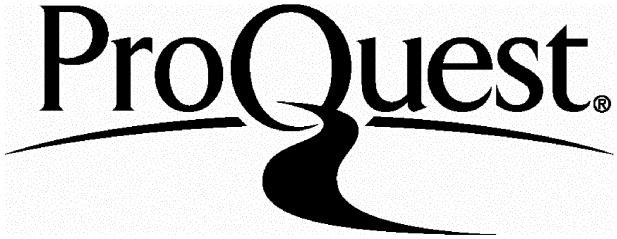

Abstract

A high resolution Johann spectrometer has been used to observe the spectrum of He- like Cl and its satellites ($4.4 - 4.5\mathring{A}$) on the COMPASS-D tokamak at Culham Laboratory. This narrow spectral region is a rich source of plasma diagnostic information. The spectra obtained have been fitted with Voigt profiles and interpreted in terms of plasma parameters. The core temperatures of the electron and ion fluids have been derived from the intensity ratio of the dielectronic satellite line, k, to the He- like resonance line, w, and from Doppler broadening of spectral lines respectively. Heat transport coefficients have been estimated from the measured temperatures and are used to explain temperature differences between the two fluids. The impurity ion diffusion coefficient, D, has been derived from the intensity ratio of the Li- like inner shell excitation satellite line, q, to the w line. The values obtained are in good agreement with those derived from laser ablation experiments. At high temperatures ($T_e > 800eV$) this ratio and the G (ratio of the intercombination lines ($x + y + z$) to the w line) and R ($\frac{z}{x+y}$) ratios are close to coronal predictions, but at lower temperatures there are large departures from coronal values. This indicates an increase in the Li- like population compared with the He- like population and an enhancement of the triplet levels over the singlet levels due to inner shell ionisation from the Li- like ground state. Absolute calibration of the spectrometer sensitivity has been used to measure the continuum and line intensities and these have been modelled in terms of impurity concentrations. The intensity of the w line increases during ELM free H-modes consistent with weak impurity accumulation. Core toroidal rotation has been measured during ELM free H-modes and mode-locking experiments from Doppler shifts of spectral lines. In both cases a change of rotation of $\approx 20km/s$ is seen in the ion drift direction at the onset of the H-mode or mode-lock. In the absence of an external momentum source these changes are accounted for by pressure gradient and viscous forces.

Contents

List of Figures

List of Tables

Acknowledgements

There are many people I must thank for their valuable contributions, advice, help and friendship over the past four years without which this thesis would not have been possible.

I must thank my supervisors Dr NJ Peacock (Culham) and Dr ACH Smith (UCL) for their guidance and help throughout this project. This work was made possible by a CASE studentship for which I must thank both the EPSRC and UKAEA Govt. division.

The starting point for this work was a ready built spectrometer which I must thank Jim Dunn for, and Robin Barnsley for help with setting up the spectrometer on COMPASS and focussing crystals. Thanks to Tony Abbey and Stephen Lea of Leicester University for the CCD electronics and software, and to Nick Nelms for sorting us out when we encountered any problems.

There are many people in Culham I must mention and thank for their help, please forgive me if I leave any one out. Martin Dunstan for technical support, Robert Stephens and Robbie McStay for electronics support, Martin O Mullane and Ivor Coffey for help with atomic physics and codes, Nick Hawkes, Paddy Carolan, Steve Fielding and Ruth Bamford for many useful discussions on rotation, transport etc, Sue Manhood and Nick Benterman for computer support, Ash Patel and Mary Singleton for their much valued assistance and of course thanks to the whole COMPASS team.

The final thankyou must go to my parents for all their support and encouragement.

Thesis Background and Objectives

A versatile high resolution Johann x-ray spectrometer was designed and built by Jim Dunn and Robin Barnsley of Leicester University [Dunn 1990]. One of the key features of the spectrometer was a novel crystal bending jig designed to be able to bend crystals to a wide range of radii of curvature. The use of this spectrometer for measurements made on tokamaks (DITE, UKAEA Culham Laboratory), beam foil sources (Oxford Clarendon Laboratory) and laser produced plasmas (Rutherford Appleton Laboratory) is reported on by Jim Dunn in his PhD thesis [Dunn 1990]. These measurements were made using photographic film. This work was carried out between 1982 and 1990.

The film was subsequently replaced by a large area CCD array in order to obtain time resolved measurements. The complete system was tested on the JET tokamak (Joint European Torus at Culham) for a single day of operations in 1992 [Abbey et al 1992].

The atomic physics codes of Queens University Belfast [Keenan et al 1987] were tested on spectra obtained from JET and are reported on by Ivor Coffey in his PhD thesis [Coffey 1993]. This includes interpretation of Cl XVI spectra obtained from the Johann spectrometer on its JET test.

The instrument in its present form was then moved to the COMPASS-D tokamak (UKAEA Culham Laboratory) in 1992 with some minor modifications to comply with COMPASS-D conditions. The spectrometer has been used as a plasma diagnostic on COMPASS-D and the results obtained are reported in this thesis.

The spectrometer has been used to view the spectrum of He- like Cl on COMPASS-D. Plasma diagnostic information is obtained from Doppler measurements of spectral lines, from the atomic physics underlying the spectral line intensities and from absolute intensity measurements. COMPASS-D conditions are ideal for measurements of Cl XVI as the relatively low electron and ion temperatures allow well resolved and relatively intense satellite lines.

The aim of this thesis is to maximise the diagnostic potential of the spectrometer by taking full advantage of the spectral and temporal resolution of the spectrometer and the atomic physics of the observed spectra and their interpre-

tation in terms of plasma heat and particle transport. Spectra are fitted with Voigt profiles to take account of thermal broadening and instrumental effects, the parameters returned from the fit are used to obtain the relevant diagnostic information. A cross-correlation technique is proposed for spectral analysis when photon statistics are not sufficient for spectral fitting.

Chapter 1 contains a brief introduction to COMPASS-D and tokamaks in general, plasma radiation and plasma diagnostics and also a short introduction to Bragg spectroscopy.

The spectrometer is described in chapter 2. The various spectrometer elements are described and an estimation is made of the instrument profile and resolution. The data analysis procedures are also described.

The relevant atomic physics of He- like spectra and their plasma diagnostic potential are given in chapter 3. The detailed spectral fitting procedure is also described here.

Results are presented in chapters 4-6. Chapter 4 contains results of ion and electron temperature measurements and their interpretation in terms of heat transport. Line ratio measurements are made and departures from coronal equilibrium are explained in terms of impurity ion transport.

The results presented in chapter 5 are from absolute calibration of the spectrometer. Absolute measurements are made of both continuum and line radiation. Modelling of the continuum is used to differentiate between free-free and free-bound radiation. Possible evidence of impurity accumulation is speculated on from the line intensity measurements.

Chapter 6 describes plasma toroidal rotation measurements. A background is given to plasma rotation and an estimation is made of the relative importance of the various driving terms of the core toroidal rotation.

A summary of the results and conclusions are presented in chapter 7.

The units used in this thesis are SI units except where otherwise stated, the unit of temperature used is eV. Symbols are defined as they are used. A list of symbols also appears as an appendix.

Chapter 1

Introduction

1.1 Tokamaks

The tokamak, Russian acronym for TOroid KAmera MAgnit Katushka (toroidal magnetic chamber), is a toroidal device for the magnetic confinement of fusion plasmas. The plasma current I_p is induced by transformer action, the plasma itself acts as a single secondary coil. Confinement and stability are provided by toroidal and poloidal magnetic fields, the resultant field being helical. Figure 1.1 shows the magnetic field configuration of a tokamak. In a tokamak the ratio of the toroidal field strength to the poloidal field strength is $\frac{B_\phi}{B_\theta} \approx 10$.

The geometry of the tokamak is toroidal but for many calculations cylindrical geometry can be assumed as a first approximation.

Present day tokamak research is aimed towards achieving controlled nuclear fusion. The most favourable fusion reaction in terms of energy yield and temperature threshold is the deuterium (D) - tritium (T) reaction;

$$D + T \rightarrow {}^4He(3.56MeV) + n\ (14.03MeV). \tag{1.1}$$

Due to the high neutron flux rate and the resultant vessel contamination most tokamak research is carried out with deuterium plasmas. Cross sections for fusion reactions have been calculated by Gammow [Gammow 1938]. The total nuclear reaction cross section at low energy ($< 200keV$) is given by;

$$\sigma = \left(\frac{S}{E}\right) exp\left[-\frac{G}{E^{\frac{1}{2}}}\right]\ barns \tag{1.2}$$

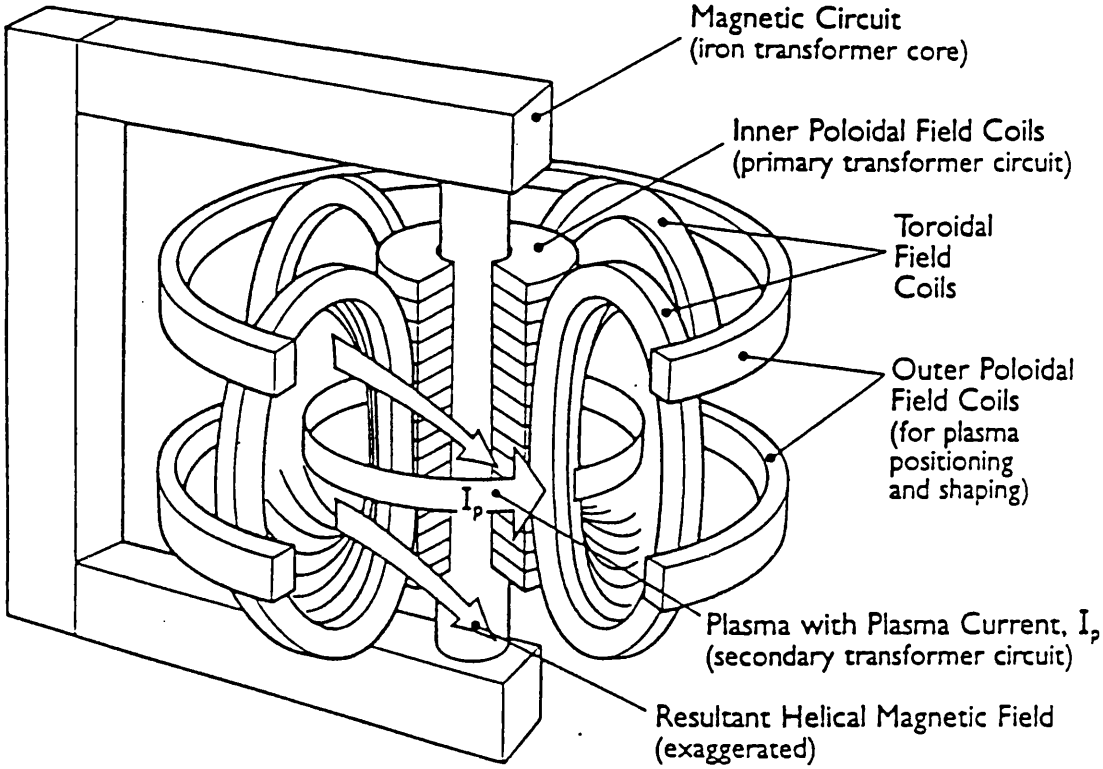

Figure 1.1: *The magnetic field configuration of a tokamak. The toroidal field is produced with toroidal field coils, the poloidal field is induced by the plasma current and the plasma is stabilised with additional poloidal field coils. The plasma current is induced by transformer action.*

where $S = 11000\ barn\ keV$ and $G = 34.4\ keV^{\frac{1}{2}}$ for a DT reaction, and $S = 53\ barn\ keV$ and $G = 31.4\ keV^{\frac{1}{2}}$ for a DD reaction ($1\ barn = 10^{-28}m^{-2}$). E is the relative particle energy. The reaction rate is the Maxwellian averaged cross section.

Ignition is defined as when the α particles produced by the fusion reaction fully compensate for the energy losses. It is achieved when the fusion triple product $n_i T_i \tau_E \geq 10^{22} m^{-3} skeV$ where n_i is the fuel ion density, T_i is the ion temperature and τ_E is the energy confinement time. This expression is obtained from a balance between the bremsstrahlung power loss from the plasma and the fusion power gain in the plasma [Lawson 1957].

Besides the main fuel ions there are impurity ions which enter the plasma due to reactions with the vessel wall. These greatly increase power losses from the plasma due to the emission of radiation. One of the main aims of tokamak research is in the field of impurity removal.

Temperature and density gradients exist between the hot reacting plasma core and the cooler plasma edge. In general the electron density gradient can be approximated by a parabolic expression;

$$n_e(r) = n_e(0)\left(1 - \frac{r}{a}\right)^n, \tag{1.3}$$

and the temperature gradient by;

$$T_e(r) = T_e(0)\left(1 - \left(\frac{r}{a}\right)^n\right)^n, \tag{1.4}$$

where $n_e(0)$ is the central electron density, $T_e(0)$ is the central electron temperature and a is the minor radius, $n \geq 2$. The impurities exist across these gradients in various ionisation stages from neutral and low ionisation stages at the edge to highly ionised and fully stripped at the centre. In some cases hollow density profiles have been measured, for example during H-modes using neutral beam heating on JET [JET Team 1988].

1.1.1 The COMPASS-D Tokamak

The COMPASS-D tokamak (COMPact ASSembly) is a medium sized tokamak designed for the study of impurity and disruption control [Hayward et al 1989]. The major features are shown in Table 1.1. Additional heating and current drive are provided by electron cyclotron resonance heating and current drive (ECRH and ECCD) and by lower hybrid current drive (LHCD).

The vacuum vessel is made of Inconel. Wall conditioning techniques include frequent boronisation to reduce the oxygen content of the plasma and He glow discharges between plasma pulses. Typical plasma impurities include boron, carbon, oxygen and chlorine.

The shaping coils allow for different plasma configurations eg. circular, elliptical and single null x-point (SNX). There is also a versatile set of "error field" coils which can be used to produce many different magnetic field perturbations

and MHD modes. Instability studies on the COMPASS-D include the generation and subsequent removal of these modes.

Table 1.1: *COMPASS-D Parameters*

Parameter	Value
Major Radius (R)	0.557 m
Minor Radius (horizontal) (a)	0.232 m
Minor Radius (vertical) (b)	0.385 m
Aspect Ratio (SNX plasmas) ($\frac{R}{a}$)	3.28
Plasma Current (I_p)	100 - 200 kA
Toroidal Field (B_ϕ)	1 - 2 T
ECRH power	2 MW at 60 GHz
LHCD power	600 kW at 1.3 GHz
Plasma Duration	300 - 400 ms
Electron Density (n_e)	$8 \times 10^{18} - 1.2 \times 10^{20} m^{-3}$
Central Electron Temperature (ohmic) ($T_e(0)$)	500 - 1000 eV
Central Ion Temperature ($T_i(0)$)	100 - 400 eV
Energy Confinement Time (τ_E)	5 - 25 ms

1.2 Plasma Radiation

There are a number of atomic processes responsible for radiative power loss. These include line radiation due to radiative decay of an excited electron following ionisation and recombination processes and continuum radiation from recombination and bremsstrahlung. See [DeMichelis and Mattioli 1981, Isler 1984] for detailed reviews of plasma radiation. The most important ionisation process is electron impact ionisation;

$$X^Z + e \rightarrow X^{Z+1} + 2e. \tag{1.5}$$

An alternative is a two step process where the ion is first excited by electron impact excitation which is followed by autoionisation to stabilise the ion;

$$X^Z + e \rightarrow X^{Z*} + e \rightarrow X^{Z+1} + 2e. \tag{1.6}$$

For some ions, this is the dominant process [Isler 1984]. The rate coefficients for these ionisation and excitation mechanisms are functions of the collision cross section and the electron velocity and hence the electron temperature.

There are three recombination mechanisms; dielectronic, radiative and charge exchange. Dielectronic recombination is also a two step process involving electron impact. An ion captures an electron in a highly excited state and at the same time a bound electron is excited. The ion will usually stabilise itself by autoionisation, but in some cases will stabilise by radiative decay of one of the electrons followed by cascading of the other resulting in a recombined ion;

$$X^Z + e \rightarrow X^{(Z-1)**} \rightarrow X^{Z-1} + h\nu. \tag{1.7}$$

An energy level diagram of the process is shown for a typical He- like ion in figure 1.2.

Radiative recombination involves the capture of a free electron into a bound state which is followed by the emission of a photon. If the captured electron has energy E then the energy of the emitted photon will be $h\nu = E + \chi$ where χ is the ionisation energy of the bound state;

$$X^Z + e(E) \rightarrow X^{Z-1} + h\nu. \tag{1.8}$$

Dielectronic recombination results in line radiation whereas radiative recombination results in continuum radiation with a minimum energy equal to the ionisation potential.

Charge exchange recombination involves the exchange of electrons between neutral particles and ions. In general electrons from neutral hydrogen or deuterium are transferred to highly ionised ions;

$$X^Z + H_0 \rightarrow X^{Z-1} + H^+. \tag{1.9}$$

The total recombination rate is given by the sum of the three processes;

$$\alpha = \alpha^R + \alpha^D + \frac{n_0}{n_e}\alpha^{CX} \tag{1.10}$$

where n_0 is the neutral density. This form is chosen for the charge exchange recombination rate such that the total loss rate is given by;

$$\frac{dn_z}{dt} = -n_z n_e \alpha. \tag{1.11}$$

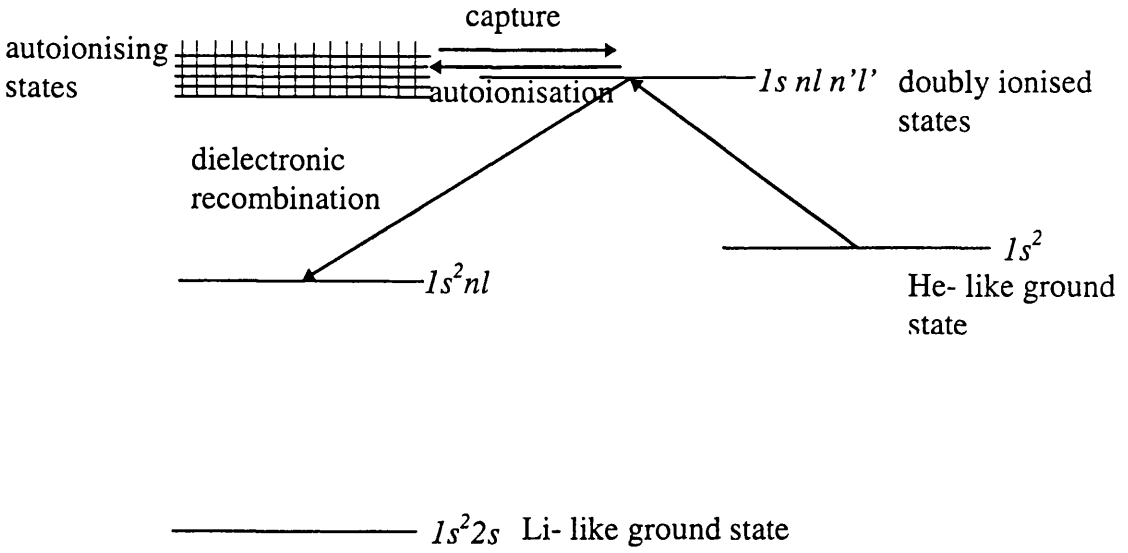

Figure 1.2: *The process of dielectronic recombination. A free electron is captured by an ion and simultaneously a bound electron is excited. The two electrons form a doubly excited state. The ion can either stabilise by autoionisation to a neighbouring level or by radiative decay to a level above the ground state of the recombined ion due to the presence of the spectator electron.*

For charge exchange alone the loss rate is given by;

$$\frac{dn_z}{dt} = -n_z n_0 \alpha. \tag{1.12}$$

The continuum radiation consists of two parts; radiative recombination (free - bound) and bremsstrahlung (free - free). Bremsstrahlung is due to the acceleration of electrons in the electric field of positively charged particles. The intensity is a function of electron temperature and density and of the effective charge state of the plasma; Z_{eff} (See chapter 5). Measurement of the absolute intensity of the bremsstrahlung thus gives a measure of the "purity" of the plasma. Bremsstrahlung covers the full spectral range, peaking at

$$\lambda = \frac{6200}{T_e}, \tag{1.13}$$

where λ is the wavelength in $\mathring{A}$ and T_e is the electron temperature in eV, for

typical tokamak conditions this is in the soft x-ray region.

1.2.1 Ionisation Equilibrium

In order to be able to interpret the emitted radiation from a plasma we require a knowledge of the populations of the various ionisation states of the impurity elements present in the plasma. The Boltzman distribution gives the ratio of the populations of two energy levels E_1 and E_2;

$$\frac{n_2}{n_1} = \frac{g_2}{g_1} e^{-\frac{E_2 - E_1}{kT}}, \tag{1.14}$$

where n_1 and n_2 are the populations of the two energy levels and g_1 and g_2 are the statistical weights. For a particular state of an ion, a partition function is used to calculate the population of that level as a fraction of the total population of that species. Thus for the j^{th} level of an ion;

$$\frac{n_j}{n} = \frac{g_j}{Q(T)} e^{-\frac{E_j}{kT}}, \tag{1.15}$$

where n is the total population of the species and $Q(T)$ is the partition function;

$$Q(T) = \sum_{j=0}^{\infty} g_j e^{-\frac{E_j}{kT}}. \tag{1.16}$$

If a Maxwellian distribution of the particles can be assumed, the partitition function for translational motion of a free particle is given by [Thorne 1988];

$$Q_t(T) = \frac{(2\pi mkT)^{\frac{3}{2}}}{h^3}. \tag{1.17}$$

In an ionisation process where an ion is ionised from a charge Z to charge $Z+1$ and a free electron is emitted, the general relation for the populations of the three species in equilibrium is;

$$\frac{N_e N_{Z+1}}{N_Z} = \frac{Q_e Q_{Z+1}}{Q_Z}, \tag{1.18}$$

where Q_e is the partition function of the electron. In this equation, total partition functions are used which are the product of the internal partition function (equation (1.16)) and the translational partition function for the free particle (equation (1.17)). The Saha equation is then obtained from the definitions of

the partition functions in equations (1.16) and (1.17). The translational partition functions of the ions Z and $Z+1$ are nearly equal as the masses are the same, these terms therefore cancel. The Saha equation is given by;

$$\frac{n_e n_{z+1}}{n_z} = \frac{2(2\pi mkT)^{\frac{3}{2}}}{h^3}\frac{g_{z+1}}{g_z} exp\left(\frac{-\chi_z}{T}\right), \tag{1.19}$$

where χ_z is the ionisation energy of the ions of charge z. The factor 2 comes from the two possible spin states of the electron.

The Saha equation is valid in cases of complete thermodynamic equilibrium ie. there is a Boltzman distribution of states, the velocities are Maxwellian and the radiation is at the black body level for the temperature of the system. This is rarely achieved in practice in either laboratory or astrophysical plasmas though it may be approached in stellar interiors.

In low density atomic plasmas there is a balance between collisional ionisation and radiative recombination as other terms become insignificant. Upward transitions are collisional and downward transitions are radiative. Using this model known as coronal equilibrium we obtain for the relative state populations;

$$\frac{n_z}{n_{z+1}} = \frac{\alpha_{z+1}}{S_z}, \tag{1.20}$$

where α is the recombination rate and S is the ionisation rate. As the density increases, collisional terms begin to dominate over radiative terms and the model breaks down. This model is adequate if the plasma is stable in time and if impurity transport is slow compared with ionisation and recombination times. In practice, tokamak plasmas are rarely stable in time and hence time dependent models become necessary.

A simple "zero dimensional" model is given by [Hulse 1983];

$$\frac{dn_z}{dt} = n_e\left[n_{z-1}S_{z-1} - n_z S_z - n_z\alpha_z + n_{z+1}\alpha_{z+1}\right] - \frac{n_z}{\tau_{imp}} + Q, \tag{1.21}$$

where τ_{imp} is the impurity confinement time and Q is a source / sink term. S and α can now change in time in response to plasma changes. The full set of coupled equations can then be solved to give the fractional abundance of each ionisation stage as a function of temperature for different values of τ_{imp}.

A more detailed one dimensional radial transport model which includes diffusion and convection can be used to model tokamak transport and forms the

basis of most transport codes eg. STRAHL [Behringer 1987];

$$\frac{dn_z}{dt} = -\frac{1}{r}\frac{\partial}{\partial r}(r\Gamma_z) + n_e\left[n_{z-1}S_{z-1} - n_z S_z - n_z\alpha_z + n_{z+1}\alpha_{z+1}\right], \qquad (1.22)$$

where Γ_z represents the particle flux density and is given by

$$\Gamma_z = -D\frac{\partial n_z}{\partial r} + \frac{r}{a}V n_z, \qquad (1.23)$$

where D is the particle diffusion coefficient and V is the convective velocity. Additional terms can be added in to take account of ion losses, recycling and other source / sink terms. Experimental results of D and V are found to be anomalously high (compared with transport theories), they are usually found empirically by fitting the results of a transport code to experimental data. A model generated by STRAHL [Behringer 1987] for the fractional abundance of Cl in COMPASS-D is shown in Figure 1.3. The main effects of transport are shifts of the emission peaks to higher temperatures than predicted by coronal equilibrium.

The diffusion coefficient D can also be predicted from the "zero dimensional" model by solution of the diffusion equation;

$$\frac{\partial n(r,t)}{\partial t} = \nabla.\left[D\nabla n(r,t)\right], \qquad (1.24)$$

which can be rewritten in cylindrical coordinates as

$$\frac{1}{r}\frac{\partial}{\partial r}\left(r\frac{\partial n}{\partial r}\right) + \frac{n}{D\tau_{imp}} = 0, \qquad (1.25)$$

and solved using a Bessel function to give

$$\tau_{imp} = \frac{a^2}{(2.4)^2 D}, \qquad (1.26)$$

where a is the plasma minor radius. This however ignores convection, which can be included with slight modification to the equation [Seguin 1983].

1.3 Tokamak Confinement

Tokamak heat and particle transport and confinement are described by neo-classical transport theory [Hinton and Hazeltine 1976]. Neoclassical transport

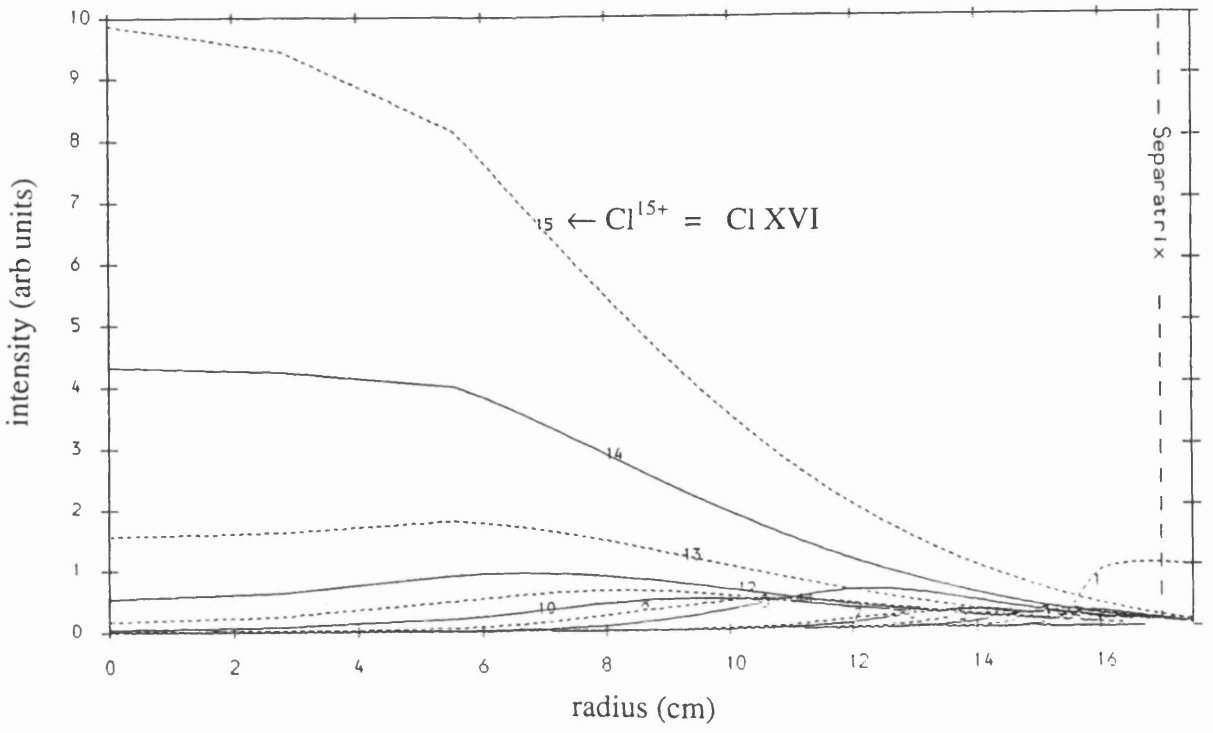

Figure 1.3: *The fractional abundance of the various ionisation stages of Cl as a function of radius in COMPASS-D,* $n_e(0) = 8 \times 10^{19} m^{-3}$ *and* $T_e(0) = 600eV$. *Plot generated from the STRAHL code [Behringer 1987].*

describes the effects of toroidal geometry on classical plasma transport. In practice heat and particle transport are found to be anomalously high. Electron energy confinement is reduced by two orders of magnitude [Wesson 1987]; the loss in ion energy confinement is less.

Improvements in confinement of a factor of ≈ 2 can be achieved in the H-mode (high confinement mode). The H-mode was first discovered in the ASDEX tokamak [Wagner et al 1982] in neutral beam heated plasmas, and has also been observed in radio frequency heated and ohmic plasmas [Osborne 1990]. COMPASS-D has achieved both Ohmic and ECRH H-modes [Fielding et al 1994]. The H-mode forms after the formation of a transport barrier at the plasma edge. The pressure gradients steepen across the transport barrier and flatten at the plasma centre. The transition to the H-mode from the L-mode (low confinement) is in general fast at the plasma edge ($< 100\mu s$). Improvement in the core confinement occurs on a time scale equivalent to the energy confinement time [Groebner 1993].

The electron density increases during an H-mode which can lead to a disruption, plasma radiation also increases as the density increases. The transport barrier can be breached by edge instabilities which halt the rise in the density, these instabilities being known as ELMs (edge localised modes). ELMs also reduce the energy confinement of the H-mode, but it still remains higher than the L-mode values.

H-modes are diagnosed by a spectroscopic measure of the intensity of H_α (or D_α) light which is a measure of bulk ion recycling at the vessel walls. At the onset of the H-mode, the H_α signal drops and then rises during ELMs. At the same time an increase is seen in the line average density and also in the plasma radiation.

1.4 Plasma Diagnostics

Information about plasma properties and behaviour can be obtained from many physical effects. Electromagnetic radiation is emitted across the entire spectrum; fields relating to the electromagnetic nature of the plasma can be measured, test particles and photons can be introduced and the resulting interaction with the plasma environment can be observed. Figure 1.4 shows the diagnostic systems used on COMPASS-D and what they measure. Here we shall describe a few of the diagnostics relevant to this work. For further discussion of plasma diagnostics see [Hutchinson 1987].

1.4.1 Magnetic Diagnostics

A time varying magnetic field passing through a loop of wire will induce a voltage across the ends of the wire. This simple technique is used in various forms to measure the electromagnetic fields and their effects such as current and voltage.

A Rogowski coil consists of a solenoidal loop wound poloidally around the torus (the solenoid is wound back on itself to cancel out the effects of currents passing through the coil). The plasma current in the torus induces a poloidal magnetic field which is measured by the Rogowski coil, the plasma current can then be derived from a combination of Faraday's law and Ampère's law. The

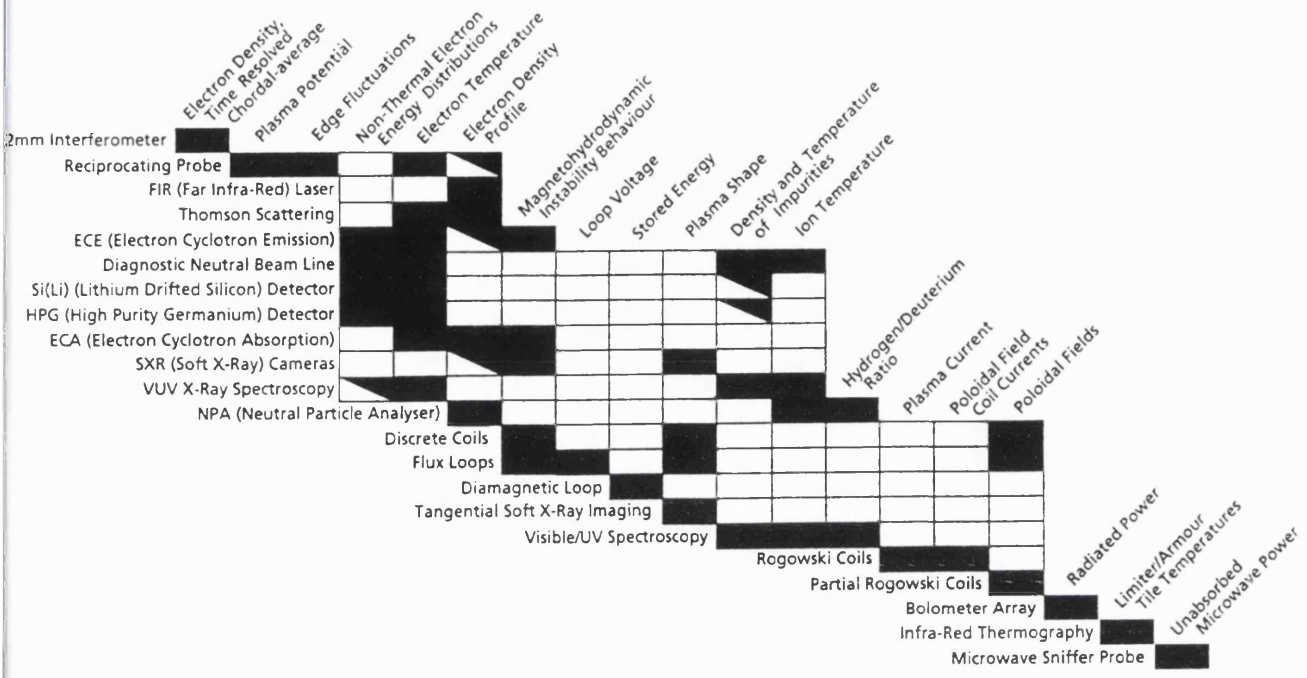

Figure 1.4: *The COMPASS-D diagnostics from [Compass-D Brochure 1994].*

voltage measured at the ends of the coils is

$$V = nA\mu\frac{dI_p}{dt}, \tag{1.27}$$

where n is the number of turns, A is the cross section area of the solenoid, μ is the magnetic permeability. An integrator is used to measure the plasma current I_p from the time varying $\frac{dI_p}{dt}$.

A single coil in the toroidal direction is used to measure the loop voltage which is the voltage that drives the plasma current.

1.4.2 Electron Temperature and Density Diagnostics

The electron temperature can be measured from the intrinsic radiation emitted from the plasma, for example by measuring the slope of the continuum radiation. Laser scattering techniques have now mostly replaced other methods.

Thomson scattering involves the introduction of photons into the plasma, with momentum small compared with the electron momentum such that there is negligible change of momentum during a collision; visible wavelengths are

therefore chosen. The cross section for incoherent scattering is small;

$$\sigma = \frac{8\pi r_e^2}{3}, \tag{1.28}$$

where r_e is the classical electron radius. For incoherent scattering, the shielding around individual electrons is weak and the total scattered intensity is simply the sum of the scattering from the separate electrons. The spectrum of the scattered light is Maxwellian in shape, the electron temperature is given by Doppler shifts and broadening of the scattered spectrum compared with the spectrum of the incident laser beam (the Doppler effects are due to thermal motion of the electrons). The high speed of the electrons causes a blue shift of the spectrum; these relativistic effects become important at $T_e > 1keV$. The electron density is derived from the absolute intensity of the spectrum.

The electron density can also be determined by measurement of the refractive index of the plasma at microwave frequencies by a Mach - Zehnder interferometer. The refractive index for the ordinary wave ($\mathbf{E} \parallel \mathbf{B}$) is given by;

$$N^2 = 1 - \frac{n_e}{n_c}, \tag{1.29}$$

where n_c is the cut off density of the interferometer, which is dependent on the wavelength used. In general only the ordinary wave is used, the extraordinary wave is removed by the use of a polariser. It is also assumed in equation (1.29) that magnetic field effects are negligible. One arm of the interferometer crosses the plasma and the phase change due to the refractive index is compared with the reference which does not pass through the plasma. The number of fringes is given by;

$$F = \frac{\Delta\phi}{2\pi} = 4.49 \times 10^{-16} \lambda \int n_e dl, \tag{1.30}$$

where $\Delta\phi$ is the phase change, λ is the wavelength ($2.17mm$ on COMPASS-D). The measured quantity is $\int n_e dl$ which is the chord average density. For COMPASS-D SNX plasmas the path length is $48cm$.

1.4.3 Impurity Monitoring Diagnostics

Impurity ions are excited in the plasma and emit line radiation. Spectroscopy is used to survey the impurities. The atomic physics behind the spectral lines can

be used to diagnose the plasma further. Broad-band spectrometers have been developed for the visible and the UV regions using gratings and for the soft x-ray region using crystals and multilayers. High resolution work involving detailed line profile analysis is usually carried out in the visible and soft x-ray regions. High resolution soft x-ray spectroscopy is the subject of this thesis.

1.5 Bragg Spectroscopy

Diffraction in the soft x-ray region is achieved with naturally occurring and manufactured crystals where the lattice spacings are of the same order of magnitude as the x-ray wavelengths. A review of crystal theory can be found in [Burek 1976]. There is only weak specular reflection from the individual crystal lattice planes, but reflections from one lattice plane under certain conditions will interfere constructively with reflections from other planes. This occurs when the path difference between the reflections is an integral number of wavelengths: this is known as Bragg's law and is given by;

$$n\lambda = 2dsin\theta_B, \tag{1.31}$$

where λ is the wavelength of interest, d is the lattice spacing (both in the same units, $\mathring{A}$ will be used here), n is the order of diffraction and θ_B is the Bragg angle (the angle between the crystal surface and the incident x-ray beam). Small corrections are required for temperature and refractive index effects. Crystal diffraction requires the thickness of the crystal (not just the surface) as many lattice planes are used.

The choice of crystal to be used for a particular measurement is clearly dependent on the lattice spacing. The crystal reflectivity and diffraction width must also be considered. Two theoretical models are used to calculate these effects; the mosaic, imperfect crystal model and the Darwin - Prins ideally perfect crystal model.

The mosaic model is a kinematical theory. The intensity of the incident beam is uniform throughout the crystal and the interaction between the incident and reflected beams is negligible. The theory assumes that the crystal is thin and is made up of separate crystal domains. If the domains are sufficiently small

then primary and secondary extinction can be ignored. Primary extinction is the reduction of the incident beam intensity due to scattering from the crystal domains as the beam passes through and secondary extinction is the reduction of the reflected beam intensity due to interference from other nearby similary oriented domains. The blocks reflect independently. The total reflectivity of the crystal is calculated from the sum of the separate reflectivities. The diffraction profile depends on the size and distribution of the domains and cannot be determined for a real crystal.

The Darwin - Prins theory is a dynamical theory which takes into account the interaction between the incident and reflected beams as well as including the effects of absorption within the crystal. The theory considers the interaction with the crystal at each lattice plane taking into account secondary reflections from previous lattice planes etc. Two limiting cases can be investigated; zero extinction (which converges to the Mosaic theory) and zero absorption. The diffraction profile can be calculated, and in the zero extinction case is Lorentzian in shape. Real crystals lie between these two limiting cases and for accurate work measurements are required for the diffraction width and the reflection integral. For a detailed discussion of measuring techniques see [Hall 1980].

A sample crystal rocking curve is shown in Figure 1.5. The reflection integral R_c is defined as

$$R_c = \int_0^{\frac{\pi}{2}} P_\theta d\theta, \tag{1.32}$$

where P_θ is the ratio of the reflected beam intensity to the incident beam intensity at an angle θ. For a crystal scanned over the range $\theta = 0 \rightarrow \frac{\pi}{2}$ the total reflectivity is R_c. For a scanning crystal we have

$$\frac{E}{I} = \frac{R_c}{\omega}, \tag{1.33}$$

where E is the total reflected beam intensity and I is the incident beam intensity, ω is the angular velocity of the scanning crystal. For a fixed crystal the peak reflectivity P_0 is given by

$$P_0 = \frac{I(\theta)}{I}. \tag{1.34}$$

where $I(\theta)$ is the reflected intensity at the peak of the rocking curve.

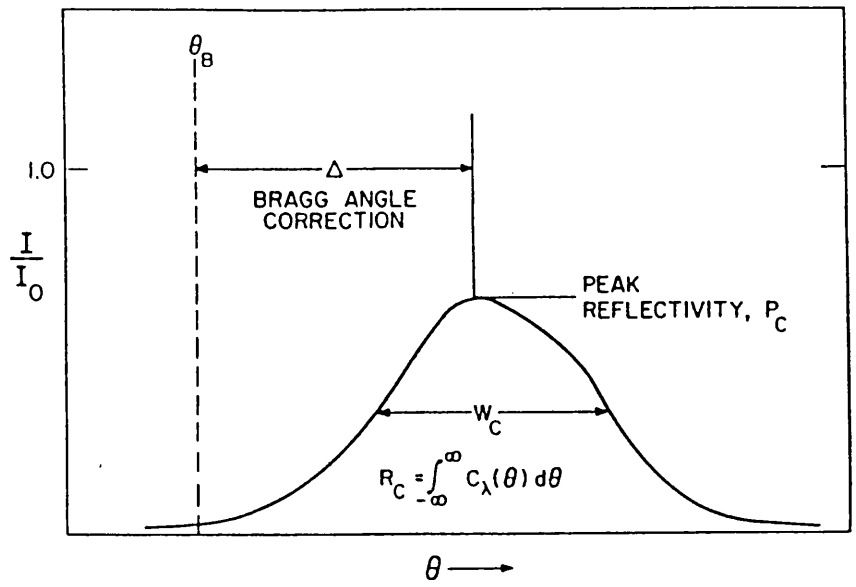

Figure 1.5: *Example of a crystal rocking curve showing the definition of the peak reflectivity and integrated reflectivity. The crystal is scanned over* $\theta = 0 \rightarrow \frac{\pi}{2}$, *the integrated reflectivity is the total reflectivity over this range. From [Burek 1976].*

The Darwin - Prins theory can be extended to include changes to the reflection integral caused by bending the crystal. The crystal is modelled with a lamellar model [White 1950]. The crystal is approximated by a set of perfect crystal lamellae each with reduced thickness A, which is a function of depth within the crystal, the Bragg angle, the angle between the lattice planes and the crystal surface, and other crystal properties [Caciuffo et al 1990]. This results in a misorientation y of the angle between the incident beam and the lattice planes;

$$y = y(0) + cA; \tag{1.35}$$

$y(0)$ is the value of y when $A = 0$, c is a constant which is dependent on various crystal properties and on the crystal radius of curvature. Neighbouring lamellae differ by $\Delta A = \frac{2}{c}$ and $\Delta y = 2$. The total crystal reflectivity is the sum of the partial reflectivities at each lamillae.

An example of the changes in the crystal reflectivity due to curvature of the crystal for Si(111) is shown in Figure 1.6 from [Caciuffo et al 1990]. A simple stress analysis can also be used to calculate the change of the crystal lattice spacing due to crystal bending [Barnsley 1993].

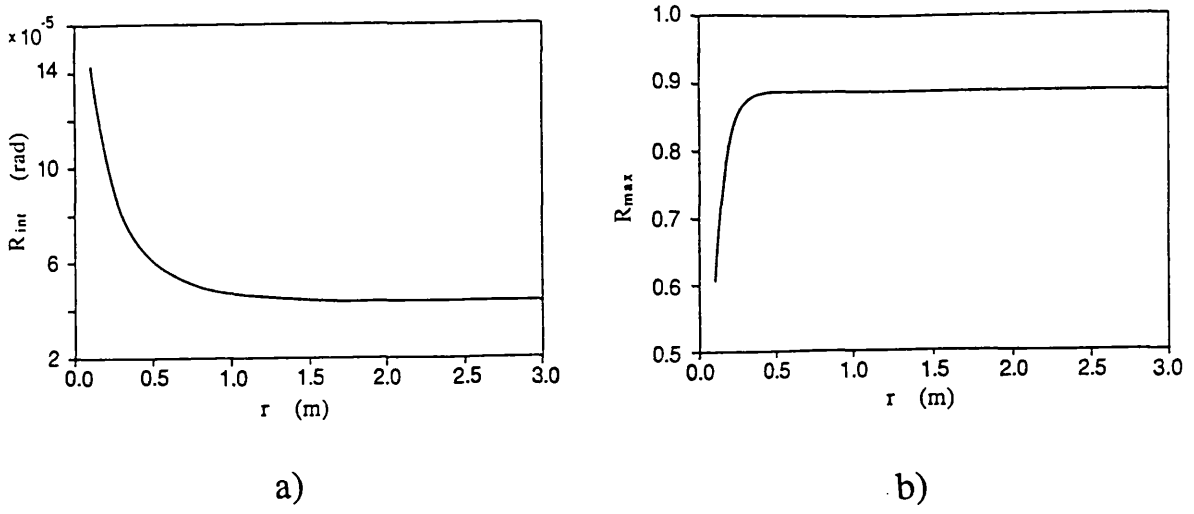

Figure 1.6: *Change in a) the integrated reflectivity and b) the peak reflectivity due to the bending of a Si(111) crystal, calculated for* $\lambda = 1.871\mathring{A}$. *From [Caciuffo et al 1990].*

Survey spectrometers generally use a single crystal scanning over a wavelength range. A Bragg rotor spectrometer has been designed [Barnsley 1993] which has six different crystals mounted onto a hexagonal rotor to survey the complete soft x-ray range ($1 - 100\mathring{A}$) in a single revolution of the rotor. High resolution spectrometers use either a scanning double crystal or a fixed focussing crystal with either the Johann [Johann 1931] or Von Hamos [Von Hamos 1933] geometry. This thesis describes results obtained from a high resolution Johann spectrometer.

Chapter 2

Instrumentation and Data Analysis

The curved crystal spectrometer was first used by Johann in 1931 [Johann 1931]. The spectrometer is a focusing spectrometer which uses a bent crystal and the Rowland circle principle.

The spectrometer used here is of a very versatile design allowing the Rowland Circle diameter and the crystal and Bragg angle to be changed easily. The detector used is a large area CCD array ($29mm \times 26mm$).

In this chapter the principle of the Johann spectrometer is described and a detailed description is given of the COMPASS-D curved crystal spectrometer including the instrument width and sensitivity.

The spectrometer is a high resolution device from which measurements can be made of line profiles and shifts. Spectral lines are fitted with Voigt profiles taking account of a Lorentzian instrument function and Gaussian line broadening. Ion temperatures are derived from the Gaussian width and plasma velocity shifts are found from changes in the line centroid position. For low density plasmas where the photon statistics are too weak for satisfactory line fitting, cross-correlation with a standard spectrum is used to find changes in the line centroid position.

2.1 The Spectrometer

2.1.1 Geometry

X-rays are diffracted onto the detector using the Johann geometry. The crystal is bent to a radius of curvature equal to the Rowland circle diameter and is placed on the circle circumference. X-rays from a source also on the circumference will be focused according to Bragg's law onto the Rowland circle circumference. A position sensitive detector placed appropriately on the circumference is then used to record the spectrum. Such an arrangement is shown in Figure 2.1. Using this

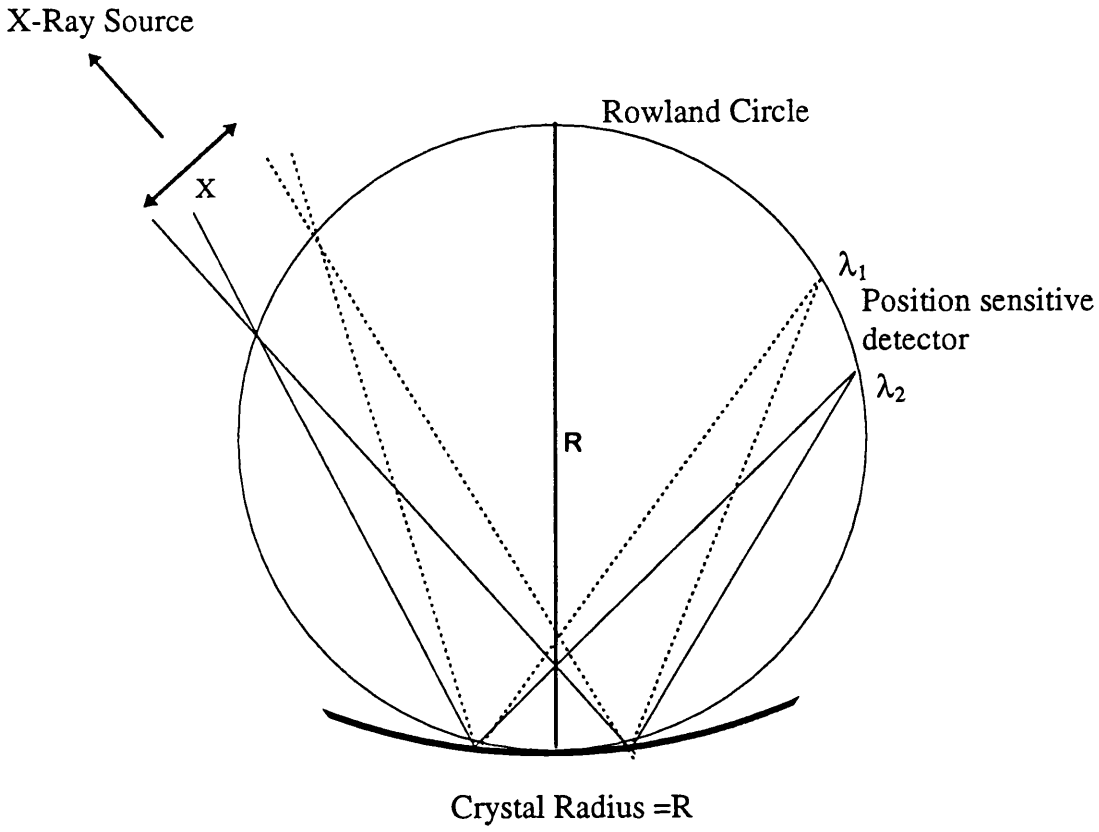

Figure 2.1: *Rowland circle geometry. The crystal is bent to a radius R, x-rays from a source on or beyond the Rowland circle are focused by the crystal as shown.*

arrangement the whole crystal area is used to diffract each wavelength fraction. The spectrometer is optimised when each crystal element diffracts equally each wavelength.

The physical size of the source, X in Figure 2.1, subtends an angle $\Delta\theta$ onto

the crystal and this defines the size of the wavelength region diffracted by the crystal,

$$\Delta\lambda = 2dcos\theta\Delta\theta, \tag{2.1}$$

where $\Delta\lambda = \lambda_2 - \lambda_1$ in Figure 2.1.

The instrument f number is given by

$$f = \frac{W}{R}, \tag{2.2}$$

where W is the effective crystal width and R is the Rowland circle diameter.

The instrument resolving power is given by

$$\frac{\lambda}{\delta\lambda} = \frac{tan\theta_B}{\delta\theta}, \tag{2.3}$$

where $\delta\theta$ is the instrument width which will be discussed in section 2.2.

In practice a number of changes have been made to our system from the ideal Johann geometry. The detector does not sit entirely on the Rowland circle, but is at a tangent to it, the centre of the detector lying on the circle. The other significant change is that the x-ray source lies beyond the Rowland circle. The tangential detector will give a slight non linearity to the wavelength scale on the detector. The Rowland circle acts as a virtual slit for an x-ray source beyond the circle; the focusing properties are not affected.

2.1.2 The Crystal and Focusing Procedure

The crystal used for the Cl XVI measurements was Si(111) with a $2d$ lattice spacing of $6.271\mathring{A}$ and for the centre of the spectral region of interest ($4.47\mathring{A}$) the Bragg angle used was 45.47°. The Rowland circle radius used for most of the measurements was 1240 mm. The crystal was bent to this radius using a four bar bending jig [Dunn 1990]. The crystal resolving power for the $Cl\ K_\alpha$ line at $4.73\mathring{A}$ is given by [Henke et al 1993] as $\frac{E}{\delta E} = 7910$ for the σ polarisation. The Cl XVI wavelengths are very close to the Brewster angle for Si(111) and therefore only this polarisation is significant. The effects of the crystal bending have been discussed in chapter 1.

The crystal is bent to the required radius of curvature by focusing in visible light. The focusing procedure is as follows:

1. The apparatus used are a microscope lamp with a tungsten filament, an orange filter, a variable slit, the crystal held in the bending jig, a mirror, a focusing screen and an eyepiece which are set up as in Figure 2.2. The optics are placed on an optical bench and the lengths are measured with a ruler. The optical distance between the slit and the crystal and the crystal and the focusing screen are equal to the required Rowland Circle diameter i.e. almost normal incidence at the crystal centre. The mirror is used so that the focusing screen and the bending jig can be placed close to each other for convenience, the angle between the incident beam and reflected beam being taken into account in the length measurement.

2. Initially a wide slit is used to check the alignment, the image seen on the focusing screen is an image of the slit. It is useful at this stage to aperture the crystal to reduce focusing errors from the crystal ends. The crystal used is $25mm \times 80mm$ and is apertured down to the central $25mm \times 20mm$. The crystal used has a thickness of $0.5mm$, thinner crystals ($0.3mm$) are used for tighter radii of curvature.

3. The four bar bending jig has four micrometer screws to control the crystal bending and focusing. The four screws which control different parts of the crystal are turned evenly until the image on the focusing screen is in focus. The slit is then narrowed and the same procedure is repeated. When the image becomes too narrow to be seen on the focusing screen with the naked eye, an eyepiece is used to view the focusing screen. This procedure of narrowing the slit and adjusting the screws is continued until a good focus is achieved; i.e. when the image is at its narrowest and is even.

4. When satisfied with the focus, the crystal jig is tapped firmly with a small metallic object and the focus is then rechecked. This is done to ensure that the jig is in a relaxed position and that the bending bars will not alter position later on and change the focus.

5. The crystal is set to the correct Bragg angle using a vernier rotary table which then fits into the spectrometer.

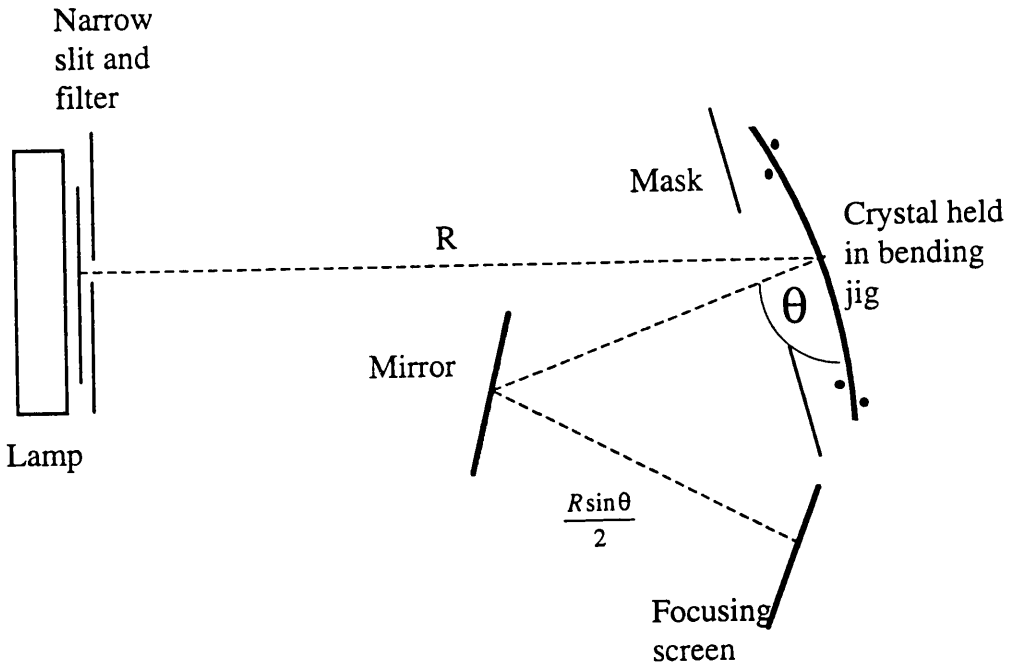

Figure 2.2: *The crystal focusing setup. The crystal is focused using visible light, the adjusting screws on the bending jig are adjusted until the sharpest focus is seen on the focusing screen.*

Further details of the crystal focusing and alignment procedure and of the crystal bending jig design can be found in [Dunn 1990].

2.1.3 CCD Detector

The detector used is a large area CCD array containing 1280×1170 pixels. The pixel size is $22.5\mu m \times 22.5\mu m$ and the total area is $29mm \times 26mm$. The detector is placed at a tangent to the Rowland circle at the required Bragg angle from the crystal. A CCD detector is used because it is position sensitive, has good quantum efficiency and can record individual spectra with good time resolution ($\approx ms$).

A CCD consists of an array of MOS (metal oxide silicon) capacitors on a Si

wafer: each capacitor acts as a single pixel. Each capacitor is surrounded in one direction by a p- type channel and in the perpendicular direction by polysilicon electrodes. The p- type channels separate adjacent pixels into separate pixel columns and the polysilicon electrodes are biased to form a potential well in each pixel to separate pixel rows. The pixels are then allowed to accumulate charge by photoionisation from photon interaction with the Si which produces hole - electron pairs. The charge is then extracted from individual pixels by switching the bias potentials on the polysilicon electrodes to move the charge along pixel columns. Figure 2.3 shows the CCD array structure and the clocking pulses on the electrodes for transferring the charge. The final row of pixels is an

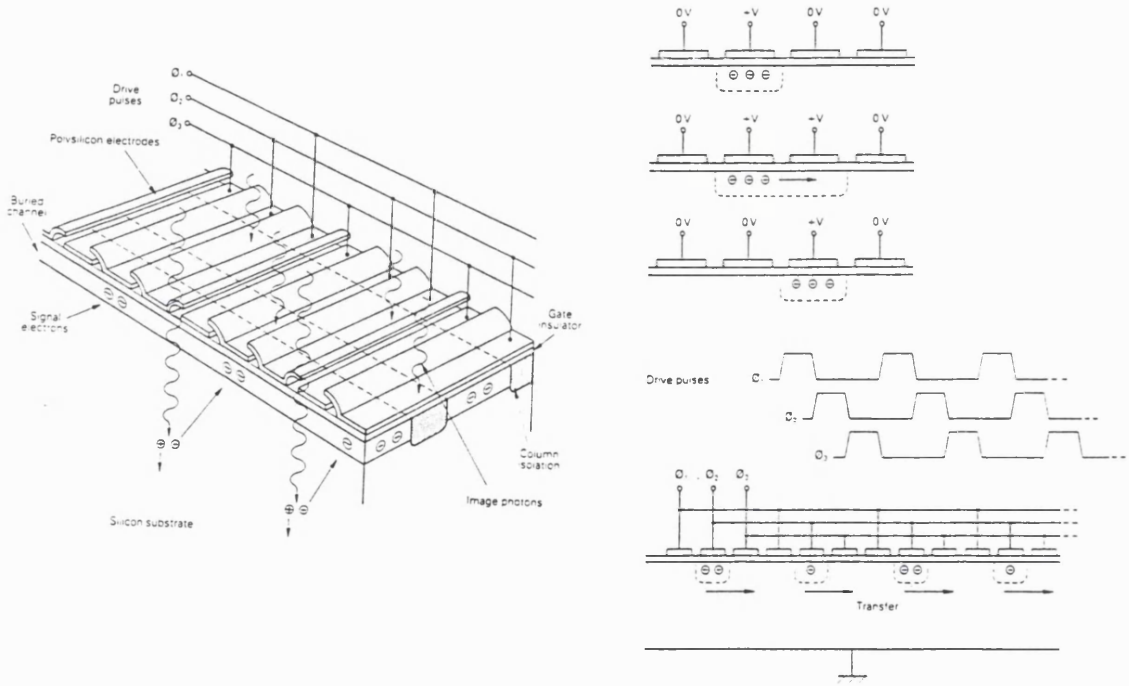

Figure 2.3: *CCD array structure and three phase clocking. From EEV.*

analogue shift register and the charge is read out from this row via a low noise amplifier.

Two different modes of CCD operation are used on our spectrometer. The CCD array is illuminated by x-rays diffracted from the crystal, each spectral line filling a number of pixel columns. The CCD can be sequenced to integrate the charge over a given time span, for example the duration of a plasma pulse.

The whole CCD is then read out to produce a 2D image of the spectrum as would be seen by photographic film. This mode of operation is used to check the detector alignment, i.e. to check that the spectral lines are aligned along the pixel columns.

The second mode of operation allows time resolved measurements to be made. Half of the CCD array (the frame store half) is covered over with an aluminium mask and is used for data storage. The other half is used to collect the photons. The total charge collected in a pixel column is then transferred and stored on a single row on the frame store half. This is then repeated until the frame store is full. The frame store half is then read out afterwards. Time resolutions of $< 1ms$ are possible. This is the usual mode of operation. The image obtained is an image of wavelength against time: a contour plot of such an image is shown in Figure 2.4.

The energy ω required to create a hole - electron pair in Si is $\omega = 3.65eV$. The number of hole - electron pairs generated by an incident photon with energy E is $\frac{E}{\omega}$. The CCD can therefore be used to detect single photons with energy resolution determined by the Fano statistics and the electronic noise;

$$\Delta E = 2.36\omega \left(\left(\frac{FE}{\omega} \right) + n^2 \right)^{\frac{1}{2}}, \tag{2.4}$$

where F is the statistical Fano factor ($F = 1.2$ for Si) and n is the RMS number of spurious electrons per pixel. Cooling the detector with liquid nitrogen to $\approx -100°C$ reduces n to ≈ 5 electrons. Thus for Cl XVI photons at 2793 eV, $\Delta E = 93eV$. This is the theoretical limit, in practice $\Delta E \approx 150eV$. This allows the CCD array to be used as an energy dispersive spectrometer on its own. The development of such devices was primarily for astrophysical x-ray sources [Wells and Pounds 1993] where such a non dispersive spectrometer is ideal. The chip is used in the first mode of operation described above with long integration times, and pulse height analysis (PHA) of the pixels is used for data analysis.

In a similar way we can use PHA for an absolute intensity calibration of the spectrometer. A pulse height spectrum is shown in Figure 2.5. The first peak at 160 on the charge / energy scale is the background noise level. The next peak is the Cl XVI level, peaks after that show multi photon events.

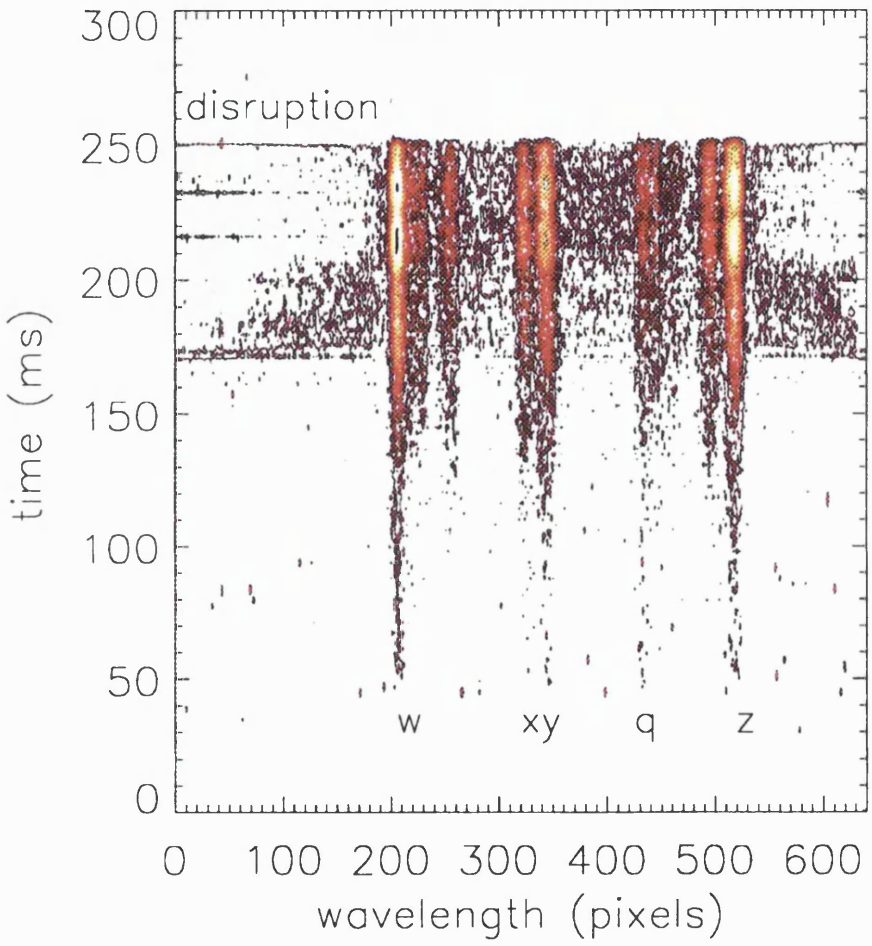

Figure 2.4: *Contour plot of CCD image, a Cl XVI spectrum from COMPASS-D shot #13449 is shown, the line notation is from [Gabriel 1972].(See Table 3.1).*

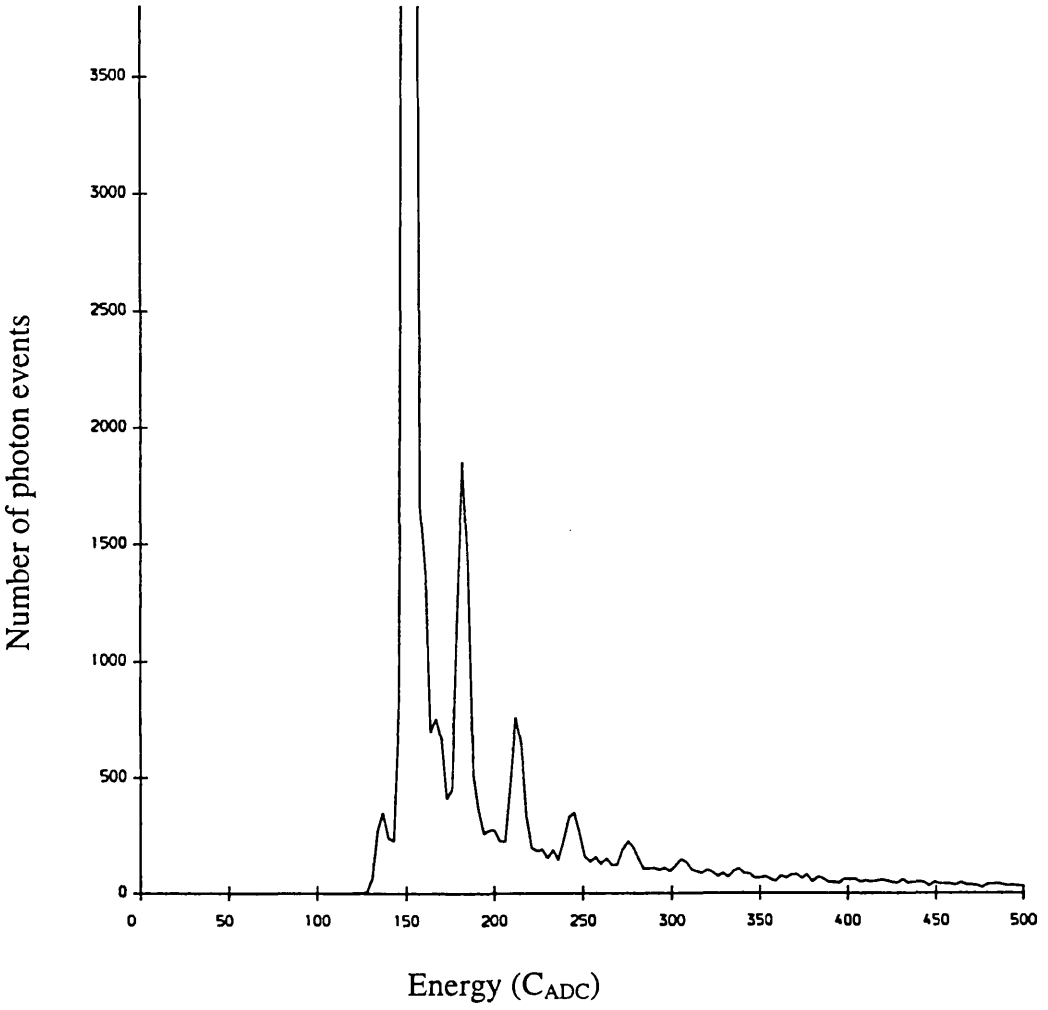

Figure 2.5: *Pulse height spectrum from COMPASS-D shot #14977 (time resolved mode). The first peak at 160 is the background noise level, the peak at 190 is the Cl level (2793 eV), subsequent peaks indicate multi photon events.*

Conventional optical CCDs have poor x-ray quantum efficiency as the absorption depth of the photons is large compared with the depletion depth in which charge is collected. X-ray CCDs are generally manufactured from high resistivity Si which allows a greater depletion depth and greater quantum efficiency. For 3 Kev photons, quantum efficiency is typically $\approx$ 90%.

The CCD used is an EEV CCD05-30-5-202 which is actually manufactured from low resistivity silicon and has a quantum efficiency of $\approx$ 60% at 3 KeV. The advantages of such a device include greater charge transfer efficiency and lower amplifier noise.

2.1.4 Vacuum System

The spectrometer is vacuum coupled to the tokamak vacuum vessel which is kept at a pressure of $\approx 10^{-8} mbar$ during operational periods. The spectrometer flight line pressure must be equal to this or better. A differential vacuum system is used in which the flight line which connects to the torus is kept at $\approx 10^{-8} mbar$. This is separated from the spectrometer section of the vacuum system by a thin ($2\mu m$) polypropylene window. The spectrometer section is kept at $\approx 10^{-6} mbar$. The high vacuum side uses knife edge seals with copper gaskets, the spectrometer side uses O ring seals. A differential system is used so that the spectrometer side can be let up to air and opened up for changes to be made, e.g. to change the crystal. The system can then be pumped down quickly. This is especially useful for the initial alignment of the spectrometer. In order to do this, a valve is closed to keep the high vacuum side at torus pressure and a bypass valve is opened around the window. Both sides of the vacuum system are pumped separately; each side has its own rotary backing pump and turbo pump. The pressure on the torus side is measured with an ion gauge which also serves as an interlock signal to prevent the torus valve from opening if the pressure is not sufficiently low. The spectrometer side pressure is measured with a Penning gauge. The difference in the pressures measured by the ion gauge and the Penning gauge shows if the window is holding.

At one stage an aluminised Mylar window was used, but with the addition of ECRH heating to the plasmas, the aluminium in the window appeared to absorb the heat and burst the window. This was quickly remedied by replacing the window with uncoated polypropylene. The transmission at $4.4\mathring{A}$ of $2\mu m$ thicknesses of Mylar, aluminium and polypropylene are greater than 90% [Dunn 1990].

A schematic of the vacuum system is shown in Figure 2.6. The vacuum system is electrically isolated from the torus by means of a ceramic break.

2.1.5 The Diffraction Arm

The length of the Rowland circle diameter is varied by changing the crystal radius of curvature and by adding different lengths of tube between the crystal and detector. The crystal to detector length ($Rsin\theta$) can be varied in four stages

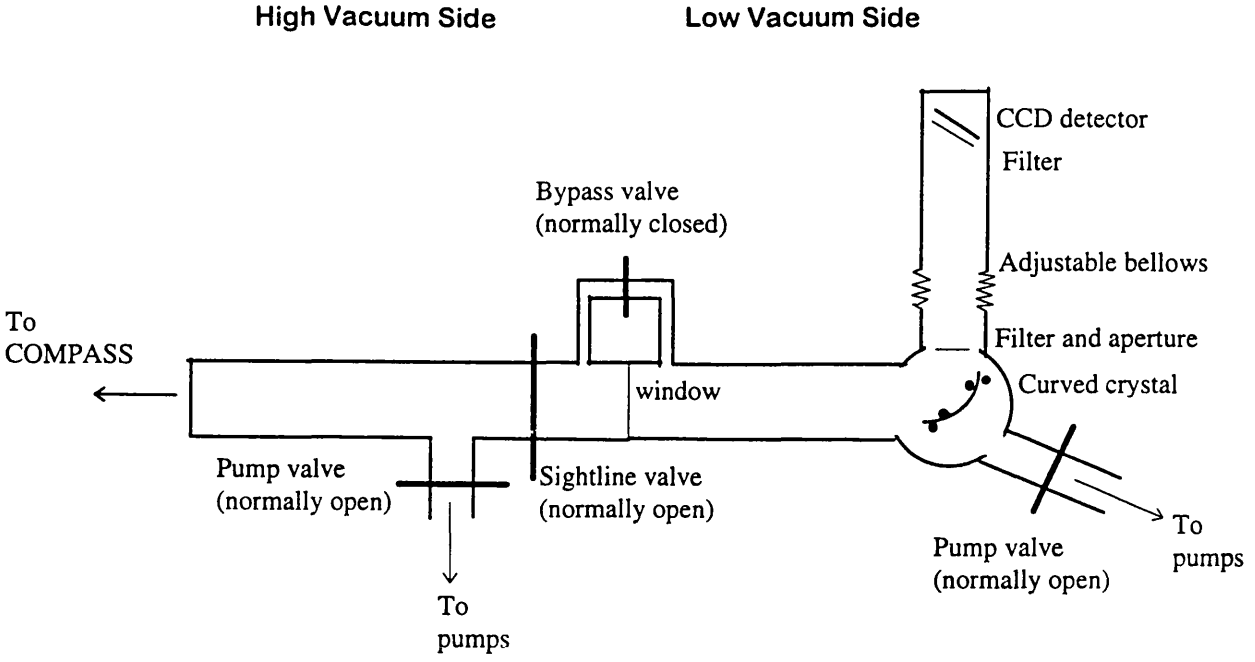

Figure 2.6: *Schematic of vacuum system showing the differential system used.*

from $0.5m$ to $3.5m$. The detector is mounted on a translation stage, providing some extra freedom in the Rowland circle diameter. The rigid tube is mounted at the crystal end with a flexible bellows to relieve stresses and to give freedom of choice of Bragg angle. The crystal chamber has two ports; one at 30° and the other at 50° from the sight line which together with the bellows allow a Bragg angle range of $25° \leq \theta_B \leq 65°$. The crystal and detector positions are thus fixed with respect to each other forming a rigid diffraction arm which is aligned with the plasma as a single unit.

Two visible light filters are used, both of $2\mu m$ aluminised Mylar. One is placed over the CCD and the other on the CCD side of the crystal. The latter has an aperture around it to reduce Johann aberrations (see section 2.2.1).

The detector is cooled with liquid nitrogen. A Dewer is filled with liquid nitrogen, which is thermally coupled by means of a copper "cold finger" and copper braids to the CCD. The detector temperature is monitored with a thermocouple.

A diagram of the diffraction arm is shown in Figure 2.7.

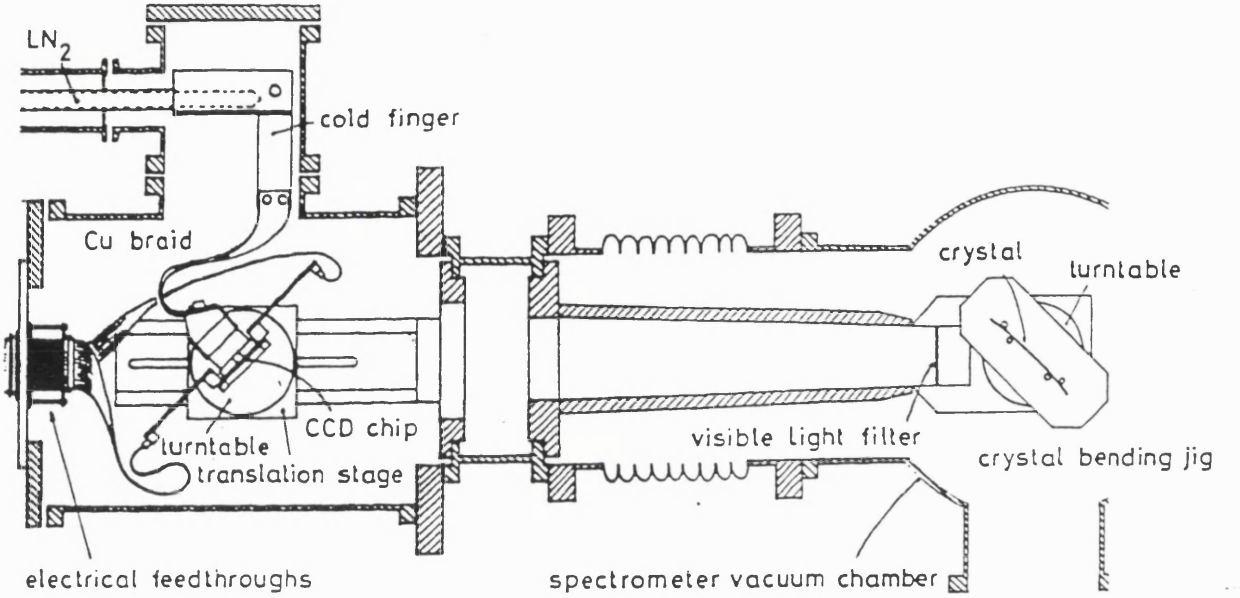

Figure 2.7: *Schematic of diffraction arm showing the crystal, detector and cold finger, from [Barnsley 1993].*

2.1.6 Data Acquisition

An Archimedes computer is used for CCD control and data acquisition. The CCD is powered from a CAMAC unit (Computer Automated Measurement and Control, IEEE Standard 583-1975). The CCD sequencer program which controls the CCD clocking and the mode of operation is downloaded from the computer to the CAMAC unit through an RS423 (serial data communications standard) optical link. Information regarding the status of the CCD is passed back through the link to the computer. An optical trigger signal is received by the CAMAC unit 2.6s before the start of a plasma pulse.

Data is read out of the CCD through a low noise amplifier to an ADC where the signal is digitised into 12 bits. The signal is then transferred in parallel to the Archimedes. There is a requirement of electrical isolation between COMPASS diagnostics and the outside, hence the signal must be transferred optically. To reduce the number of fibres required, the signal is changed to serial and then converted to an optical pulse which is then transmitted through a monomode fibre (the signal is transmitted at 40 MBaud); it is then changed back to electrical

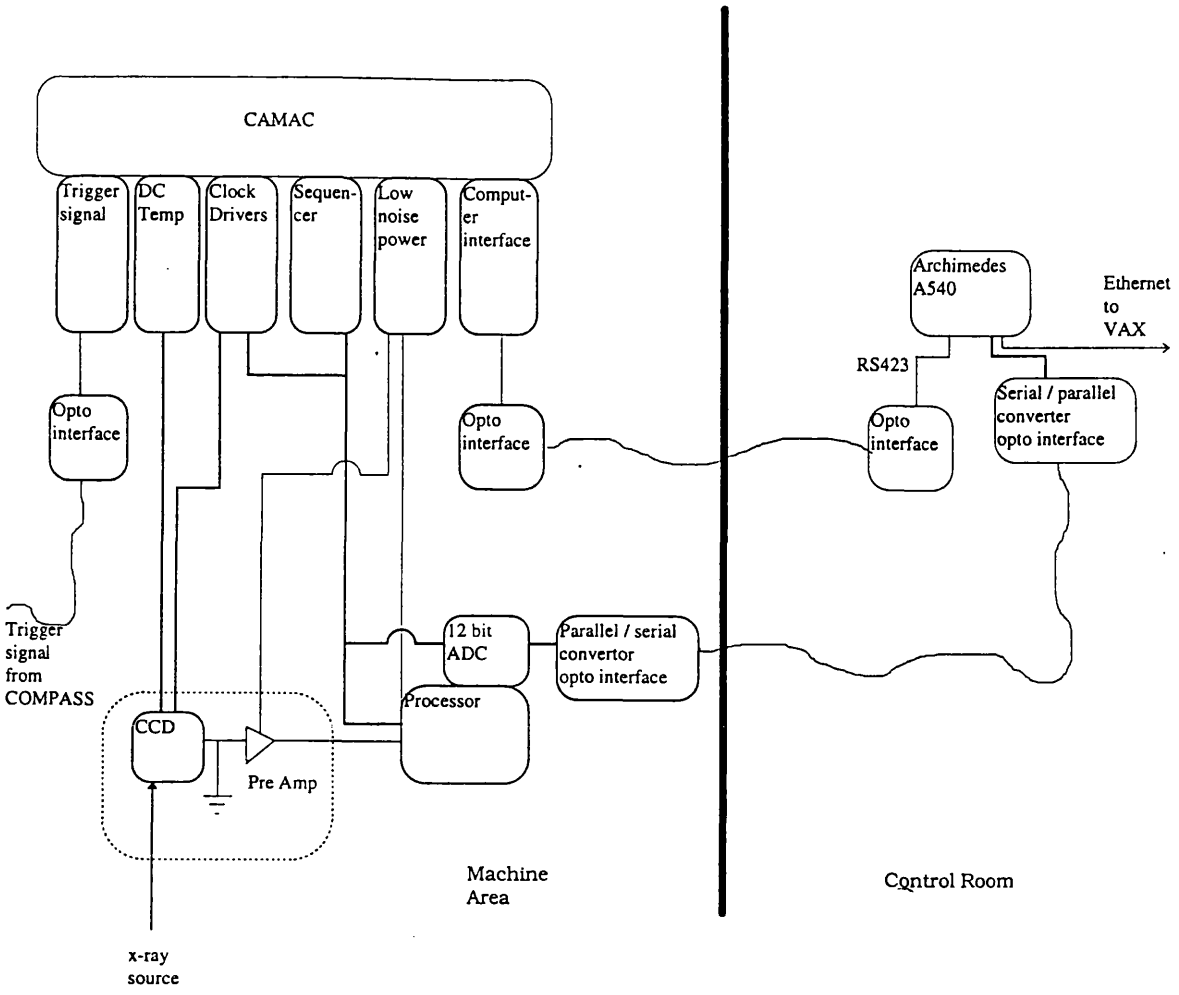

Figure 2.8: *Data acquisition system*

and parallel before going into the Archimedes 16 bit parallel interface. The data is then stored on the Archimedes hard disk as a binary image file.

Due to limitations on disk space and the requirement to store all COMPASS data centrally, the image files are transferred through ETHERNET to the COMPASS VAX where the file format is changed to the COMPASS IDA format, the files are then archived. Data analysis programs on the VAX are then used to analyse the data. Figure 2.8 shows the data acquisition system.

The CCD electronics and the CAMAC control modules were built and supplied by Leicester University, the serial / parallel optical interface was designed and built by the electronics group at Culham Laboratory.

2.2 Instrumental Effects

There are two types of instrumental effects to take into account; the effect of the instrument on the spectral line width and the effect on the spectral line intensity. The line width is broadened by a number of factors; the more significant ones include the quality of the crystal focus, the Johann focusing aberrations, the crystal diffraction width and the detector spatial resolution. The line intensity across the detector is dependent on how evenly the detector is illuminated, which is determined by the geometry of the system.

The crystal diffraction width is assumed to be Lorentzian in shape (see sections 1.5 and 2.2.3). The natural line width is also Lorentzian, but is negligible in comparison with the other broadening mechanisms.

2.2.1 The Johann Aberrations

Two effects of the Johann geometry relating to the line shape will be discussed; one resulting from the crystal width (parallel to the plane of dispersion) and the other from the crystal height (perpendicular to the plane of dispersion).

The focusing aberration due to the crystal width is caused by the crystal radius of curvature being equal to the Rowland circle diameter and therefore only the crystal centre is actually on the circle. The focusing defect increases with the distance of the point of reflection from the centre of the crystal (i.e. the crystal width) and is much more pronounced on the short wavelength side. The aberration results in a displacement to the short wavelength side. The intensity variation due to the distortion against wavelength is shown in Figure 2.9 from [Johann 1931, Sändstrom 1957]. Johann has characterised this displacement in terms of a line width;

$$\Delta\theta = \frac{W^2}{8R^2 tan\theta_B}, \tag{2.5}$$

where W is the crystal width. The aberration can be reduced by careful choice of Rowland circle diameter and crystal width. In practice we have reduced it by aperturing the crystal width. Using a crystal apertured down to $20mm$ in our experimental setup gives $\frac{\lambda}{\Delta\lambda} = 3 \times 10^4$ which is equivalent to a broadening of 0.63 pixels on the CCD array.

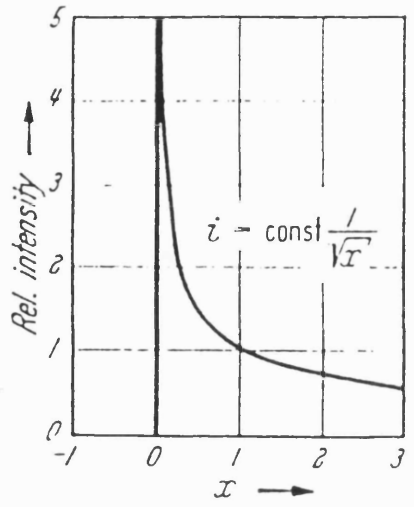

Figure 2.9: *Wavelength distortion due to Johann width error, from [Sändstrom 1957].*

The Johann height defect results from the reflection of a ray from a point A_1 on the Rowland circle (entrance slit) to the arc of a circle $C_1E_1H_1$ on the detector, see Figure 2.10 from [Sändstrom 1957]. The arc of the circle is actually

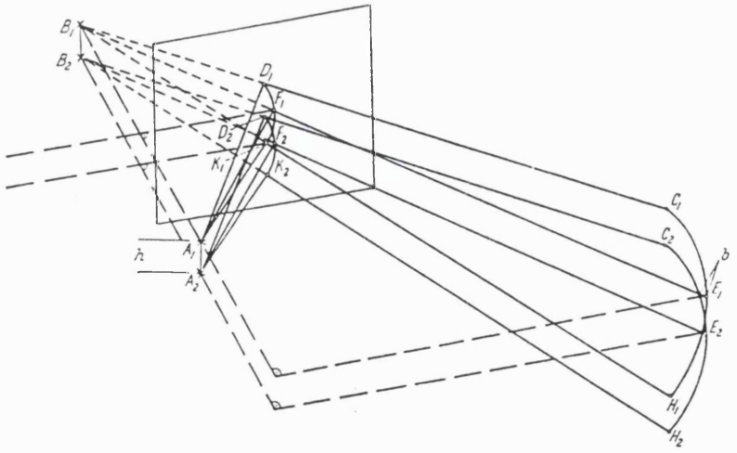

Figure 2.10: *Johann height aberration, from [Sändstrom 1957].*

the surface of a cone, the apex being the virtual image of A_1, shown as B_1 in the figure. The full Johann height aberration is given by the summation of all these arcs integrated over the crystal height. Assuming that the source, crystal and detector are of equal height, H, the broadening due to this aberration is [Johann 1931];

$$\Delta\theta = \frac{H^2}{8R^2 sin\theta_B cos\theta_B}. \tag{2.6}$$

Again this can be minimised by careful choice of the crystal height and the Rowland circle diameter. For our setup with a crystal with $H = 25mm$, the broadening is $\frac{\lambda}{\Delta\lambda} = 1 \times 10^4$ which is equivalent to 2.0 pixels.

Other less significant aberrations resulting from the Johann geometry due to the detector include a broadening due to the detector being placed at a tangent to the Rowland circle and a defocusing broadening if the detector is slightly off position. The most significant broadening however results from the quality of the focus.

2.2.2 Detector Broadening

The detector spatial resolution is the limiting resolution of the spectrometer whichever crystal is used. For a CCD array this is the pixel size. In terms of line broadening this is given by

$$\Delta\theta = \frac{\Delta X}{Rsin\theta_B}, \tag{2.7}$$

where ΔX is the pixel size. For this work we have used double pixels on the wavelength axis i.e. the actual pixel size used is $45\mu m \times 22.5\mu m$. This reduces charge spreading across pixels and also reduces the amount of data to be stored. The broadening due to the spatial resolution is $\frac{\lambda}{\Delta\lambda} = 2 \times 10^4$.

Charge spreading in the CCD array can be investigated by taking a 2D image without a significant number of multi photon events and then systematically looking through the pixels for photon events and then looking at the surrounding pixels for any increase in charge. This can then be averaged over a number of pixels to give the charge spreading. Figure 2.11 shows the charge spreading function measured using an ^{55}Fe source. As can be seen from the figure, this contribution to the broadening can be considered to be negligible.

2.2.3 Measurement of Instrument Width

A direct measurement of the instrument width has not been possible because there was no available x-ray source which could be used in situ on the torus. However, a measurement of the line shape of a "cold" source was made. The spectrometer was set up with a silver L_α source, ($4.16\mathring{A}$) with a Si(111) crystal at

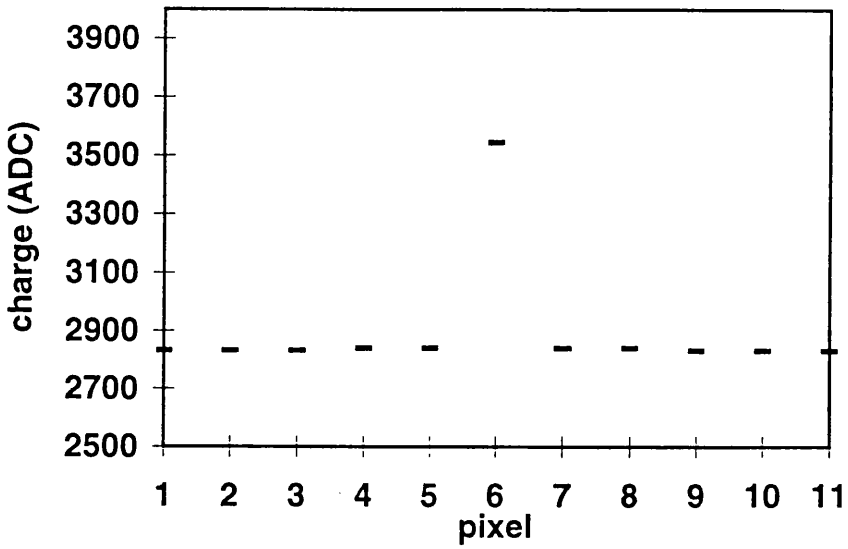

Figure 2.11: *Charge spreading in the CCD array measured with an* ^{55}Fe *source. An area of* 11×11 *pixels was looked at around each pixel containing charge. This was then averaged over the whole CCD area.*

a Bragg angle of 41.6° and a Rowland circle diameter of $1725mm$. The resulting spectrum was fitted with a Lorentzian profile and is shown in Figure 2.12.

A number of problems were highlighted by this exercise. No direct measurement could be made of the instrument function as this would require an x-ray source of the correct wavelength being available and the ability to slide it in place whilst still attached to the tokamak. This however has been done for Lamb shift measurements where an argon source could be fitted into the spectrometer sightline between plasma pulses in order to obtain an absolute wavelength calibration [Källne et al 1984].

The limits of the spectrometer resolution cannot be measured directly with a K_α or L_α source. Figure 2.13 shows $\frac{E}{\Delta E}$ against Z for $K_{\alpha 1}$ and $L_{\alpha 1}$ lines, the $K_{\alpha 1}$ widths are from [Krause and Oliver 1979] and the $L_{\alpha 1}$ widths are from [Salem and Lee 1976]. The $K_{\alpha 1}$ widths are semi empirical and the $L_{\alpha 1}$ widths are from least square fits to experimental data, all the widths are natural line widths. The wavelengths are taken from [Kirz et al 1986]. The maximum resolution for a $K_{\alpha 1}$ line is $\frac{\lambda}{\Delta\lambda} \approx 4000$. A high resolution spectrometer should exceed this. The line width in such an experiment can be reduced by monochromating the

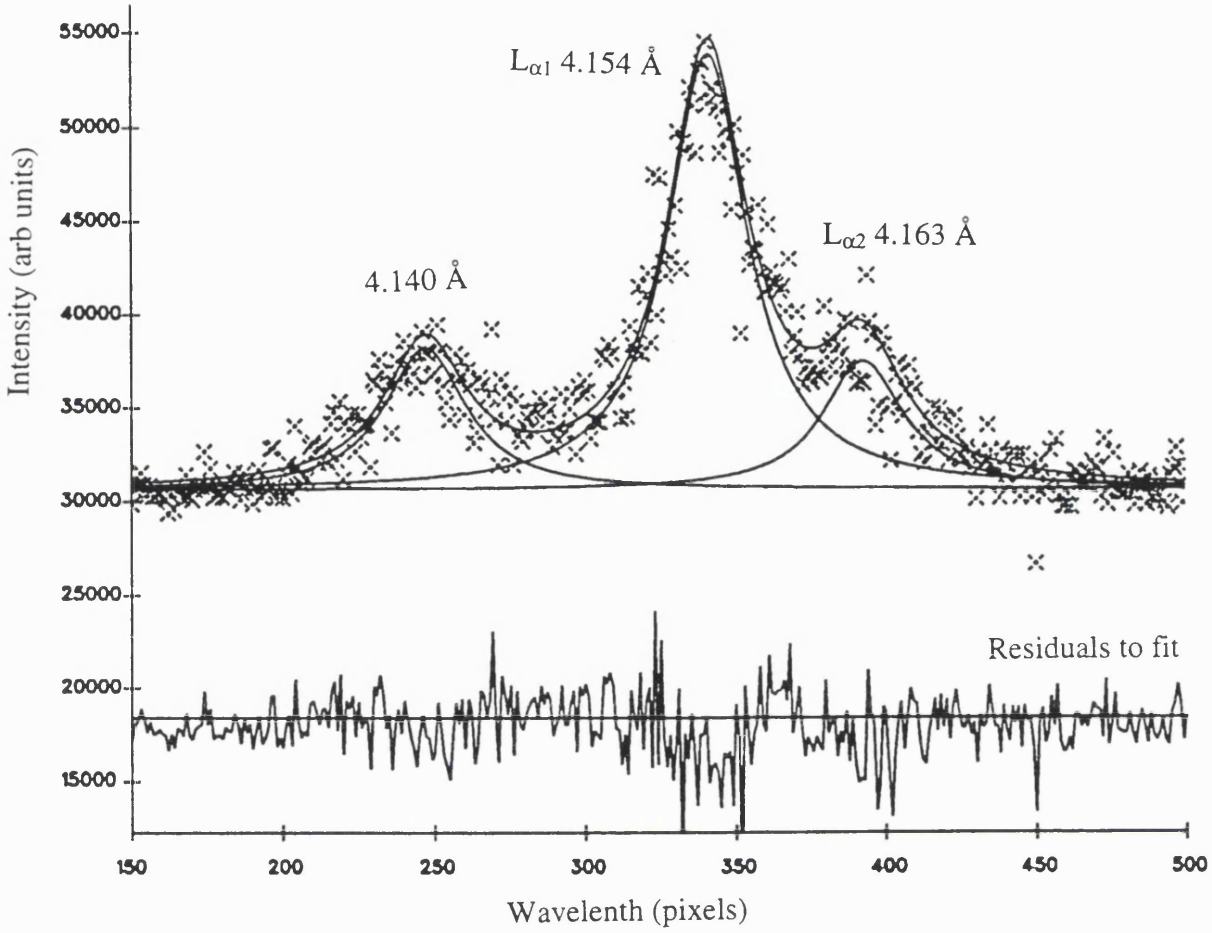

Figure 2.12: *The silver* L_{α_1} 4.15443*Å and* L_{α_2} 4.16294*Å lines were obtained from a "cold" source and subsequently fitted with a Lorentzian line profile. The line at* 4.140*Å remains unidentified. The measured* $\frac{\lambda}{\Delta\lambda} \approx 800$ *compared with the theoretical value of* 1280.

source with a crystal, but this adds in an extra uncertainty from the diffraction width of the monochromator.

The actual instrument function used has been assumed to be Lorentzian in shape and equal in width to the narrowest lines measured on COMPASS-D i.e. from low density plasmas with low ion temperatures. This is equivalent to $\frac{\lambda}{\Delta\lambda} \approx 2100$ which is equivalent to 9.5 pixels.

The various contributions to the line width are shown in Table 2.1.

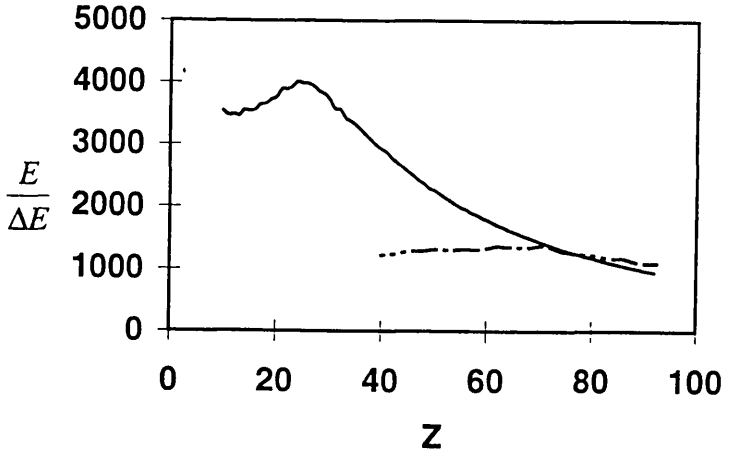

Figure 2.13: *The theoretical resolutions of K_α (solid line) and L_α (dashed line) x-ray line widths.*

Table 2.1: *Contributions to the instrument width*

Effect	Resolution $\frac{\lambda}{\Delta\lambda}$	Width in pixels
Crystal diffraction width	< 7910	> 2.5
Johann width error	3×10^4	0.6
Johann height error	1×10^4	2.0
Detector spatial resolution	2×10^4	1.0
Focusing error	unknown	unknown
Detector charge spreading	negligible	0.0
Total (assumed from narrowest lines)	≈ 2100	≈ 9.5

2.2.4 Line Intensity Effects

There are some instrumental effects which affect the line intensity rather than the width. These are mainly geometrical in origin. The torus port diameter is $40mm$ in diameter with a small ($8mm$) constriction on one side. The port to crystal distance is $2510mm$. This small ratio of port size to flight line length imposes serious vignetting problems which causes the detector to be illuminated unevenly. The vignetting function can be calculated from the geometry and can also be seen on the background radiation. Figure 2.14 shows a spectrum in which the vignetting is clearly seen. The vignetting function used for data analysis has been obtained by averaging over a number of discharges.

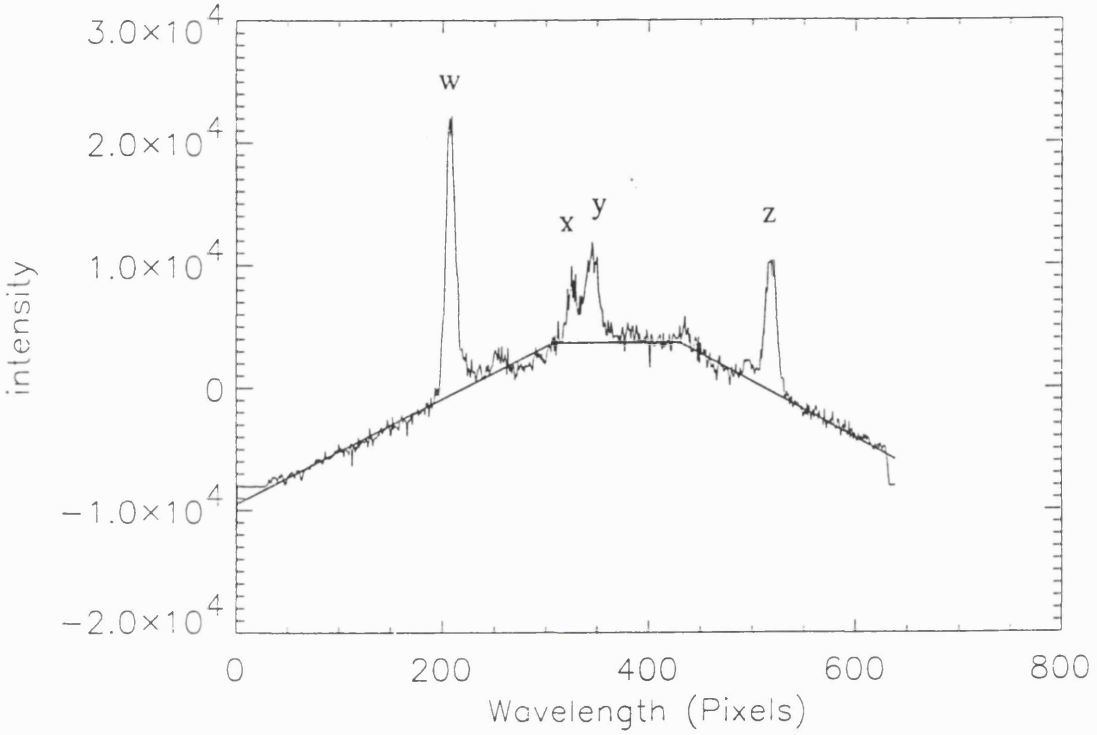

Figure 2.14: *Trapezoidal window function obtained from high background during neon puffing in shot #14368. Cl XVI spectrum (see Table 3.1). The continuum level is discussed in section 5.1.*

High density plasmas with a high x-ray flux can saturate the ADC. This can be prevented by the addition of a voltage divider at the input of the ADC. Saturation of the ADC has occured very infrequently and so an additional voltage divider is generally not used. Alternatively at very high photon fluxes the pixels of the CCD can be saturated. This occurs at 3×10^5 electrons per pixel which is equivalent to a current of $300nA$. The sensitivity of the CCD is assumed to be even across the required wavelength range which is small.

2.3 Spectrometer Calibration

There are in principle two separate wavelength calibrations for the spectrometer; the energy resolution of the CCD and the Bragg angle setting of the crystal. The

CCD energy resolution allows determination of the elements which are present but is not of sufficient resolution for accurate wavelength measurement. The calibration used in practice relies on the identification of a specific line, the distance on the detector from other lines to this "known" line is then measured and their wavelengths can then be determined. The wavelength separation of the lines can be determined from the Bragg angle difference between the lines. However since the tabulation of line wavelengths is to a higher degree of accuracy than the scales on the rotary stages of the crystal and detector, two lines are used for the wavelength calibration and the wavelength separation of individual pixels is then calculated from the wavelength difference between the lines. For the present set up this is $0.17 m\mathring{A}$ *per pixel*. The wavelength separation per pixel is assumed to be constant across the detector.

The intensity calibration is calculated from the total spectrometer sensitivity taking into account the geometry, the crystal and detector efficiencies and the effects of filters, apertures etc.

The charge measured by the ADC is calibrated in terms of photons and energy using a known source. An ^{55}Fe source is placed close to the CCD and the charge collected by the detector in the time integration mode of operation is measured. This gives a calibration of ADC counts per eV from which the number of photons hitting the detector can be calculated if the photon energy is known. This can then be used to give absolute values of spectral line intensities and background count rates.

2.3.1 Spectrometer Sensitivity

The spectrometer sensitivity is the number of photons registered by the detector per unit time compared with the total number emitted by the source. Only photons emitted in a certain solid angle will reach the spectrometer, the efficiencies of the various spectrometer elements then reduces this number further. All these factors must be taken into account in the calculation. The sensitivity is given by [Dunn 1990];

$$\frac{N}{t} = HW sin\theta_B V P_0 \psi_x \psi_y \eta_\lambda Q \frac{E_\lambda \Delta Z}{4\pi}. \qquad (2.8)$$

The equation is best explained by splitting it into a number of parts and explaining each part separately.

The left hand side is the number of photons detected (N) per unit time (t).

We then have an expression for the crystal geometry, H is the crystal height, W is the crystal width and it is turned through the Bragg angle θ_B from the source. This represents the total crystal area seen by the source which is used for diffraction.

An expression is required for the proportion of photons reflected by the crystal which are detected by the detector. V is calculated geometrically to take account of photons which miss the detector. The detector vignetting function is also included here.

P_0 is the peak reflectivity of the crystal. The viewing angle in the plane of dispersion ψ_x is given by $\frac{W sin\theta}{R sin\theta}$ i.e. it is the effective crystal width over the Rowland chord (in radians). ψ_y is the viewing angle perpendicular to the plane of dispersion and is given by the crystal height over the distance from the crystal to the plasma centre. The complete solid angle is therefore included.

η_λ is the total filter transmission at the required wavelength. The filters used here are $2\mu m$ thick polypropylene and aluminised mylar which both have a transmission of $> 90\%$ at $3keV$. Q is the detector quantum efficiency which is $\approx 60\%$ for our CCD at this energy.

The final term represents the x-ray flux emitted by the plasma. E_λ is the emissivity which is usually measured in $photons\ cm^{-3}s^{-1}$. ΔZ (cm) is the effective length of the plasma column emitting the x-rays and the 4π factor represents the solid angle.

$\frac{N}{t}$ can be measured from pulse height analysis of the spectra and hence $\frac{E_\lambda \Delta Z}{4\pi}$ can be found and absolute intensity measurements made.

The instrument sensitivity gives

$$\frac{N}{t} = 7.7 \times 10^{-6} \frac{E_\lambda \Delta Z}{4\pi} photons\ s^{-1} \qquad (2.9)$$

This is accurate to within a factor 2. There are large uncertanties in the crystal reflectivity, the detector quantum efficiency and the geometrical measurements.

As an example, from pulse height analysis we obtain

$$\frac{N}{t} = \frac{1\ C_{ADC}}{2ms} = 4.5 \times 10^4 eVs^{-1} = 16\ photons\ s^{-1} \tag{2.10}$$

where 1 C_{ADC} is a single unit of charge recorded by the ADC of the CCD and the photon energy is 2793 eV.

The sensitivity is calculated here geometrically. An alternative method is to compare the measured continuum intensity in the soft x-ray region with the continuum measured in the visible and extrapolate using an atomic physics and transport code to the spectral region of the measurement [Platz et al 1995]. The two methods agree within $\approx$ 30% [Platz et al 1995].

2.4 Data Analysis

Diagnostic information can be obtained from spectral line widths, intensities and centroid positions. In general these have been found by fitting appropriate line shapes to the spectral lines. For low density discharges where the photon statistics are poor, cross-correlation has been used to find the line centroid positions.

The line shape consists of the convolution of the instrument function with the Doppler broadening of lines due to thermal motion of the plasma. The spectrometer has been set up on a tangential port and thus plasma motion in the toroidal direction will result in a Doppler shift of the line centroid position.

2.4.1 Voigt Profiles

It has already been shown that the instrument function is Lorentzian in shape, the thermal broadening is Gaussian. The convolution of a Lorentzian and a Gaussian is a Voigt function;

$$V(x) = \int L(y)G(x-y)dy. \tag{2.11}$$

The relative weight of the two functions is given by $\eta = \sqrt{\ln 2}\frac{\Delta G}{\Delta L}$, ($\Delta G$ is the Gaussian broadening and ΔL is the Lorentzian broadening). Fitting a Voigt function to a spectral line allows the extraction of the Gaussian width from which the ion temperature can be calculated;

$$\frac{\lambda}{\Delta\lambda} = 13000 \left(\frac{A_i}{T_i}\right)^{\frac{1}{2}}, \tag{2.12}$$

where T_i is the ion temperature in eV, A_i is the ion mass in atomic units and $\Delta\lambda$ is the Gaussian width of the line. The Voigt function has been tabulated by a number of authors including [Tudor Davis and Vaughan 1963].

A number of pseudo Voigt functions (analytical representations of a true Voigt function) have been developed. In this work the following analytical form has been used [Fraser and Suzuki 1970];

$$V(\lambda, a) = \frac{V_0}{\left[1 + (2^{a^2} - 1)\left(2\frac{\lambda - \lambda_0}{\Delta\lambda}\right)^2\right]^{\frac{1}{a^2}}} \tag{2.13}$$

where $0 < a \leq 1$. When $a = 1$ the function is purely Lorentzian and when $a \rightarrow 0$ it is Gaussian. a in (2.13) is not the same as η in (2.11). $\Delta\lambda$ is the FWHM of the line. Figure 2.15 shows a fit of (2.13) to a true Voigt profile.

Equation 2.13 is fitted to the spectral data with a least squares fit using NAG routine E04FDF for the minimisation. The value of χ^2 is returned. The fit requires initial guesses of the line intensity V_0, width $\Delta\lambda$, line centroid position λ_0, background and the value of a. If the fit is not satisfactory, the initial guesses can be changed, this is repeated until χ^2 is minimised. The best fit values of the input parameters are returned and are then used to obtain the relevant plasma parameter.

As a in 2.13 is not a direct measure of the Gaussian weighting of the profile, the tables of [Tudor Davis and Vaughan 1963] are used to extract the Gaussian width from the returned value of the FWHM width using the assumed instrument width as the Lorentzian contribution. The values of the Lorentzian and Gaussian widths in the tables can be fitted with the following polynomial expression

$$y = -2.8676x^4 + 5.1299x^3 - 3.3935x^2 + 0.2787x + 0.9377 \tag{2.14}$$

where x is the Lorentzian fraction and y is the Gaussian fraction of the line width.

The main errors in the final result are the uncertainty in the instrument function and the quality of the fit. The error due to the uncertainty in the instrument function is a systematic error which is reduced as the ion temperature rises. In typical COMPASS-D conditions where T_i ranges from $\approx 100eV - 300eV$, the line widths vary from $\approx 10 - 13$ pixels and the instrument width is ≈ 9.5

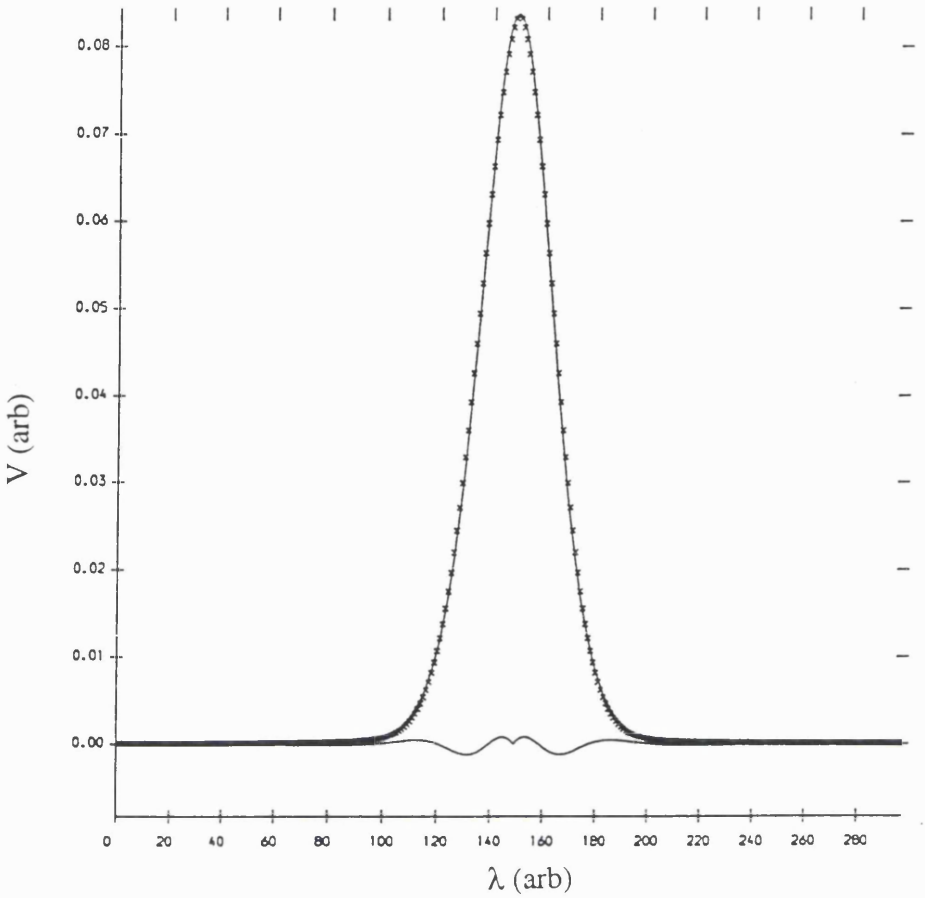

Figure 2.15: *Fit of approximate Voigt function to true Voigt function. The points are generated from a true Voigt function, the line which represents the approximate function is then fitted to the points. Also shown are the residuals to the fit.*

pixels. Temperatures below $\approx 100eV$ cannot be measured. The error due to the quality of the fit is essentially a random error, but can be reduced by increasing photon statistics, i.e. by summing spectra together. For rotating plasmas where the line centroid is moving, care must be taken when summing spectra together.

2.4.2 Other Broadening Mechanisms

The Stark effect is the splitting of energy levels in the presence of an electric field. For a detailed treatment of the Stark effect see [Griem 1964]. Two different approaches can be used to calculate Stark broadening. The impact approximation assumes that the ion is continuously radiating, but occasional collisions do occur

which interrupt the wave train. If τ is the mean free time between collisions, a Lorentzian broadening of FWHM proportional to $\frac{1}{\tau}$ is produced.

The quasi-static approximation assumes that the emitting and perturbing ions are stationary for the duration of the emission. In the simplest approximation, a single perturbing ion is located within a radius r to $r + \delta r$ of the emitter such that the electric field contributions from other ions are the same as or smaller than that from the original perturber. The probability of a spectral line being affected by the presence of the perturbing ion is proportional to the volume of the spherical shell i.e. $4\pi r^2 dr$. The wavelength shift, $\delta\lambda$, is proportional to the electric field strength ($E \propto r^{-2}$). The shape of the broadening can then be shown to be

$$I(\lambda) \propto E^{-\frac{5}{2}} dE, \tag{2.15}$$

and the line width to be

$$\Delta\lambda \propto n_i^{\frac{2}{3}}. \tag{2.16}$$

n_i is the ion density.

The electric field strength of the perturbing ions is given by the Holtzmark field [Griem 1964];

$$F_0 = 1.3 \times 10^{-8} n_i^{\frac{2}{3}} \; V m^{-1}. \tag{2.17}$$

In typical COMPASS-D conditions with $n_i = n_e = 5 \times 10^{-19} m^{-3}$, this gives $F_0 = 175 kV m^{-1}$. The electric field due to thermal motion of the plasma ions $(\mathbf{V} \times \mathbf{B})$ is given by;

$$F_t = \left(\frac{8eT_i}{\pi m_i}\right)^{\frac{1}{2}} B \; V m^{-1}, \tag{2.18}$$

where e is the electronic charge, T_i is the ion temperature in eV, m_i is the ion mass in kg, and B is the magnetic field in T. For D ions at a temperature of 200 eV and with $B = 1.5T$, $F_t = 235 kV m^{-1}$. The Holtzmark field and the thermal motion fields are thus similar in magnitude.

For the hydrogen atom the linear Stark effect (first order in the electric field) is important, for other atoms it is insignificant but the quadratic Start effect (proportional to E^2) becomes relevant. The quadratic Stark effect becomes more important at high n levels of the atom.

The Stark broadening as, shown in equation (2.16), increases with increasing density. At typical tokamak densities, the broadening of low n x-ray lines is negligible compared with Doppler broadening [DeMichelis and Mattioli 1981].

The Zeeman effect is the splitting of energy levels in the presence of a magnetic field. The wavelength shift due to Zeeman splitting is given by [Griem 1964];

$$\delta\lambda = \lambda^2 \times 10^{-8} B \; nm \tag{2.19}$$

where λ is the wavelength in nm and B is the field strength in T. For x-ray wavelengths in typical tokamak conditions, this effect is negligible.

Tokamak plasmas are considered to be optically thin at x-ray wavelengths, opacity effects are negligible and are not taken into account [DeMichelis and Mattioli 1981].

2.4.3 Cross-Correlation

In some low density plasma experiments ($n_e < 2\times10^{19}m^{-3}$) there is an interest in measuring changes in plasma core rotation. However for many of these plasmas photon statistics are too poor to obtain satisfactory line fits. Cross-correlation is then used to detect shifts in the line centroid position [Carolan 1994]. A spectrum with good photon statistics is chosen as a standard and the spectra of interest (with low photon statistics) are then compared with it. The correlation function is given by

$$A(\Delta\lambda) = \frac{\int G(\lambda)H(\lambda-\Delta\lambda)d\lambda}{\int G(\lambda)d\lambda \int H(\lambda)d\lambda}, \tag{2.20}$$

where $G(\lambda)$ is the standard spectrum and $H(\lambda)$ is the spectrum of interest. The whole spectrum is used for the correlation. $G(\lambda)$ is held in position whilst $H(\lambda)$ is shifted in one pixel steps from 20 pixels on the short wavelength side of $G(\lambda)$ to 20 pixels on the long wavelength side, $A(\Delta\lambda)$ is calculated at each step and the maximum of $A(\Delta\lambda)$ is the centroid position. The maximum is found by fitting a degree six polynomial to $A(\Delta\lambda)$. Figure 2.16 shows a cross-correlation of a spectrum with a standard spectrum. Care must be taken to ensure that the standard spectrum is similar in shape to the spectrum of interest as differences in shape can move the maximum.

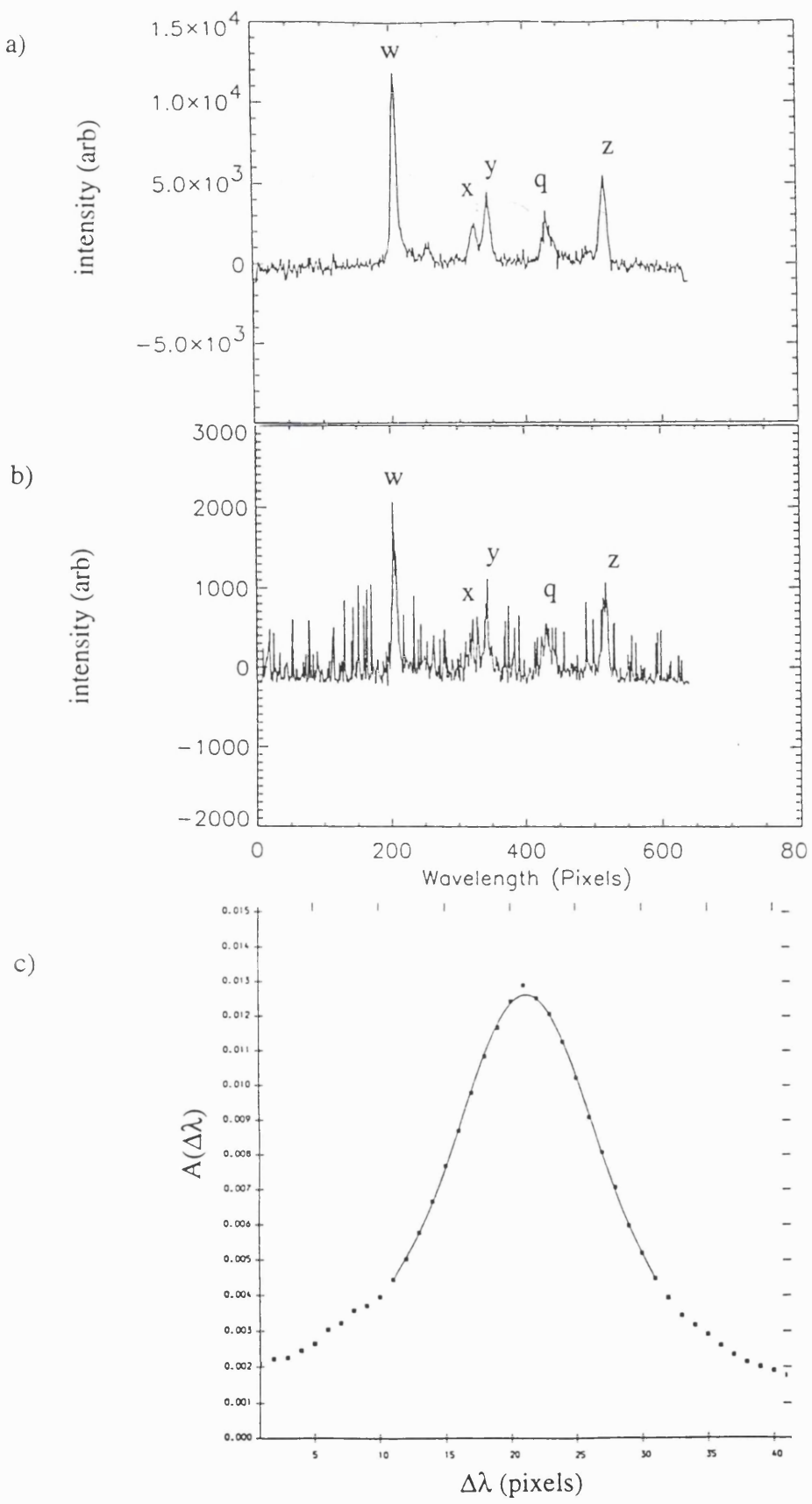

Figure 2.16: *a) Example of a standard spectrum used for low density data analysis, this spectrum has been produced by the addition of a number of low density spectra. The line notation is from [Gabriel 1972]. b) Noisy spectrum taken from a 10 ms time slice from a low density plasma shot #13595. c) The cross-correlation of the two spectra in a) and b).*

Chapter 3

The He-Like Spectrum

The He- like charge state has the largest abundance for the widest temperature range of any isoelectronic sequence. He- like ions have traditionally been studied and used as diagnostics of both astrophysical and laboratory plasmas. The atomic physics is known to a good degree of accuracy and can be used to enhance the diagnostic potential of spectroscopic measurements.

High resolution He- like spectra of mid Z elements were first observed from solar active regions [Parkinson 1972] and flares [Grineva et al 1973] from spectrometers on board SOLFLEX [Doschek et al 1979] and Solar Maximum Mission [Gabriel et al 1981]. More recently such spectra have been observed from tokamak plasmas. Tokamak plasmas are the best diagnosed low density, high temperature plasmas and therefore such observations have a two fold interest; firstly, comparison with other diagnostics can be used as a test of the atomic theory, for example electron temperature dependent line intensity ratios can be compared with laser scattering measurements, giving a greater degree of confidence in the diagnosis of astrophysical plasmas where no other measurements are available. The second use of course is for diagnosis of the tokamak plasmas themselves.

The relevant atomic physics was first set out by Gabriel [Gabriel 1972] and many workers since have made improvements to the theory by improving calculations of the rate coefficients, by the addition of other population mechanisms [Pradhan 1985] and also by improving wavelength calculations [Drake 1988]. Line intensity calculations require the relevant rate coefficient for the process

involved whilst taking into account any effects from other processes, for example additional ionisation and recombination mechanisms. Line blending, especially due to unresolved satellite lines must also be taken into account when analysing spectra.

Tokamaks contain trace amounts ($< 0.1\%$) of mid Z ($Z = 9 \rightarrow 28$) elements. These impurities in general originate from the vessel wall or limiters. Impurities can also be introduced deliberately into the plasma for diagnostic purposes either by laser ablation or by gas puffing. These elements are often only partially ionised and exist in various ionisation stages across the temperature gradient, transport codes are used to model the plasma and to determine the positions of the ionisation stage shells. The observed spectra from these shells can be used to diagnose the plasma.

This thesis discusses the observation of He- like Cl (Cl XVI) and its satellites ($4.4\mathring{A} - 4.5\mathring{A}$) from the COMPASS-D tokamak. Chlorine is an intrinsic impurity and is assumed to be sputtered into the plasma from the vessel wall. COMPASS-D has relatively low electron temperature (500 eV - 1000 eV) (in ohmic operation) and ion temperature (100 eV - 400 eV). The low electron temperatures produce relatively intense satellite lines and the low ion temperatures produce narrow lines. These two effects combine to enable resolution of a number of satellites which are not resolved in higher temperature tokamaks. The wavelengths and intensities of these lines can be measured and compared with theory.

The $n = 2$ He- like spectrum consists of four main lines excited from the He-like ground state. The most intense line is the He- like resonance line $1s^2\ ^1S_0 - 1s2p\ ^1P_1$, labelled w by Gabriel [Gabriel 1972] and is an electric dipole (E1) transition, the intensity scaling as Z^4. There are two intercombination lines $1s^2\ ^1S_0 - 1s2p\ ^3P_2$ and $1s^2\ ^1S_0 - 1s2p\ ^3P_1$ labelled x and y respectively. x is a magnetic quadropole (M2) transition, the intensity scales as Z^8 and y is an electric dipole (E1) transition scaling as Z^9. The fourth line is a forbidden line, $1s^2\ ^1S_0 - 1s2p\ ^3S_1$ labelled z which is a magnetic dipole (M1) transition scaling as Z^{10}. In addition to these lines a typical spectrum will also contain a number of dielectronic and inner shell excitation satellite lines of the type $1s^2nl - 1s2l'nl''$ where $n \geq 2$.

A third recombination line is occasionally seen [Coffey 1993] $1s^2\ ^1S_0$ – $1s2p^3P_0$ which is a nuclear spin allowed transition. An energy level diagram of these lines (including the more intense satellite lines) is shown in Figure 3.1. The three intercombination levels also decay to the $^3S_1$ producing line emission in the UV region.

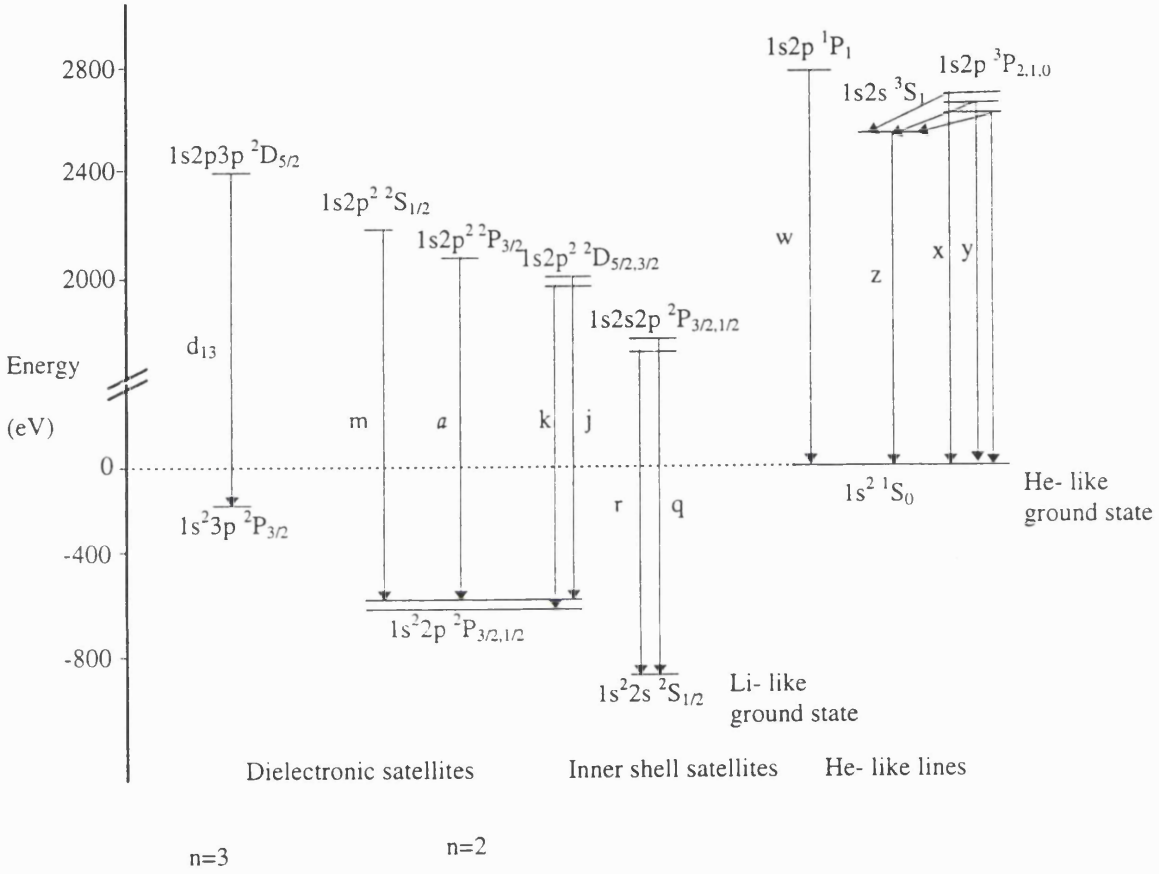

Figure 3.1: *Energy level diagram of a He- like system showing the four He- like lines and the main satellite lines due to inner shell excitation and dielectronic recombination. The labelling is according to [Gabriel 1972].*

3.1 Line Intensities and Ratios

3.1.1 He- Like Lines

The intensity of the w line is given by;

$$I_w = N_w A_w = n_e n_I C_w(T_e), \tag{3.1}$$

where N_w is the excited state population, A_w is the radiative decay rate to the ground state, n_I is the impurity density (in this case the He- like ground state density) and $C_w(T_e)$ is the excitation rate. This is true at low densities where the main collisional process is electron impact excitation: at higher densities, other effects must be taken into account as well. The excitation rate $C_w(T_e)$ is the collision cross section averaged over the Maxwellian velocity distribution function;

$$C_w(T_e) =< \sigma_w v > . \tag{3.2}$$

The interpretation of spectral line intensities is a problem requiring a knowledge of charge state distributions and excited level populations. The relative distribution of the charge state intensities are found from the solutions to the coronal equilibrium equation taking into account any departure from equilibrium and impurity transport effects - this is done in practice using a transport code.

In tokamak conditions there will be an overlapping of neighbouring charge states and recombination and ionisation must also be taken into account. Thus the total line intensity will be given by;

$$I_w = n_e n_I \left\{ C_w(T_e) + \alpha \frac{n_H}{n_I} + S \frac{n_{Li}}{n_I} \right\}, \tag{3.3}$$

where α is the recombination rate and S is the ionisation rate. n_H is the H- like ground state density and n_{Li} is the Li- like ground state density.

There are a number of approaches available for the calculation of the excitation rates and cross sections. These approaches include the R Matrix method and distorted wave approximation as the more accurate methods. Simpler analytical approximations have also been used. A review of these methods can be found in [Henry 1981].

The simplest approximation is given by Van Regemorter, which uses the Bethe approximation for the high energy limit of the Born approximation, i.e. the plane wave of the Born approximation is replaced by a slowly varying Gaunt factor $g(E)$ [Van Regemorter 1962];

$$\sigma_{ij} = \frac{8\pi}{\sqrt{3}} \frac{\chi_H^2}{E_{ij} E} f_{ij} g(E) \pi a_0^2. \tag{3.4}$$

$f_(ij)$ is the optical oscillator strength. E_{ij} is the transition energy, a_0 is the Bohr radius. At high energies this approximation tends towards the Bethe formula for

the excitation rate. Using this approximation the collision rate becomes

$$C_{ij}(T_e) = 3.15 \times 10^{-7} f_{ij} \overline{g} \frac{\chi_H}{E_{ij}} \left(\frac{\chi_H}{T_e}\right)^{\frac{1}{2}} \exp\left(\frac{-E_{ij}}{T_e}\right) cm^3 s^{-1}, \qquad (3.5)$$

where $\overline{g}$ is $g(E)$ averaged over a Maxwellian distribution, for $T_e < E_{ij}$, $\overline{g} \approx 0.2$.

Another approach has been used by Keenan [Keenan et al 1987] in which a polynomial fit is used for γ_{ij}, the effective collision strength. Starting with accurate R Matrix results for O VII and Mg XI and distorted wave calculations for Ca XIX and Fe XXV, γ_{ij} has been calculated for all values of Z between O and Fe and the polynomial fit is given by;

$$\gamma_{ij}(T_e) = a_0 + a_1 log(T_e) + a_2 [log T_e]^2, \qquad (3.6)$$

where $a_0 = 1.5220 \times 10^{-1}$, $a_1 = -4.6154 \times 10^{-2}$ and $a_2 = 3.6464 \times 10^{-3}$ for the Cl XVI w line. The results obtained agree to within 1% of the original data. The excitation rate can then be calculated from;

$$C_w(T_e) = \frac{8.63 \times 10^{-6}}{g_i T_e^{\frac{1}{2}}} \gamma_{ij}(T_e) exp\left(\frac{-E_w}{T_e}\right). \qquad (3.7)$$

E_w is the transition energy of the w line and g_i is the statistical weight of the ground state level.

The intensities of the intercombination and forbidden lines, x, y and z, are also dependent on the excited level populations and on the relevant collision rates in the same way as the w line, but the collision strengths for these lines are weaker. Other effects must also be considered for these lines. It has been shown for Fe XXV [Bely-Dubau et al 1982a] that the excitation of the z line can be increased by a factor of two due to cascades from $n \geq 3$ levels whilst increasing the w line by only 5%. It has also been shown that the z line is also increased the most by resonances [Pradhan 1985].

There is much experimental evidence to show that calculations of the line intensities from direct excitation alone is not sufficient [Bitter et al 1985]. When adding in the effects of recombination, cascades and inner shell ionisation, good agreement is achieved for light elements but for heavier elements, $Z > 15$ there are still significant differences between experiment and theory, especially for $T_e < 1KeV$.

The line intensities given by equations such as equation (3.1) assume that the excited levels are populated mainly by electron impact excitation and decay through radiative transitions. However if $A_{ij} \leq n_e C(T_e)$, which becomes true as the density increases, then the long lived metastable states are depleted by collisional transitions to nearby levels. This begins to occur for the Cl z line at $n_e \approx 10^{20} m^{-3}$, as collisions depopulate the $^3S_1$ metastable level to the ^3P levels. The density sensitive R ratio is defined as

$$R = \frac{z}{x + y}. \tag{3.8}$$

COMPASS-D maximum electron densities are only just bordering on the density sensitive range, and therefore this diagnostic has not been used here for density determination.

The electron temperature dependence of the collision rates allows the G ratio;

$$G = \frac{x + y + z}{w}, \tag{3.9}$$

to be used as an electron temperature diagnostic. The electron density dependence of the triplet states does not affect this ratio as it merely represents a redistribution of the same population amongst these levels. The R ratio also has an electron temperature dependence due to the collision rates.

Any enhancement of the triplet line intensities due to recombination and ionisation will be dependent on the ionisation balance and on the impurity ion transport, hence departures from coronal equilibrium can be observed by measurement of these ratios.

3.1.2 Dielectronic Satellite Lines

The mechanism of dielectronic recombination has already been described in chapter 1. The population of the satellite state can be calculated by assuming that the population and depopulation mechanisms are in balance;

$$n_I n_e C_d(T_e) = N_d \left(A_a + \Sigma A_r \right), \tag{3.10}$$

where n_I is the ground state density, $C_d(T_e)$ is the capture rate, N_d is the excited level density, A_a is the autoionisation rate and A_r is the radiative decay rate.

The capture rate is calculated using the assumption that, in the absence of other processes, dielectronic recombination must be balanced by its inverse process, autoionisation. The line intensity is then given by;

$$I_d = C_d(T_e) n_I n_e \frac{A_r}{A_a + \Sigma A_r}. \tag{3.11}$$

The ratio of the dielectronic satellite line intensity to the He- like resonance line is;

$$\frac{I_d}{I_w} = \frac{C_d(T_e)}{C_w(T_e)} q_s, \tag{3.12}$$

where

$$q_s = \frac{A_r}{A_a + \Sigma A_r} \tag{3.13}$$

is the satellite intensity factor. The ratio is electron temperature dependent through the excitation / capture rates and has no electron density or ionisation balance dependence thus making it a very useful electron temperature diagnostic.

The radiative decay rate scales as Z^4 whereas the autoionisation rate remains constant as Z increases, and thus for mid and high Z elements the dielectronic satellites are very prominent and at COMPASS-D temperatures, the most intense dielectronic satellites of Cl XVI are in the order of $\approx$ 15% of the resonance line intensity.

Dielectronic satellites of the type $1s^2nl - 1s2l'nl''$ where $n \geq 3$ produce a series of lines close to and converging on the long wavelength side of the resonance line. These lines at low electron temperatures can cause a number of effects. They increase the apparent intensity and width of the resonance line and change its centroid position giving an apparent red shift. These lines must therefore be taken into account when using any line ratio and Doppler measurements involving the resonance line. The theory for the modelling of these line for Ti XXI is given by [Bely-Dubau et al 1982b, Bitter et al 1985]. For the intensity contribution of the dielectronic satellite lines to the apparent resonance line intensity [Bely-Dubau et al 1982b] give the following model;

$$\Delta I_w = \alpha(T_e) I_w, \tag{3.14}$$

where

$$\alpha(T_e) = \frac{\Sigma I_d}{I_w}, \tag{3.15}$$

and is shown in Figure 3.2. ΔI_w is the apparent increase in intensity of the resonance line. The two curves shown in the figure are for Ti XXI from [Bely-Dubau et al 1982b] and for Cl XVI using the dielectronic satellite data of [Vainshtein and Safronova 1980] assuming a spectrometer with $\frac{\lambda}{\delta\lambda} \approx 3000$.

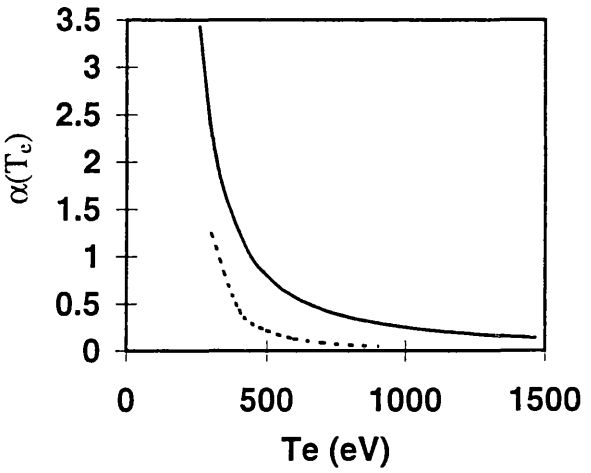

Figure 3.2: *Apparent changes to the resonance line intensity due to dielectronic satellites, Ti XXI (full line) from [Bely-Dubau et al 1982b] and Cl XVI dashed line (The Cl data includes only dielectronic satellites $n \leq 3$).*

It is often preferable to make Doppler measurements on other lines if available, even if they are less intense, as the modelling of other line blends is usually much more straightforward. However it has been shown that complete modelling of the high n satellite lines does lead to the use of the resonance line with good accuracy [Bitter et al 1985].

Figure 3.3 shows the Maxwell averaged collision rate for the Cl w line. It is clear from the figure that if the electron distribution becomes non-Maxwellian, the w line intensity can be altered by the change of shape of the tail. The dielectronic satellites are not affected by the tail as they are only excited by a very narrow energy range and therefore the dielectronic satellite to resonance line ratio can also be used to measure non-Maxwellian electron distributions.

The Holtzmark field, as described in section 2.4.2, can enhance the dielectronic capture rate by Stark mixing of the high n states. It has been shown [Badnell et al 1993] that this is only important for high n satellites ($n > 40$).

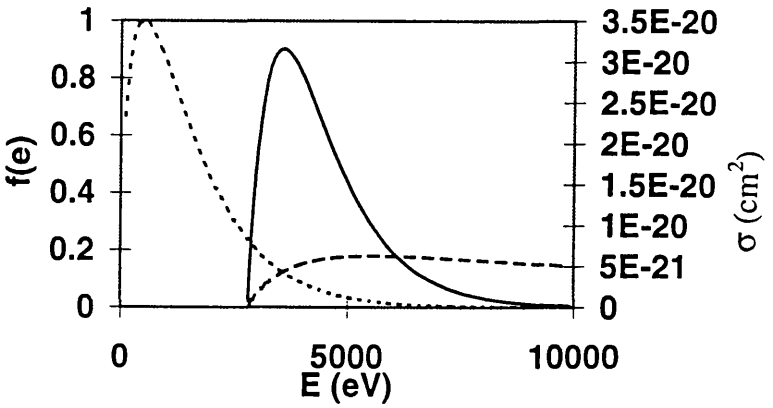

Figure 3.3: *The Maxwellian averaged excitation rate for the Cl XVI w line (full line), also shown is the electron energy distribution for $T_e = 1keV$ (dotted line) and the excitation cross section σ (dashed line). The cross section was calculated using the Van Regemorter approximation [Van Regemorter 1962].*

These effects are also very small at typical tokamak electron densities [Dickson 1993].

3.1.3 Inner Shell Excitation Satellite Lines

Inner shell excitation is only important for n=2 levels. The method of excitation is electron impact and the population of the upper level is given by the balance between collisional excitation from the ground state and the total decay rate. The line intensity is given by;

$$I_{is} = n_{Li} n_e C_{is}(T_e) \frac{A_r}{A_a + \Sigma A_r}. \tag{3.16}$$

The collision rate can be calculated using similar methods to those discussed for the resonance line. The lines are excited from the Li- like ground state and the intensity is proportional to the Li- like ground state density. The ratio of the inner shell satellite intensity to the resonance line intensity is given by;

$$\frac{I_{is}}{I_w} = \frac{n_{Li}}{n_{He}} \frac{C_{is}(T_e)}{C_w(T_e)} \frac{A_r}{A_a + \Sigma A_r}. \tag{3.17}$$

n_{Li} is the Li- like ground state density and n_{He} is the He- like ground state density. The ratio has an electron temperature dependence through the collision rates, and also has a dependence on the ratio of the Li- like ground state

density to the He- like ground state density from which departure from coronal equilibrium can be detected and hence this ratio can be used as a diagnostic of impurity ion transport.

Many satellites have a contribution from both dielectronic recombination and inner shell excitation, and therefore when using these satellite line ratios both mechanisms must be taken into account when appropriate.

3.2 Line Wavelengths

Hydrogenic wavelengths are calculated from Dirac theory which is based on the Schrödinger equation with relativistic effects included, QED effects are added in afterwards. This method agrees with experiment with good accuracy [Mohr 1983]. For multi electron atoms e.g. He- like systems where the extra effects of electron shielding must be included, there is no exact solution to the Dirac equation. One approach to solving the problem is the $1/Z$ expansion method used by [Vainshtein and Safronova 1978] in which the non-relativistic Hamiltonian is separated into two parts; one representing the single electron hydrogenic ion and the other the electron - electron interaction;

$$H = Z^2 \left(H_0 + \frac{1}{Z} V \right), \tag{3.18}$$

where V represents the electron - electron interaction. Relativistic and QED effects are then added separately by means of the Breit operator.

The various contributions to the energies of He- like ions for $2 \leq Z \leq 100$ have been calculated [Drake 1988] and are shown in Figure 3.4 for the w, x, y and z lines for the range of typical tokamak impurities $2 \leq Z \leq 28$. The figures show that for these lines for low and mid Z elements the relativistic and QED corrections are small compared with the non-relativistic contribution. Relativistic corrections are in the order of 10^{-3} of the total wavelength for Cl and the QED corrections are a factor of ten lower. A spectrometer with $\frac{\lambda}{\delta\lambda} \approx$ 3000 should thus be able to resolve the relativistic effects but not the QED effects. For more accurate measurement of the QED effects measurement of the $1s2s^3S_1 - 1s2p^3P_{2,0}$ lines would be preferable as for Cl the QED corrections are of the order 10^{-3}. These lines at $614\mathring{A}$ and $706\mathring{A}$ are unfortunately blended with

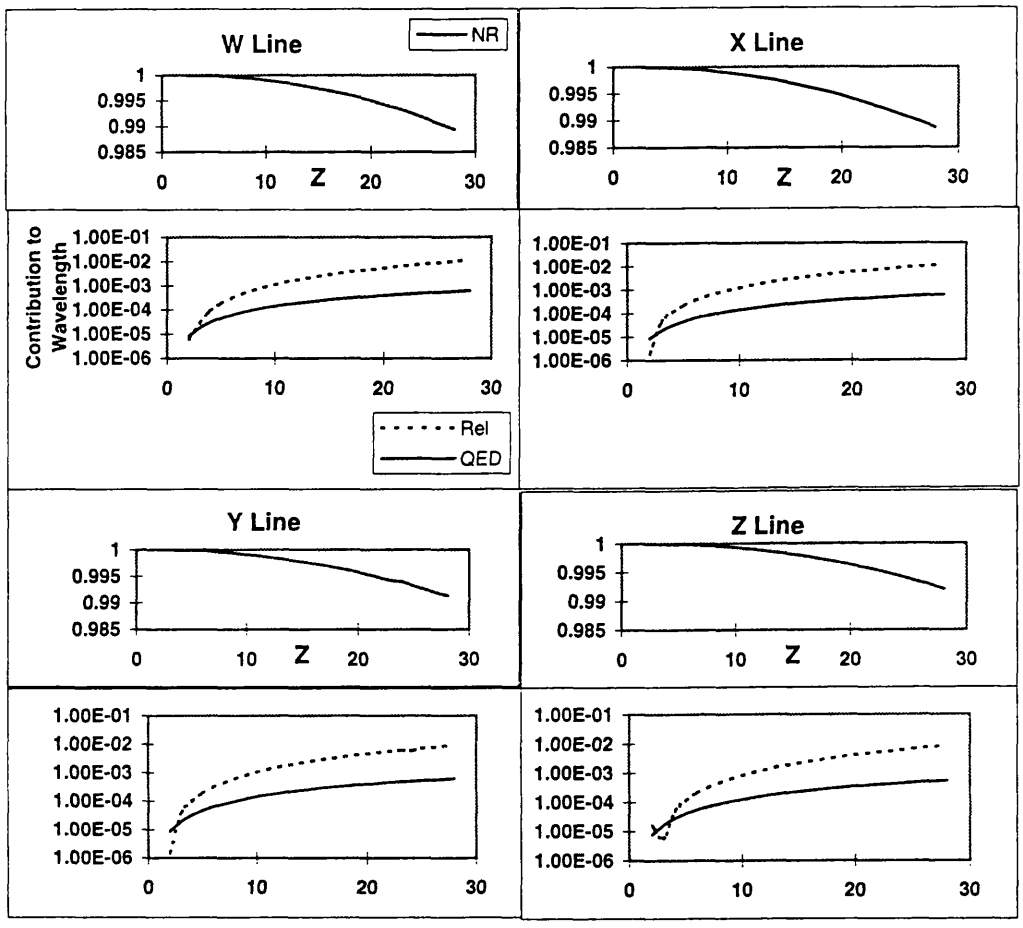

Figure 3.4: *Non relativistic (NR), relativistic (Rel) and QED contributions to the w, x, y and z line wavelengths for* $2 \leq Z \leq 28$, *from[Drake 1988]*

various oxygen lines on COMPASS-D, but have been measured on a tandem accelerator using beam foil excitation [DeSerio et al 1981].

Table 3.1: *Wavelengths and satellite intensity factors for spectral fitting. The inner shell ratio is the contribution to the line intensity due to inner shell excitation as a fraction of the q line.*

Line Notation	Configuration	λ Theor. ($\AA$)	λ Fitted ($\AA$)	Satellite Intensity Factor q_s	Inner Shell Ratio
w	$1s^2\ ^1S_0 - 1s2p^1P_1$	4.4436	4.4436	-	-
h_{17}	$1s^23d\ ^2D_{\frac{3}{2}} - 1s2p[^1p]3d\ ^2F_{\frac{5}{2}}$	4.4437	4.4437	5.53	-
h_{16}	$1s^23d\ ^2D_{\frac{5}{2}} - 1s2p[^1p]3d\ ^2F_{\frac{5}{2}}$	4.4441	4.4441	1.24	-
h_{15}	$1s^23d\ ^2D_{\frac{5}{2}} - 1s2p[^1p]3d\ ^2F_{\frac{7}{2}}$	4.4452	4.4452	9.57	-
d_8	$1s^23p\ ^2P_{\frac{3}{2}} - 1s2p[^1p]3p\ ^2P_{\frac{3}{2}}$	4.4504	4.4504	1.68	-
a_1	$1s^23s\ ^2S_{\frac{1}{2}} - 1s2p[^1p]3s\ ^2P_{\frac{3}{2}}$	4.4504	4.4504	1.64	-
d_{14}	$1s^23p\ ^2P_{\frac{3}{2}} - 1s2p[^1p]3p\ ^2D_{\frac{3}{2}}$	4.4508	4.4508	6.68	-
d_{13}	$1s^23p\ ^2P_{\frac{3}{2}} - 1s2p[^1p]3p\ ^2D_{\frac{5}{2}}$	4.4518	4.4523	12.4	-
a_3	$1s^23s\ ^2S_{\frac{1}{2}} - 1s2p[^3p]3s\ ^2P_{\frac{3}{2}}$	4.4591	4.4591	1.11	-
m	$1s^22p\ ^2P_{\frac{3}{2}} - 1s2p^2\ ^2S_{\frac{1}{2}}$	4.4593	4.4593	1.18	-
n	$1s^22p\ ^2P_{\frac{1}{2}} - 1s2p^2\ ^2S_{\frac{1}{2}}$	4.4633	4.4633	2.92	-
x	$1s^2\ ^1S_0 - 1s2p^3P_2$	4.4636	4.4636	-	-
h_{18}	$1s^23d\ ^2D_{\frac{5}{2}} - 1s2p[^3p]3d\ ^2F_{\frac{7}{2}}$	4.4637	4.4637	2.36	-
s	$1s^22s\ ^2S_{\frac{1}{2}} - 1s2s[^3p]2p\ ^2P_{\frac{3}{2}}$	4.4659	4.4659	1.51	0.06
t	$1s^22s\ ^2S_{\frac{1}{2}} - 1s2s[^3p]2p\ ^2P_{\frac{1}{2}}$	4.4667	4.4667	2.38	0.09
h_{19}	$1s^23d\ ^2D_{\frac{5}{2}} - 1s2p[^3p]3d\ ^2F_{\frac{5}{2}}$	4.4668	4.4668	1.40	-
y	$1s^2\ ^1S_0 - 1s2p^3P_1$	4.4669	4.4669	-	-
$^3P_0$	$1s^2\ ^1S_0 - 1s2p^3P_0$	4.4688	4.4688	-	-
q	$1s^22s\ ^2S_{\frac{1}{2}} - 1s2s[^1p]2p\ ^2P_{\frac{3}{2}}$	4.4822	4.4822	0.679	1.00
b	$1s^22p\ ^2P_{\frac{1}{2}} - 1s2p^2\ ^2S_{\frac{1}{2}}$	4.4836	4.4836	1.94	-
r	$1s^22s\ ^2S_{\frac{1}{2}} - 1s2s[^1p]2p\ ^2P_{\frac{1}{2}}$	4.4842	4.4842	1.92	0.44
a	$1s^22p\ ^2P_{\frac{3}{2}} - 1s2p^2\ ^2P_{\frac{3}{2}}$	4.4876	4.4876	3.76	-
k	$1s^22p\ ^2P_{\frac{1}{2}} - 1s2p^2\ ^2D_{\frac{2}{2}}$	4.4927	4.4927	14.5	-
z	$1s^2\ ^1S_0 - 1s2p^3P_0$	4.4965	4.4965	-	-
j	$1s^22p\ ^2P_{\frac{3}{2}} - 1s2p^2\ ^2D_{\frac{5}{2}}$	4.4968	4.4968	20.0	-

3.3 Spectral Analysis

This section shows how the spectral fitting routines described in chapter 2 and the atomic physics discussed in this chapter are used to interpret a spectrum.

Figure 3.5 shows a fit of twenty five Voigt profiles to a typical Cl XVI spectrum from COMPASS-D. The wavelengths of the He- like lines, in-

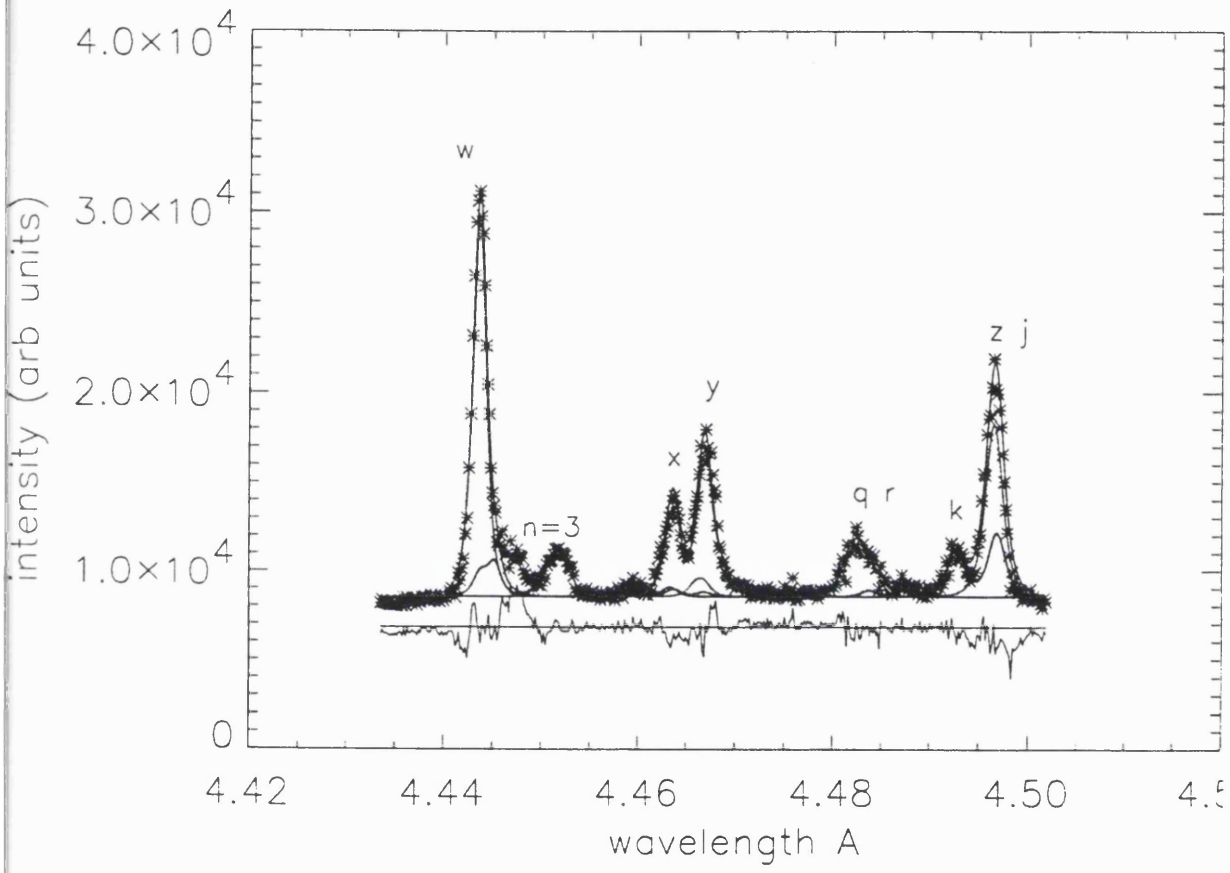

Figure 3.5: *ClXVI spectrum fitted with twenty five Voigt profiles from COMPASS-D shot #14096. The line notation is according to [Gabriel 1972].*

ner shell excitation satellites and n=2 dielectronic satellites are taken from [Vainshtein and Safronova 1978] and so too are the satellite intensity factors for the n=2 dielectronic satellites. The wavelengths and satellite intensity factors for the n=3 dielectronic satellite lines are from [Vainshtein and Safronova 1980]. The wavelength of the $1s^2\ ^1S_0 - 1s2p^3P_0$ line was taken from [Drake 1988], there is a slight discrepancy in the wavelengths of the He- like lines between [Drake 1988] and [Vainshtein and Safronova 1978], the data of Vainshtein and

Safronova was chosen in preference as they also provide satellite data. The discrepancy between the two data sets is fairly constant for all four He- like lines, thus the choice will have little effect on the quality of the fit. The satellite intensity factors for the inner shell excitation satellites were taken from the ADAS code [Summers 1994]. The wavelengths and satellite intensity factors used for the fit are given in Table 3.1.

The fits are carried out as follows; the k line is a pure dielectronic satellite line and the q line is virtually a pure inner shell excitation satellite with very little contribution from dielectronic recombination. Both of these lines are well resolved. Initial guesses for their intensities are taken from the raw data and the initial guesses for the remaining satellites are then calculated via the satellite intensity factors from these two lines, taking into account the vignetting function. Initial guesses for the He- like line intensities are then taken from the difference between the raw data and the initial guesses for the satellite intensities. The fit is then carried out (with these initial starting points) allowing the intensities to float, all widths are assumed to be constant, two wavelengths are allowed to float (w and z), the rest are assumed to be constant offsets from these, the background is allowed to float.

Figure 3.6 shows the separate contributions from the He- like lines and the various satellites. The theoretical and measured wavelenths are shown in Table 3.1. The only discrepancy in wavelength between the measured and theoretical values is the d_{13} line. However there is no data for the $n \geq 4$ lines, these lines on the long wavelength side of the w line have not been fitted, and this will result in an error in the intensities of the w line and the $n = 3$ satellite lines. Table 3.2 shows the measured line ratios obtained from the spectrum shown in Figure 3.5. The q/w ratio includes a correction for the small dielectronic contribution. The effects of the vignetting function are also taken into account.

Doppler measurements are made from a fit to just three of the lines, k, z, and j. The fitting procedure is similar to that for the complete spectrum. The initial value of the k line intensity is measured from the raw data and the initial j intensity is calculated from the ratio of the satellite intensity factors, the z intensity is taken initially as the remainder. Only one width and wavelength

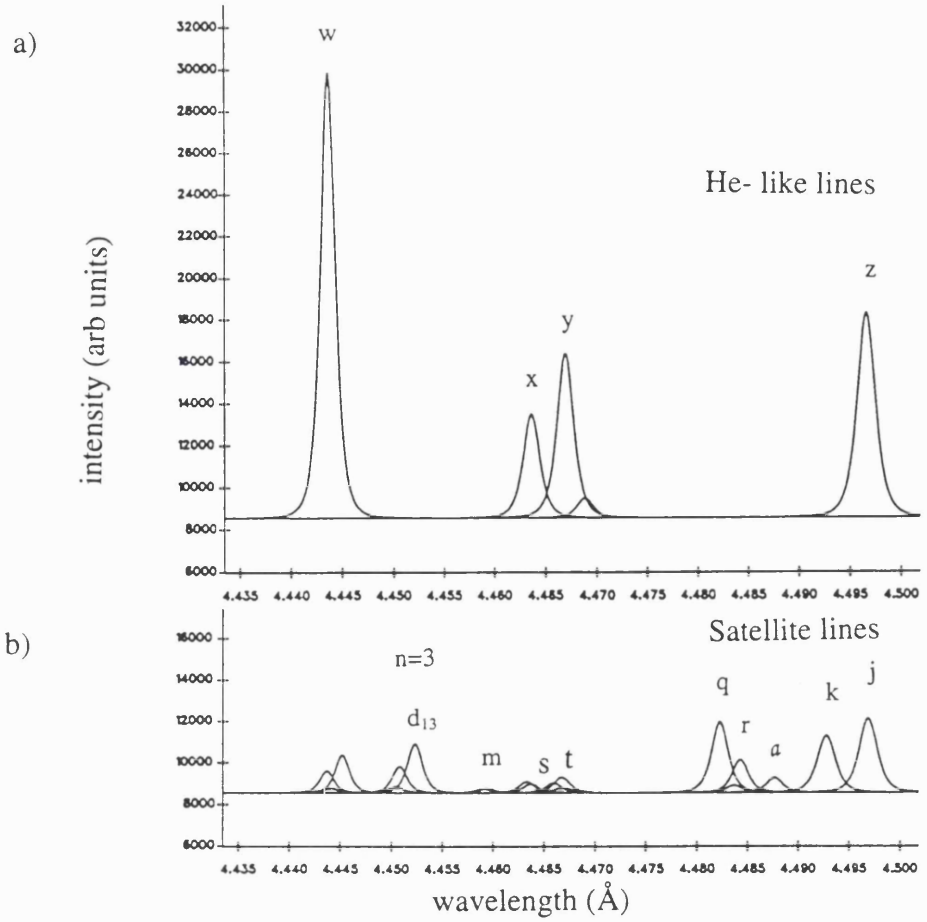

Figure 3.6: *a) He- like lines and b) satellite lines from COMPASS-D #14096*

are used, the background is also fitted. The fit is carried out with eleven input parameters, five of which are free (one width, one position, one background and two intensities). The parameter a from equation 2.13 is also fitted. Figure 3.7 shows a fit to these lines.

Cross-correlation is used for looking for Doppler shifts in low density, noisy spectra. Differences in the line ratios between the standard spectrum and the test spectra cause apparent shifts. Synthetic spectra were generated for coronal conditions at different electron temperatures, thus varying the line ratios. Spectra were generated at 100 eV intervals from 500 eV to 900 eV. Each of the spectra were then cross-correlated with the 700 eV spectrum. The results are shown in Figure 3.8. The apparent shift can be the same size as the Doppler shifts seen in practice. The effect can be minimised with careful choice of standard spectra which are as close as possible in shape to the test spectra. For example, the standard spectrum can be generated by adding together a number of similar noisy spectra obtained from the same conditions as the spectrum of interest.

Table 3.2: *Measured line ratios and plasma parameters from the spectrum shown in Figure 3.5, COMPASS-D shot #14096.*

Ratio	Value
G	0.86
R	1.14
$\frac{q}{w}$	0.10
$\frac{k}{w}$	0.11
$T_e(\frac{k}{w})(eV)$	900
Line width (pixels)	11.8
$T_i(eV)$	222

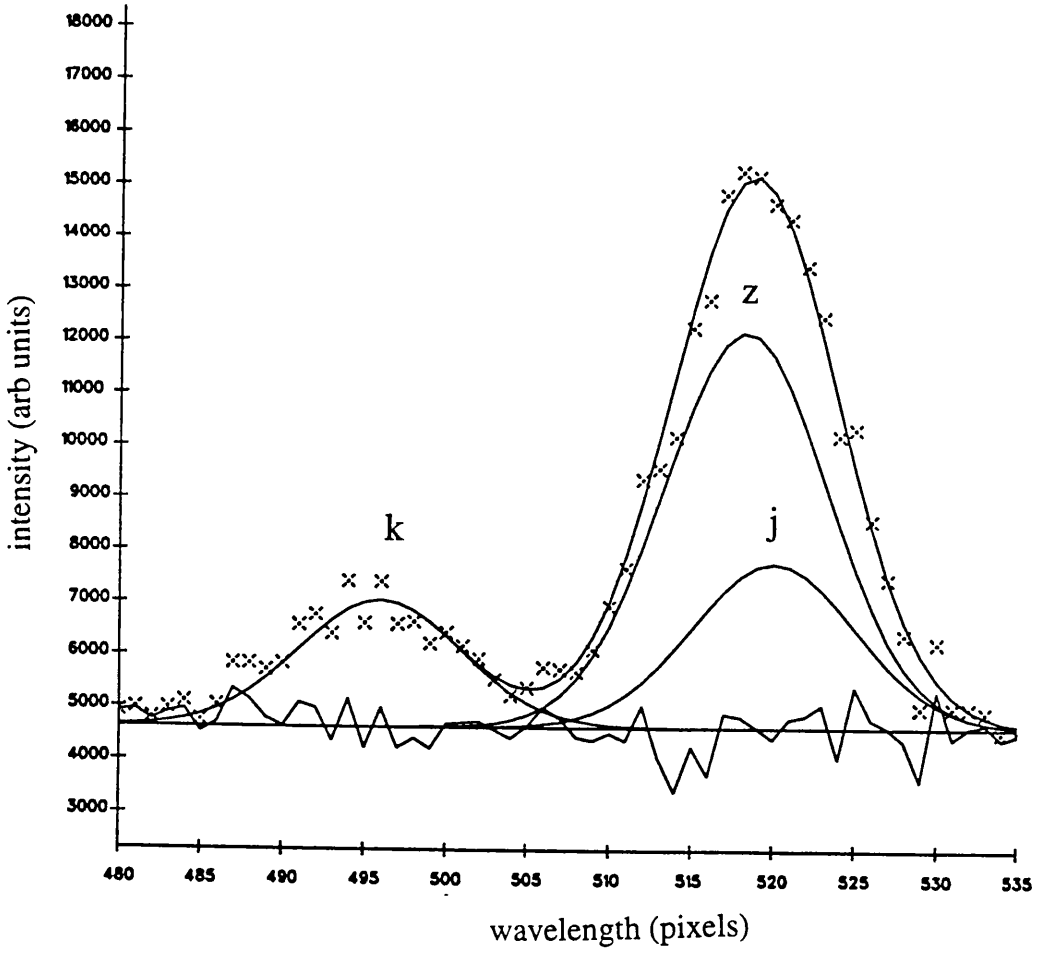

Figure 3.7: *Doppler measurements from fit to three lines, k, z and j. COMPASS-D # 14212.*

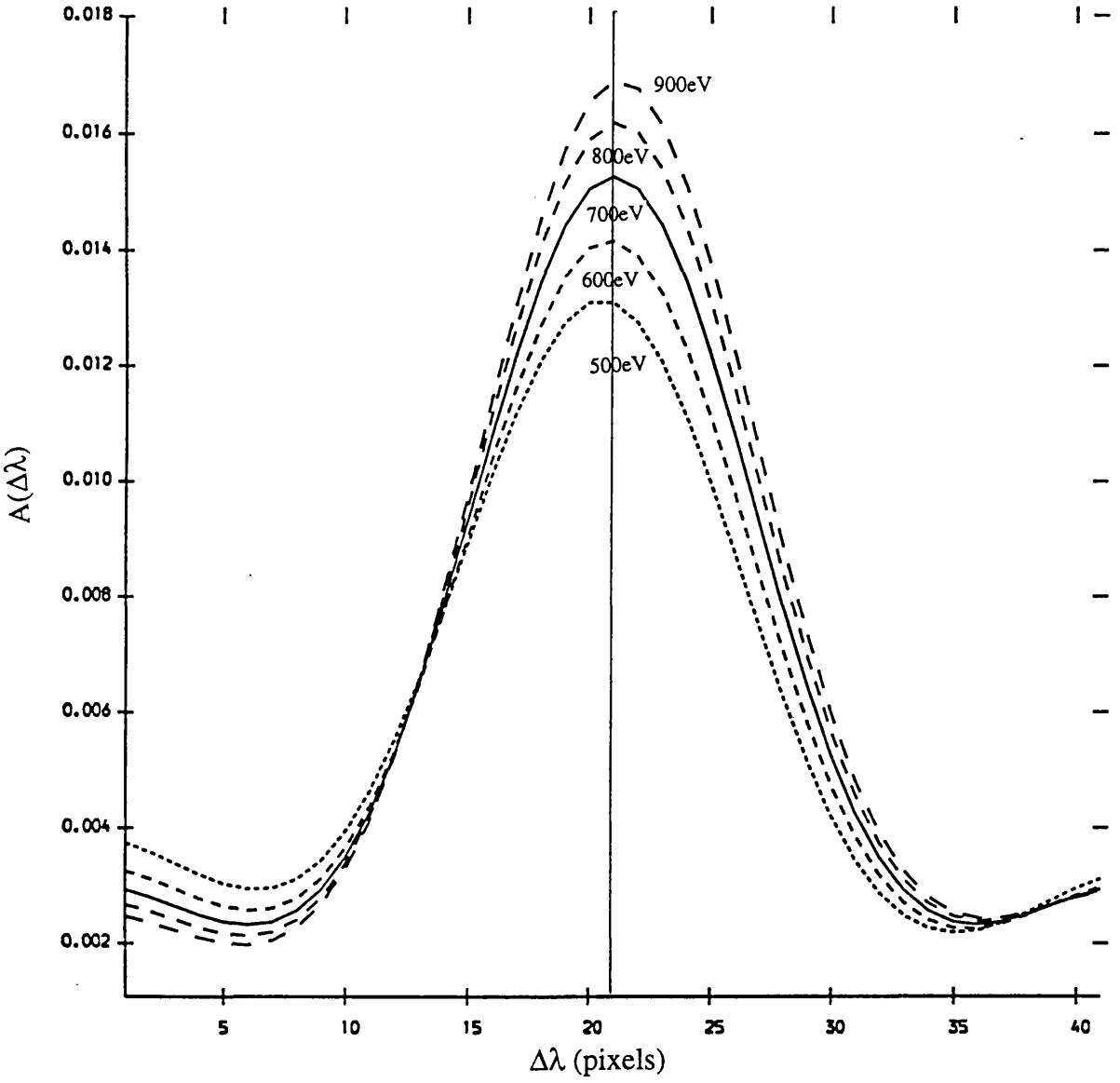

Figure 3.8: *Cross correlation of synthetic spectra. Spectra synthesised at* $T_e =$ $500eV$, $600eV$, $700eV$, $800eV$, *and* $900eV$ *cross correlated with a spectrum synthesised at* $T_e = 700eV$. *All spectra are at coronal equilibrium and have the same line widths. There is an apparent wavelength shift due to the change in the line intensities.*

Chapter 4

Heat and Particle Transport

Spectroscopic measurements of core electron and ion temperatures have been made on COMPASS-D. Electron temperatures are measured from the dielectronic satellite line to resonance line ratio of Cl XVI and are compared with measurements from Thomson Scattering. Ion temperatures are measured from Doppler broadening of spectral lines and are compared with the Artsimovich scaling law [Artsimovich 1972]. The time resolution of the spectrometer used for these measurements is also demonstrated.

An energy balance equation is set up for the electron and ion fluids and the simultaneous measurement of both temperatures leads to the derivation of some of the unknown parameters. The results are compared with neoclassical and anomalous heat transport coefficients.

The He- like G and R line ratios and the $\frac{q}{w}$ ratio have been measured and compared with coronal equilibrium predictions. The $\frac{q}{w}$ line intensity ratio is related to the $\frac{n_{Li}}{n_{He}}$ abundance ratio and changes to this line ratio can be interpreted in terms of the perpendicular diffusion coefficient $D_{\perp}$. The G ratio is dependent on the population mechanisms of the singlet and triplet states, and changes to the ratio occur due to enhancement of the triplet states due to additional recombination and inner shell ionisation when coronal conditions are not satisfied.

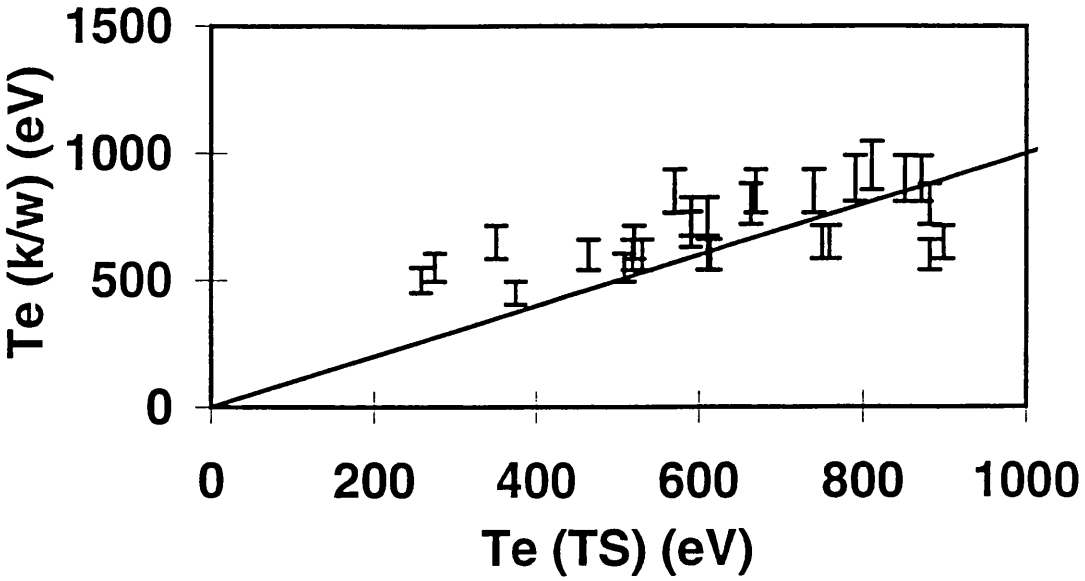

Figure 4.1: *Comparison of T_e derived from the $\frac{k}{w}$ ratio with Thomson Scattering measurements.*

4.1 Electron and Ion Temperature Measurement

Spectroscopic measurements have been made of both the central electron and ion temperatures. The electron temperature has been measured using the $\frac{k}{w}$ dielectronic satellite line to resonance line ratio. The temperature dependence of this ratio has been discussed in chapter 3 and is demonstrated in equation (3.12). As is shown in the equation, this line ratio is dependent only on the electron temperature and has no dependence on either the electron density or on the ionisation balance. This ratio is therefore preferred to the other temperature dependent ratios such as those involving the intercombination lines or the inner shell satellite lines which do have density and transport dependences.

The k line is excited purely by dielectronic recombination and has no contribution from inner shell excitation and at COMPASS-D ion temperatures is sufficiently resolved from other lines. The other dielectronic satellites such as d_{13} are in very close proximity to other lines.

The only disadvantage of this ratio is the sensitivity to non-Maxwellian electron distributions. Wherever possible the $\frac{k}{w}$ derived electron temperatures have been compared with Thomson scattering measurements. Figure 4.1 shows a comparison of the two temperature diagnostics. The main errors in the $\frac{k}{w}$ measurement are the quality of the fit and the errors associated with the vignetting function. The resonance line intensity has also been measured without taking

into account dielectronic satellites from $n \geq 4$ levels. The errors in the Thomson Scattering measurement are mainly associated with low photon statistics due to the small cross section for scattering. The errors do vary with plasma conditions and in general are in the order of 10%-20%. The large differences at the lower end of the temperature scale in Figure 4.1 are probably due to the absence of the $n \geq 4$ dielectronic satellite lines which would reduce the resonance line intensity and increase the ratio.

The ion temperature measurement has been discussed in detail in chapters 2 and 3. Ion temperatures have been measured over a wide range of plasma parameters and compared with Artsimovich's scaling law [Artsimovich 1972];

$$T_{i\ Artsimovich} = \frac{2.8 \times 10^{-6}}{A_i^{\frac{1}{2}}} \left(I_p B_\phi R^2 \bar{n}_e\right)^{\frac{1}{3}}\ eV, \tag{4.1}$$

where I_p is the plasma current in A, B_ϕ is the toroidal magnetic field in T, R is the major radius in m and $\bar{n}_e$ is the average electron density in m^{-3}. A_i is the ion mass in atomic units.

This scaling law assumes that the ions are heated by Coulomb collisions with the electrons and that heat losses are mainly through neoclassical collisional heat diffusion, with little contribution from particle diffusion and charge exchange losses. The scaling law is valid for $1.6 \leq \frac{T_e}{T_i} \leq 10$ as under these conditions (which are usually true for ohmically heated tokamaks) T_e can be eliminated from the ion temperature balance. The density dependence comes from the energy transmitted to the ions from Coulomb collisions with the electrons. The current, field and geometric dependences come from neoclassical heat conduction losses.

The measured ion temperatures are compared with the Artsimovich scaling in Figure 4.2. Also shown in the figure are the equivalent electron temperatures as measured from the $\frac{k}{w}$ ratio. The error bars in the ion temperature reflect the uncertainty in the instrument width and the fitting errors. The measured values are generally $40\% - 50\%$ lower than the predicted values. The best straight line fit through the points does show an increase with the Artsimovich parameters, however the scatter is large. The fitting errors have been reduced by summing together sufficient time slices for a reasonable fit. No account has been taken

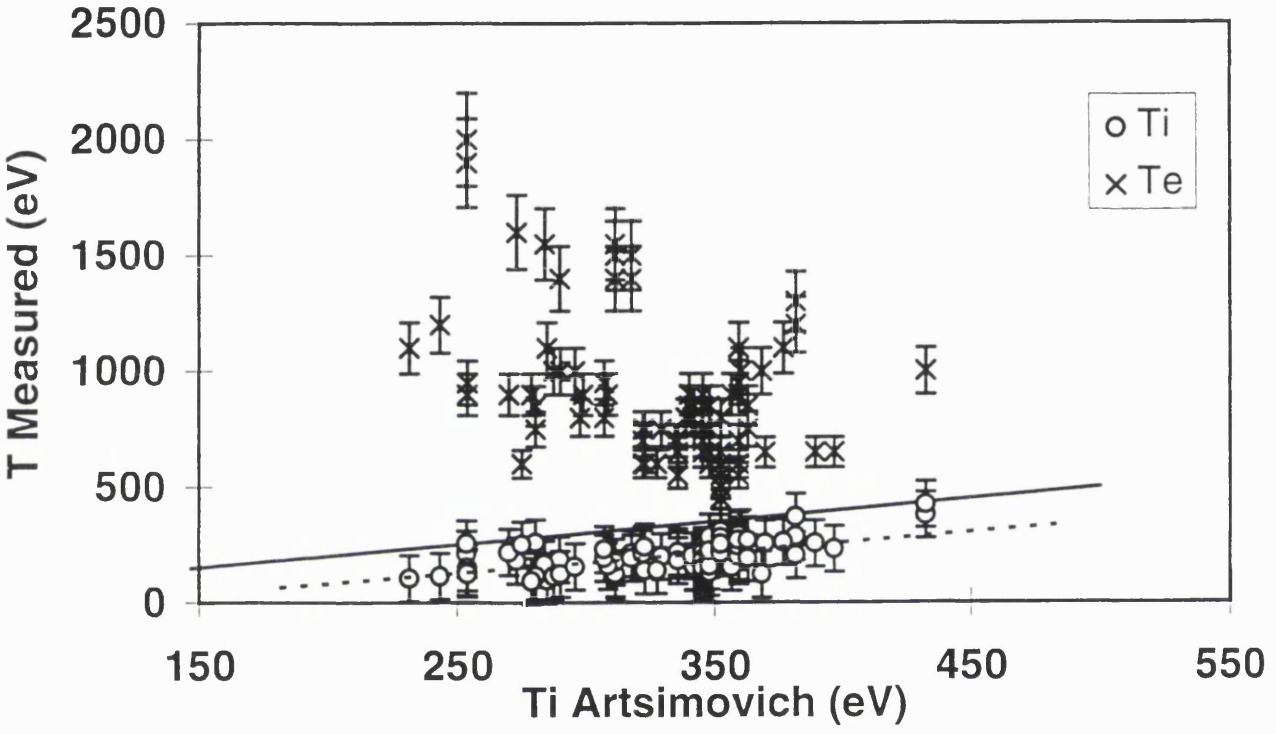

Figure 4.2: *Comparison of measured ion temperature with Artsimovich scaling. Also shown are the electron temperatures (measured using the $\frac{k}{w}$ ratio) for the same plasma pulses. The full line is the Artsimovich scaling, the dashed line is a best fit line to the measured values.*

of the effects of the vignetting function on the line width. The large differences between the measured ion and electron temperatures are discussed in section 4.2.

Improvement in the data could be achieved by reducing the fraction of the total line width due to instrumental effects. This can be done by increasing the dispersion by increasing the Rowland Circle diameter. For such an experiment, a different set of lines must be chosen as the vignetting function would not allow the whole He- like spectrum to be diffracted onto the detector, and would be at the cost of the other diagnostic information of the He- like spectrum. A singlet line would reduce uncertanties in the fit.

4.1.1 Ion Temperature Equilibration

The ion temperature is measured using Cl XVI ions. The equipartition time between two particle species A and B is [Spitzer 1962];

$$\tau_{eq} = \frac{(2\pi)^{\frac{1}{2}} 3\pi\epsilon_0^2 m_A m_B}{n_A Z_A^2 Z_B^2 e^4 \ln\Lambda} \left(\frac{kT_A}{m_A} + \frac{kT_B}{m_B}\right)^{\frac{3}{2}} \ s, \tag{4.2}$$

where m are the masses and T are the initial temperatures, all units are SI. This equation can be used for any two particle species. More convenient versions of such formulae are generally used with the constants evaluated and the units changed to the usually measured quantities. For the heating of an impurity ion from the background ions, the equipartition time can be expressed as;

$$\tau_{eq} = 2.34 \times 10^{17} \frac{A_i A_I}{Z_i^2 Z_I^2 n_i \ln\Lambda} \left(\frac{T_i}{A_i} + \frac{T_I}{A_I}\right)^{\frac{3}{2}} \ s, \tag{4.3}$$

where A are the ion masses in atomic units, the temperatures are in keV and the density in m^{-3}. The subscript I refers to the impurity ions and i to the bulk ions. $\ln\Lambda$ is the Coulomb logarithm, given by [Wesson 1987];

$$\ln\Lambda = 17.3 - \frac{1}{2}\ln\left(\frac{n_e}{10^{20}}\right) + \frac{3}{2}\ln T_i, \tag{4.4}$$

where n_e is in m^{-3} and T_i is in keV, it is typically ≈ 16 for the background ions in tokamak plasmas. Calculations involving collisions often only include large angle scattering ($> 90°$), however, due to the long range of the Coulomb force, small angle scattering is also very common, the Coulomb logarithm was introduced by Spitzer to take account of this [Spitzer 1962]. For Cl XVI ions at a temperature

of $200eV$ in a deuterium plasma with $n_e = 5 \times 10^{19} m^{-3}$, $\tau_{eq} \approx 5\mu s$. The electron - ion equipartition time is given by [Spitzer 1962];

$$\tau_{ie} = 0.99 \times 10^{19} \frac{A T_e^{\frac{3}{2}}}{n_i Z^2 \ln \Lambda} \; s, \tag{4.5}$$

where T_e is in keV. Under the same conditions as above with $T_e = 700eV$, $\tau_{ie} = 14.5ms$ which is large compared with the ion - impurity ion equipartition time. The Cl XVI temperature can therefore be considered to be equal to the bulk ion temperature.

4.1.2 Time Resolved Measurement

The CCD chip bins data in 2ms time slices. In general for the sake of good spectral fitting time slices must be added together to improve the photon statistics. At high density where the photon statistics are good, even for short time periods, it has not been necessary to sum time slices together. The time evolution of T_e and T_i from a COMPASS-D H-mode plasma are shown in Figure 4.3. The scatter of the points in the figure indicate the size of the error bars. For the ion temperature measurement, the error bars are larger before the commencement of the H-mode as the line intensity is weaker. The errors due to the fitting are therefore greater. More spectra are summed together in this period than during the H-mode in an attempt to reduce the size of the errors.

Most pulses require the addition of a number of time slices and many require the summation of the whole pulse ($\approx 300ms$). One solution to this problem would be to inject larger impurity concentrations into the plasma (for example argon gas puffing) for the measurement rather than rely on the intrinsic Cl level.

The figure also shows the H_α trace which is the usual H-mode indicator. Within the errors no change is seen in the ion temperature during the L-H transition.

4.2 Analysis of Temperature Measurement

4.2.1 Background Theory

The power balances of the electron and ion fluids are given by;

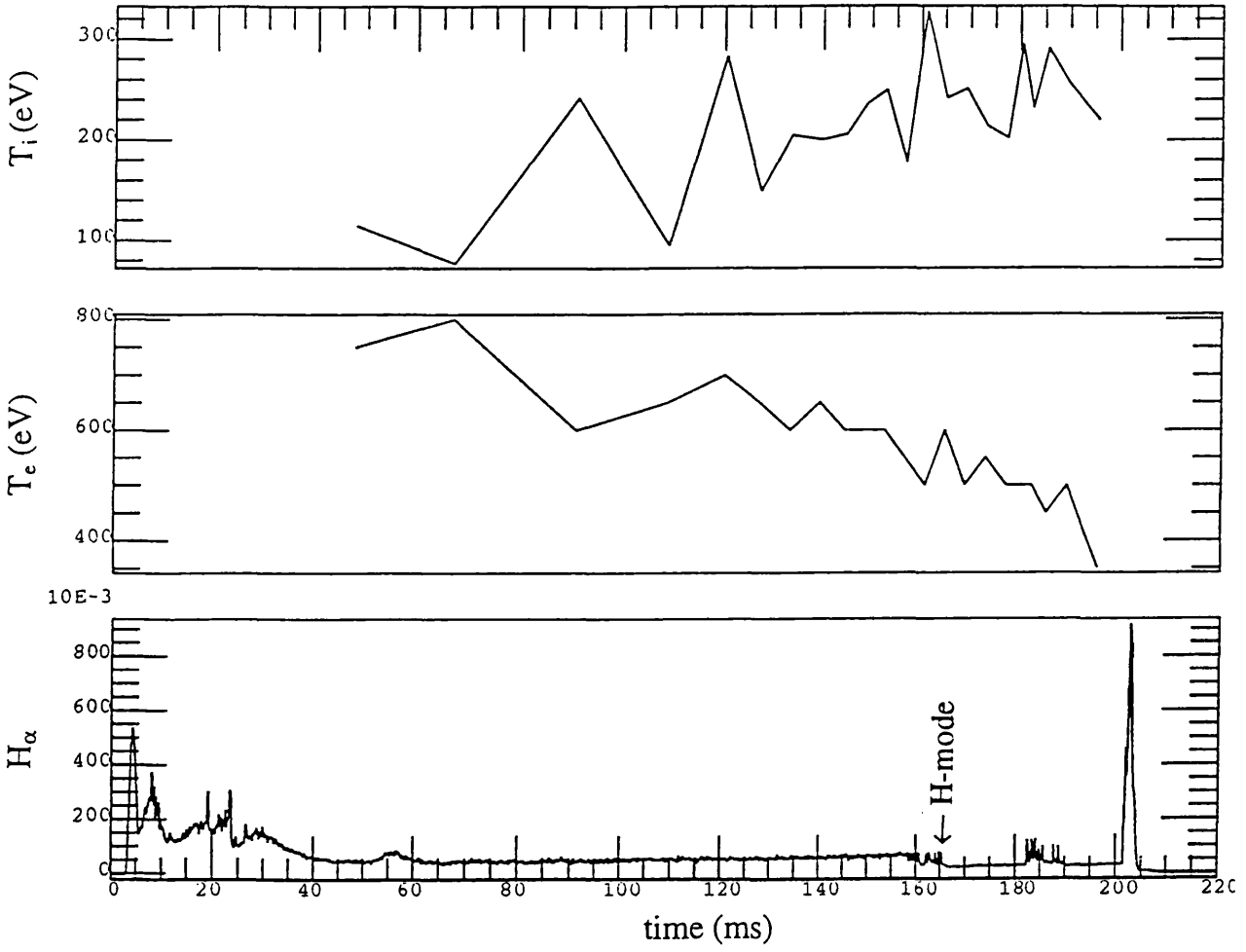

Figure 4.3: *Time resolved measurement of T_i and T_e during an H-mode plasma. The H_α trace is also shown to indicate the start of the H-mode. COMPASS-D shot #15070. The fluctuations in the measurements indicate the size of the error bars.*

Electron fluid:

$$\frac{\partial w_e}{\partial t} = \int P_{in} dV - \int \nabla.(n_e \chi_e \nabla T_e) dV - \frac{3}{2} \int \nabla.(T_e D_\perp \nabla n_e) dV - \int P_{ei} dV - \int P_{rad} dV; \tag{4.6}$$

Ion fluid:

$$\frac{\partial w_i}{\partial t} = \int P_{ei} dV - \int \nabla.(n_i \chi_i \nabla T_i) dV. \tag{4.7}$$

The various terms are as follows; P_{in} is the total heat input per unit volume to the electrons from ohmic and additional heating sources, P_{rad} is the power lost through radiation, P_{ei} is the power transmitted through Coulomb collisions from the electrons to the ions and w is the total kinetic energy. There is no direct ion heating on COMPASS-D. The terms including χ represent heat diffusion losses where χ is the heat diffusivity. The term including $D_\perp$ represents heat losses through particle diffusion. The ion fluid equation includes only those terms used in the Artsimovich scaling law. The particle diffusion and radiative loss terms as in the electron equation could also be included.

Heat losses occur both parallel and perpendicular to the magnetic field lines. Parallel losses are due to the guiding centre drift along the field lines whereas the perpendicular losses are due to collisions as the particles gyrate in Larmor orbits around the guiding centre. Radial particle diffusion and heat transport are therefore dependent on the particle collisionality. We shall consider only perpendicular diffusion because parallel diffusion, although faster, has no effect on closed magnetic surfaces. The classical electron heat diffusivity is given by [Book 1987];

$$\chi_e^{cl} = 4.7 \frac{k T_e \tau_e}{m_e} \frac{1}{\omega_{ce}^2 \tau_e^2} \; m^2 s^{-1}, \tag{4.8}$$

k is taken as $1.6 \times 10^{-19} J/eV$ if T_e is in eV. ω_{ce} is the electron gyro frequency, τ_e is the electron collision time in s. A more convenient form to use is

$$\chi_e^{cl} = 2.46 \times 10^{-24} \frac{n_e Z^2 \ln \Lambda}{B^2 T_e^{\frac{1}{2}}} \; m^2 s^{-1}, \tag{4.9}$$

where T_e is in keV, B is in T and n_e is in m^{-3}. The classical ion heat diffusion coefficient is [Book 1987]

$$\chi_i^{cl} = \frac{k T_i \tau_i}{m_i} \frac{1}{\omega_{ci}^2 \tau_i^2} \; m^2 s^{-1}, \tag{4.10}$$

and can be expressed more conveniently as

$$\chi_i^{cl} = 3.13 \times 10^{-23} \frac{A^{\frac{3}{2}} Z^2 n_i \ln \Lambda}{B^2 T_i^{\frac{1}{2}}} \; m^2 s^{-1}. \tag{4.11}$$

The term $\frac{1}{\omega_c^2 \tau^2}$ is a classical term which defines the "step length" for perpendicular diffusion as the Larmor radius [Stringer 1993]. The Larmor radius is defined as

$$r_L = \frac{v_\perp}{\omega_c} = \frac{m v_\perp}{ZeB}. \tag{4.12}$$

The "random walk" step length is equal to the Larmor radius in a uniform field. If there is a magnetic field gradient across the plasma, the step length will change and hence heat and particle diffusion losses are modified. The magnetic geometry of a tokamak is toroidal with a $\frac{1}{r}$ drop in the toroidal field along the major radius. The field is greater at the inside of the torus than at the outside. Particles gyrating around field lines experience a magnetic mirror effect due to the magnetic field gradient and become trapped in banana shaped orbits. There are three collisionality regimes. In low collisionality plasmas, many particles will be trapped in banana orbits and the perpendicular diffusion and heat conduction coefficients are enhanced, the step length being given by the width of the banana orbit rather than by the Larmor radius. This is called the banana regime. In the plateau regime, particles undergo a significant part of the banana orbit, but are then scattered. In this regime, diffusion is independent of collisionality. At still higher collisionalities, in collision dominated plasmas, diffusion is enhanced over the classical value by the toroidal curvature. This regime is called the Pfirsch - Schlüter regime. The three regimes are shown in Figure 4.4. The theory for these enhancements of particle diffusion is known as neoclassical theory and has been reviewed by [Hinton and Hazeltine 1976]. These three regimes exist for both particle diffusion and heat conduction.

Tokamak experiments show that for ion transport, neoclassical theory is a good approximation. The measured coefficients are within a factor 5 of the predicted values. However, experiments show that for electrons the transport coefficients are very much enhanced over the neoclassical values. Many models have been proposed to describe this anomalous transport. These models are generally based on plasma turbulence and instabilities, some are theoretical,

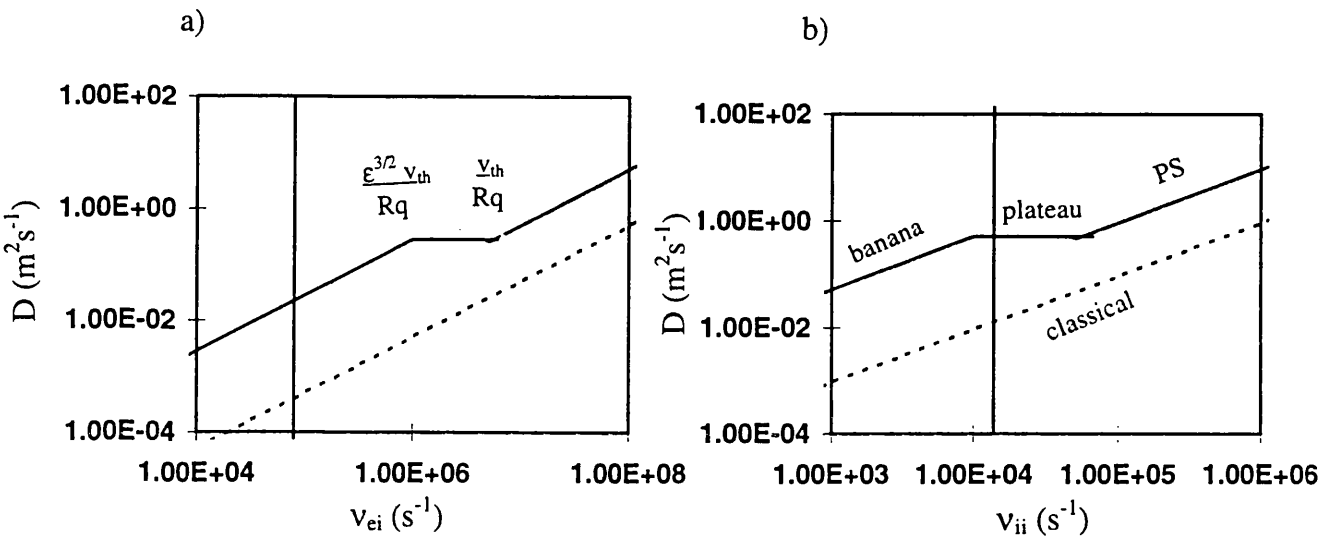

Figure 4.4: *Neoclassical diffusion a) electrons and b) ions. In both cases typical COMPASS-D conditions are marked* ($n_e = 5 \times 10^{19} m^{-3}$).

some semi - empirical. The general tests of such theories are their predictions of scaling laws and radial profiles.

One early example of anomalous diffusion is Bohm diffusion which predicts a confinement time scaling with good agreement with a number of different devices [Chen 1984]. The Bohm diffusion coefficient is given by

$$D_B = \frac{1}{16} \frac{kT_e}{eB}, \tag{4.13}$$

which predicts a diffusion coefficient four orders of magnitude larger than the classical diffusion coefficient for normal tokamak conditions.

The transport coefficients are improved in the H-mode, but not sufficiently to return to neoclassical values.

As shown in Figure 4.4 for typical COMPASS-D conditions, electrons are in the banana regime and ions are in the plateau regime. The neoclassical enhancement of the heat conductivities for the three regimes are given by [Gross 1984];

Banana regime:

$$\chi^b = \chi^{cl}\left(1 + \frac{q(a)^2}{\epsilon^{\frac{3}{2}}}\right); \tag{4.14}$$

Plateau regime:

$$\chi^p = \chi^b \text{ at the b-p boundary ;} \tag{4.15}$$

Pfirsch-Schlüter regime:

$$\chi^{PS} = \chi^{cl}\left(1 + q(a)^2\right); \tag{4.16}$$

where ϵ is the inverse aspect ratio, and q is the safety factor given by

$$q(r) = \frac{r}{R}\frac{B_\phi}{B_\theta}, \tag{4.17}$$

which is a measure of the number of times a field line goes toroidally around the torus for each poloidal circuit (see Figure 6.2).

One approximation of the anomalous heat conductivity is given as [Wesson 1987];

$$\chi_e^a = \frac{C10^{19}}{n_e}\, m^2 s^{-1}\ 1 < C < 5 \tag{4.18}$$

for the electrons, and

$$\chi_i^a = \alpha\chi^{nc}\ 1 < \alpha < 5 \tag{4.19}$$

for the ions, χ^{nc} is the neoclassical heat conductivity.

Some recent models of anomalous heat transport can be found in [Cordey et al 1995].

A heat diffusion confinement time can be calculated from the heat diffusivity equation. This is done by expressing the equation in cylindrical coordinates and then solving using a Bessel function in the same way as the diffusion equation in chapter 1. The conduction equation in cylindrical coordinates is;

$$\frac{1}{r}\frac{\partial}{\partial r}\left(r\frac{\partial T}{\partial r}\right) + \frac{3}{2\chi\tau}T = 0, \tag{4.20}$$

the solution is

$$\tau = \frac{a^2}{3.8\chi}. \tag{4.21}$$

The power transfer from the electrons to the ions is given by;

$$P_{ei} = \frac{3}{2}\frac{n_e k}{\tau_{ei}}(T_e - T_i), \tag{4.22}$$

where τ_{ei} is the heat transfer time given by;

$$\tau_{ei} = \frac{m_i}{2m_e}\tau_e, \tag{4.23}$$

and can be expressed more conveniently as in equation (4.5).

4.2.2 Data Analysis

We shall take two cases of the data shown in Figure 4.2; i) $n_e = 2 \times 10^{19} m^{-3}$, $T_e = 1500eV$ and $T_i = 150eV$; ii) $n_e = 1 \times 10^{20} m^{-3}$, $T_e = 700eV$ and $T_i = 300eV$. We shall also assume that for both cases $Z_{eff} = 2$ and that $B_\phi = 1.5T$. The heat conductivity times and heat transfer times for these cases are given in Table 4.1.

Table 4.1: *Classical, neoclassical and anomalous heat transfer times.*

times (ms)	case i)	case ii)
$n_e \times 10^{19} m^{-3}$	2	10
$T_e(eV)$	1500	700
$T_i(eV)$	150	300
q	6	3
$\tau_{\chi e}^{cl}$	28000	3900
$\tau_{\chi e}^{NC}$	126	69
$\tau_{\chi e}^{a}$	3	15
$\tau_{\chi i}^{cl}$	116	33
$\tau_{\chi i}^{NC}$	3	3
τ_{ei}	30	2

These values show very different behaviour for the two cases. Case i) has low density and high electron temperature. The electron heat transport is very anomalous and energy is lost preferentially through heat diffusion rather than through electron - ion collisions. Little energy is transferred to the ions and this is then lost quickly, hence the ion temperature remains low. Case ii) has high density and lower electron temperature. This case is closer to neoclassical predictions. Electrons in this case transfer more energy to the ions through

collisions, and lose less through heat diffusion. The ion temperature in this case is therefore higher. This behaviour seems to explain our measurements. Thus even though we do not have a direct measure of the heat transport coefficients, we can assume the above anomalous coefficients to explain the measured changes to T_e and T_i with the changing plasma conditions.

The total energy confinement time of the the plasma τ_E as measured by the diamagnetic loop is the average of the electron and ion energy confinement times. Our anomalous model value of $\tau^a_{\chi e}$ increases from $3ms$ to $15ms$ with the rising density whereas the neoclassical ion model $\tau^{NC}_{\chi i}$ hardly changes. Measurements of τ_E from the total stored energy vary from $\approx 5ms$ at low density L-modes to $\approx 15ms$ at high density L-modes and rising to $\approx 30ms$ in ELM free H-modes [Fielding et al 1994].

Since the ion heating is due to Coulomb collisions with the electrons, one would expect the ion temperature to increase during H-modes as the energy confinement time increases. Our measurements do not show any increase (See Figure 4.3).

We can calculate the expected ion temperature rise during the H-mode as a result of the increased confinement time. We can calculate the power transfer between the electrons and the ions, P_{ei}, from our T_e and T_i measurements and then model the ion temperature changes from

$$T_i = \frac{P_{ei}\tau_{EI}}{n_i}, \tag{4.24}$$

where τ_{EI} is the ion energy confinement time. If we assume that τ_{EI} increases from $0.5ms$ to $0.8ms$ from the L-mode to H-mode we obtain the results shown in Figure 4.5 which shows both the experimental temperatures and the value of T_i calculated from equation (4.24). Within the error bars shown ($\pm 50eV$ due to the the line fitting) we would not expect to see a change in the measured values of T_i across the L-H transition.

An alternative explanation for not seeing any increase in T_i is that our measurement is a measurement of the core ion temperature. The H-mode begins to form at the plasma edge and then the related effects of improved confinement move inwards on a time scale comparable with the energy confinement time [Groebner 1993]. For beam heated H-modes on DIII-D, the heat

a)

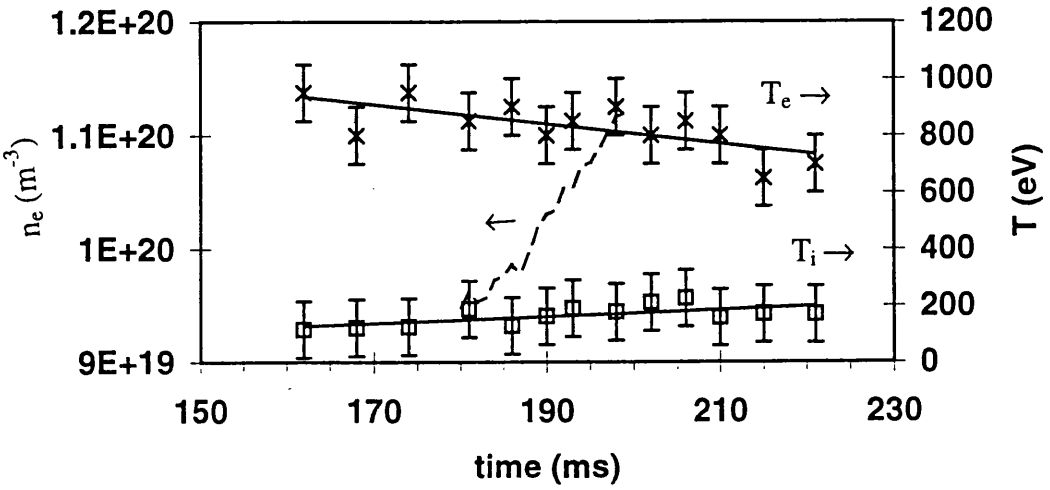

b)

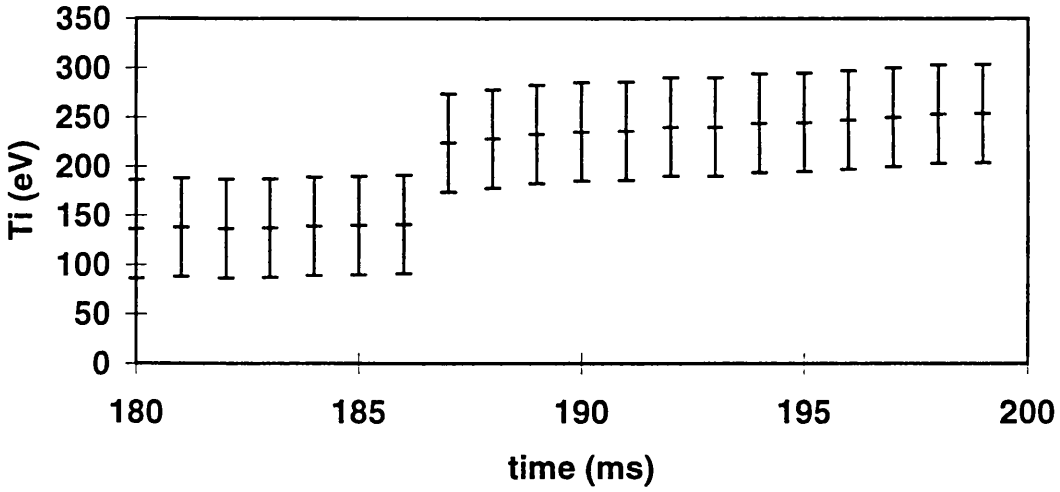

Figure 4.5: *a) Experimental measurements of T_e and T_i from shot #12570. The squares are T_i and the asterisks are T_e also shown is the density (dashed line). b) T_i calculated from equation (4.24) assuming an increase in τ_{EI} of* $0.5 - 0.8ms$ *at the L-H transition at* $186ms$.

transport coefficients in the plasma core begin to improve within 30 ms of the L-H transition and the improvement continues for 80 ms after the transition [Kurki-Suonio et al 1992]. On COMPASS-D, the energy confinement time during ELM free H-modes is increased to $\approx 30ms$ [Fielding et al 1994], and this would be the expected timescale for an increase in the ion temperature.

4.3 Line Ratios

Line ratios are measured by fitting the spectral lines with Voigt functions as described in chapters 2 and 3. The intensity ratio is then taken from the ratio of the line heights (strictly the ratio of the areas should be used, however the line widths are assumed to be the same). Three line ratios will be discussed here; the $\frac{q}{w}$ ratio, the G ratio and the R ratio. Measured values are compared with values predicted from coronal equilibrium calculations and any departures will be discussed. The theoretical model used is the same as used by [Coffey 1993] which includes all relevant processes for the 23 lowest $1snl$ states with $n < 6$ and $l < 3$. Dielectronic and radiative recombination are also included.

4.3.1 q/w Ratio

The q line is excited by inner shell excitation from the Li- like ground state. The intensity is proportional to the Li- like ground state density and is also dependent on the electron temperature through the excitation rate. The w line is excited mainly by electron impact excitation of the He- like ground state, the intensity is therefore proportional to the He- like ground state and also has an electron temperature dependence. The $\frac{q}{w}$ ratio is given by equation(3.17), and is sensitive to the electron temperature through the excitation rates and to the ionisation equilibrium through the ratio of the two ground state densities. The measured values of the $\frac{q}{w}$ ratio from a large variety of plasma conditions are shown in Figure 4.6 and are compared with the coronal predictions calculated for $n_e = 5 \times 10^{19} m^{-3}$. The experimental points lie on or above the coronal curve showing that for these plasmas the coronal values are a lower limit to the $\frac{q}{w}$ ratio. The simplest explanation would be that the Li- like density is enhanced

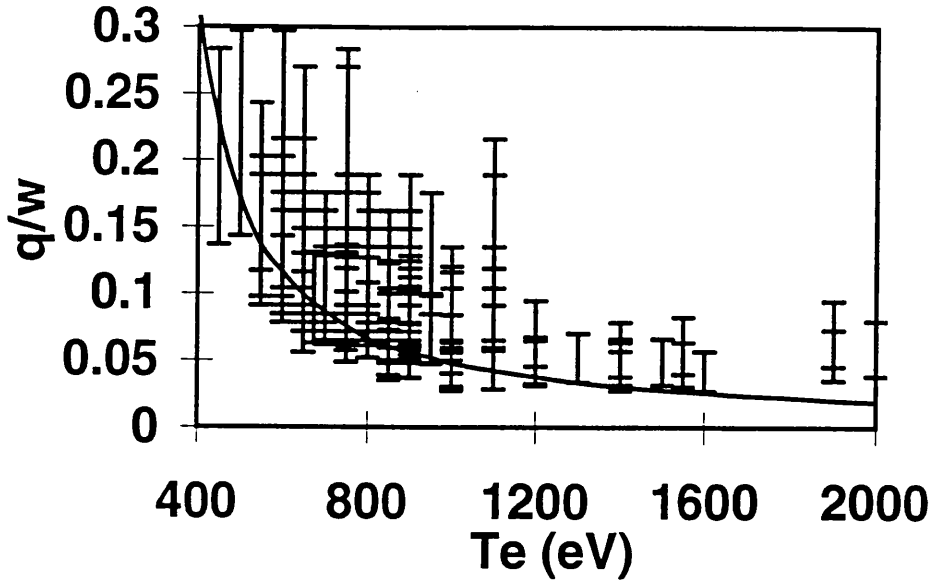

Figure 4.6: *Experimental $\frac{q}{w}$ ratio plotted against T_e (from the $\frac{k}{w}$ ratio) compared with coronal equilibrium predictions for $n_e = 5 \times 10^{19} m^{-3}$.*

over that predicted by the coronal model due to inward diffusion of the Li- like ions towards the plasma core. These effects can be modelled using a zeroth order transport equation (see equation (1.21)) in which the impurity confinement time can be varied to give different values for the $\frac{n_{Li}}{n_{He}}$ ratio and hence the $\frac{q}{w}$ ratio. The diffusion coefficient $D_\perp$ can then be found from τ_{imp} from equation (1.26).

Using such a model, the low density results $n_e = 2 \times 10^{19} m^{-3}$ have been modelled as is shown in Figure 4.7 [O Mullane 1994]. The $\frac{q}{w}$ ratio is modelled for coronal equilibrium (infinite confinement time) and for a range of impurity confinement times. It is found that our data at these densities lie between coronal equilibrium and $\tau_{imp} = 30ms$. This is equivalent to $D_\perp \leq 0.2 m^2 s^{-1}$. Modelling of laser ablations with the STRAHL transport code gives $D_\perp = 0.1 m^2 s^{-1}$ [Peacock et al 1995]. At higher densities, the $\frac{q}{w}$ ratio becomes less sensitive to transport effects. The enhancement of the ratio at these higher density and lower temperature plasmas implies an enhancement of the Li- like ground state population relative to the He- like ground state population under these conditions.

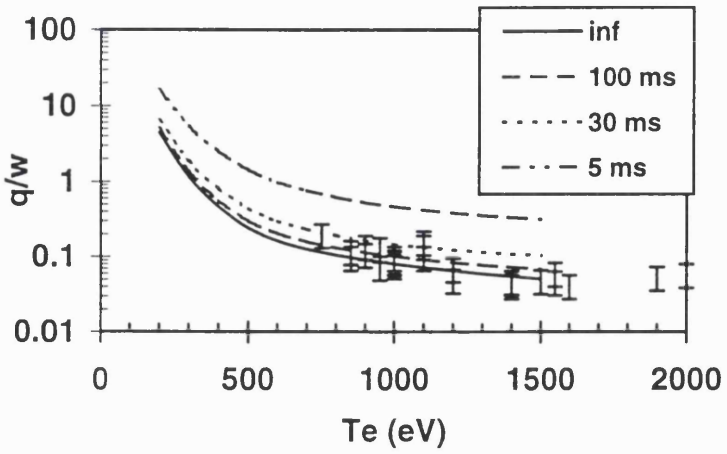

Figure 4.7: *Experimental $\frac{q}{w}$ ratio plotted against T_e (from the $\frac{k}{w}$ ratio) compared with coronal equilibrium predictions for $n_e = 2 \times 10^{19} m^{-3}$. The $\frac{q}{w}$ has been calculated for various impurity confinement times, coronal equilibrium is considered to have infinite confinement time.*

4.3.2 G and R Ratios

The G and R ratios are based entirely on He- like lines excited from the He-like ground state with additional contributions from recombination from the H- like state and inner shell ionisation from the Li- like ground state. The G ratio ($G = \frac{x+y+z}{w}$ see equation (3.9)) is electron temperature sensitive through the excitation rates. The R ratio ($R = \frac{z}{x+y}$ see equation (3.8)) is temperature sensitive through the excitation rates, but is also electron density sensitive as the $^3S_1$ metastable state is collisionally coupled to the ^3P levels.

The ratios can be calculated for coronal conditions taking into account the expected contributions from recombination and inner shell ionisation, however as the plasma departs from coronal conditions, ionisation or recombination can dominate and the G and R ratios change accordingly. As a guide to the ionisation state of the plasma, the values of the G ratio shown in Table 4.2 are found to be useful [Pradhan 1985]. Recombination predominantly fills the triplet levels rather than the singlet levels and therefore the G ratio is increased in cooling plasmas. In coronal equilibrium, recombination accounts for about half the contribution of the triplet levels and therefore in ionising plasmas where recom-

Table 4.2: *A simple guide to the impurity ionisation state based on changes of the G ratio from [Pradhan 1985]. T_m is the temperature of maximum abundance in coronal equilibrium ($\approx 800eV$ for Cl XVI) G_0 is the lower limit of the G ratio from electron impact excitation and ionisation.*

ionising plasma	$G_0 < G < 0.7$	$T_e > T_m$
coronal equilibrium	$0.7 < G < 1.5$	$T_e \approx T_m$
recombining plasma	$G > 1.5$	$T_e < T_m$

bination is reduced, the G ratio is also reduced.

Inner shell ionisation from the Li- like ground state, $1s^2 2s\ ^2S_{\frac{1}{2}}$, leaves the ion in an excited state $1s2s$ and three quarters of the population goes into the $^3S_1$ level [Phillips et al 1994]. At tokamak densities a large fraction of the Li-like ions are in the $1s^2 2p\ ^2P_{\frac{1}{2},\frac{3}{2}}$ states due to the high collisional excitation rate of the $2p$ level and its low radiative decay rate, [McWhirter 1981]; inner shell ionisation from these levels will populate the $1s2p\ ^3P_{2,1,0}$ levels. However, the total contribution to the z line due to inner shell ionisation is small ($< 4\%$), it is less for the other lines, [Phillips et al 1994, Bitter et al 1985].

Measurements of the C V triplet lines $1s2s\ ^3S_1 - 1s2p\ ^3P_{2,1,0}$ on the TJ-I tokamak [McCarthy and Zurro 1995] have shown that the intensity ratio of

$$\frac{I\ 1s2s\ ^3S_1 - 1s2p\ ^3P_2}{I\ 1s2s\ ^3S_1 - 1s2p\ ^3P_{1,0}}, \tag{4.25}$$

is greater than expected across most of the plasma radius. Modelling of these results shows that charge exchange recombination between neutral particles and C VI ions could be responsible for the enhanced intensity ratio. Measurement of this line ratio is even proposed as a measure of the neutral density in the plasma. This does imply that the extra population is going into the $1s2p\ ^3P_2$ level and if applicable to our case would imply an enhanced G ratio and reduced R ratio.

The measured G ratios for a range of plasma conditions are shown in Figure 4.8 and are compared with coronal predictions. At the higher temperatures, the measured values agree very well with the predictions, however at the lower temperatures the measured G ratio is generally higher than the coronal prediction

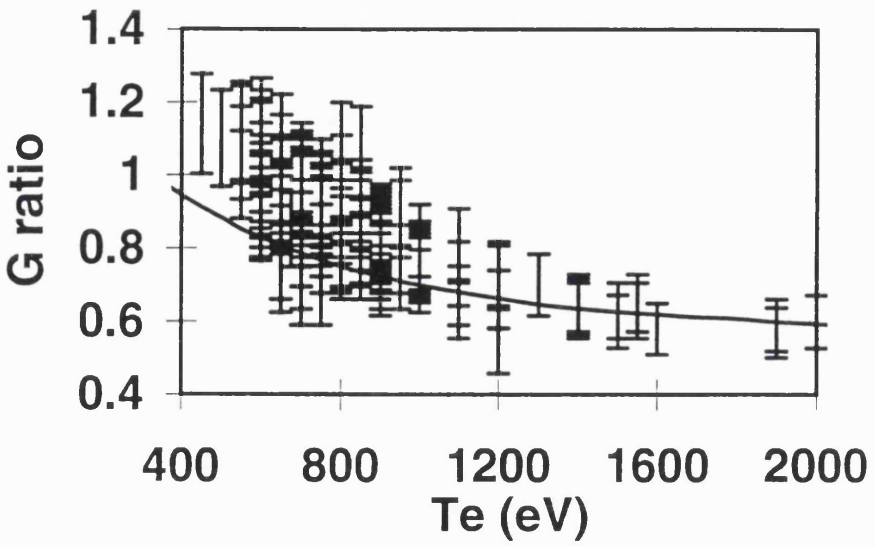

Figure 4.8: *Experimental G ratio plotted against T_e (from the $\frac{k}{w}$ ratio) compared with coronal equilibrium predictions.*

which would imply additional recombination or inner shell ionisation at these temperatures. The measured R ratios for the same discharges plotted against electron temperature are shown in Figure 4.9. The densities used are below or just bordering the density sensitive region for Cl XVI. The measured results are $\approx 20\%$ below the coronal prediction with a region of greatest scatter in the data at $\approx 600eV$. Measurements of the R ratio for Cl XVI below the coronal predictions are also reported by [Coffey 1993]. Most of the points in the region of greater scatter are in the same density region, $n_e = 1 \times 10^{20} m^{-3}$. The good agreement for the G ratio implies that the vignetting function and the line blending have been taken care of adequately and are unlikely to be the reason for the low R ratios. The high temperature G ratio results show that the ratio of the singlet to triplet populations are as predicted, but the R ratio shows that there is a redistribution of the population within the triplet states and that the ^3P states are populated preferentially to the ^3S state.

Measurements of the G and R ratios of He- like Cl and S on the ALCATOR-C tokamak are close to the predicted coronal values [Källne et al 1983]. However there is a large variation in the $\frac{x}{y}$ line ratio. The ratio is not predicted to change with n_e or T_e. The observations of changes in the $\frac{x}{y}$ ratio are not correlated

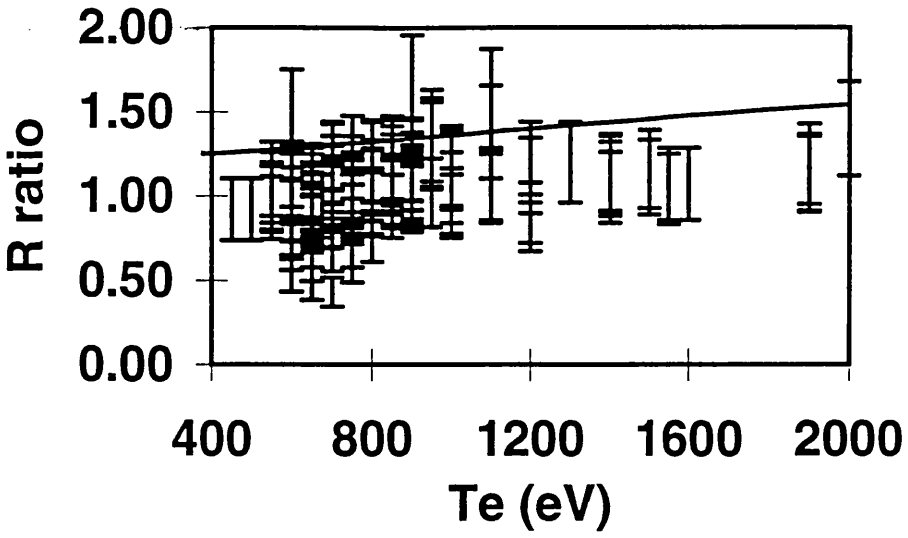

Figure 4.9: *Experimental R ratio plotted against T_e (from the $\frac{k}{w}$ ratio) compared with coronal equilibrium predictions. The densities are below the density sensitive limit for Cl XVI.*

with changes in any of the measured plasma parameters. There is speculation on a number of additional population mechanisms for the ^3P states, but none fit the experimental results. The $\frac{x}{y}$ ratio measured on COMPASS-D is shown in Figure 4.10 and is compared with the coronal values. The coronal value shows no change with temperature, however the measured values show a greater scatter at lower temperatures with a slight tendency towards an enhanced y line. The region of this scatter is approximately the same temperature region as the region of greatest scatter in the R ratio.

Increases in the G ratio (above coronal predictions) of TiXXI below 1200eV have been observed [Bitter et al 1985]. There is a correlation between the departure from coronal conditions and the density ratio of $\frac{n_{Li}}{n_{He}}$ which implies that excitation / ionisation from the Li- like ground state is responsible for the enhancement, but a likely mechanism cannot be found.

4.4 Discussion

The differences between the measured ion and electron temperatures have been modelled with a simple anomalous transport model. Neoclassical transport is found to be insufficient to model the temperature data. However, in order to make a serious attempt at testing more detailed anomalous transport models

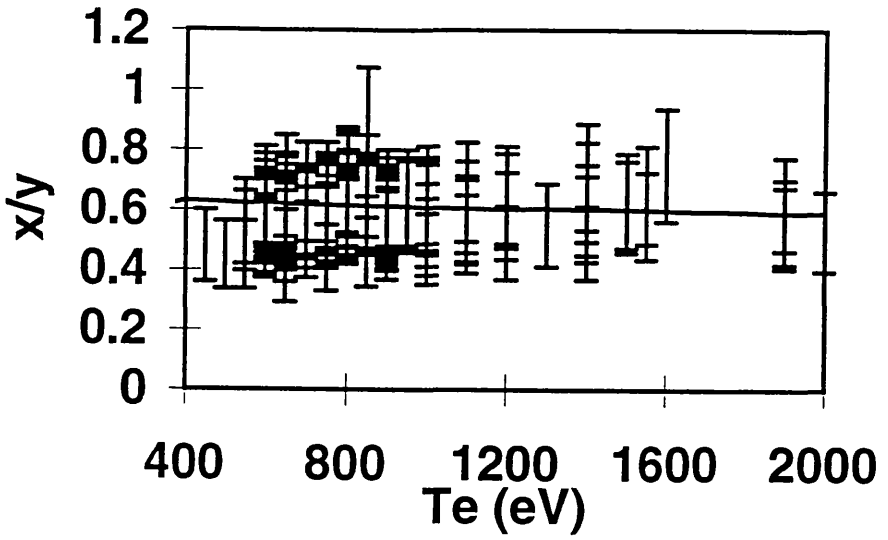

Figure 4.10: *Experimental $\frac{x}{y}$ ratio plotted against T_e (from the $\frac{k}{w}$ ratio) compared with coronal equilibrium predictions.*

temperature and density profiles are required which are not available here. No attempt has therefore be made to investigate heat transport any further.

Our line ratio results show good agreement with coronal predictions (except for the R ratio which is a little low) at electron temperatures above $\approx 800eV$. These results have mostly been obtained from plasmas with $n_e \leq 5 \times 10^{19} m^{-3}$ and as shown in Figure 4.7 are close to coronal conditions.

At lower temperatures and higher electron densities the measured ratios depart from coronal conditions. Many of these results are obtained from high density H-mode plasmas during which T_e is slowly decreasing (Figure 4.3) and n_e is increasing. It is thought unlikely that recombination is responsible for the increased G ratio as the electron temperature in these pulses is not high enough to burn through to Cl XVII. The enhanced $\frac{q}{w}$ ratio in these conditions (Figure 4.6) does imply that the Li- like density is increased over the expected coronal values and that some form of inner shell ionisation or excitation is populating the triplet states as suggested by [Bitter et al 1985]. If this population mechanism preferentially populates the ^3P states rather than the ^3S states it would also help to explain our R ratio and $\frac{z}{y}$ ratio results.

Chapter 5

Intensity Measurements

The various types of plasma radiation have been described in chapter 1. A typical spectrum comprises both line and continuum radiation. The continuum consists of both bremsstrahlung and radiative recombination. The bremsstrahlung intensity is related to the effective charge of the plasma, Z_{eff}, but the contribution of radiative recombination must be taken into account when using the continuum intensity to derive Z_{eff}.

Absolute intensity measurements of spectral lines provide an alternative method for finding the total impurity content and Z_{eff};

$$Z_{eff} = \frac{1}{n_e} \sum_I n_I Z_I^2, \tag{5.1}$$

where the summation is over the total ion content of the plasma, n_I is the density of ion species I and Z_I is the ion charge.

The x-ray continuum on the short wavelength side of the Cl XVI w line has been measured in various plasma conditions. The measured continuum intensity has been modelled taking account of both bremsstrahlung and radiative recombination. An impurity mixture containing the most abundant impurities found in COMPASS-D has been to model the continuum levels.

Measurements of chlorine concentrations on COMPASS-D from different conditions are also presented. The chlorine line intensity is modelled using a coronal model. An analysis of differences between the time evolution of the Cl XVI line intensity and the electron density is used to speculate on impurity accumulation at the plasma core during H-modes.

5.1 Continuum Measurements

Measurements of the continuum made in the visible are generally free from radiative recombination [Kadota et al 1980] and hence that is the preferred wavelength region for Z_{eff} measurement. In the soft x-ray region, radiative recombination must be taken into account. An absolute intensity factor of 5 to 100 times larger than that expected from pure hydrogen bremsstrahlung, due mainly to the presence of oxygen and metals, is often measured [Von Goeler et al 1975]. In particular one can say [DeMichelis and Mattioli 1981];

$$I_{ff} + I_{fb} = \psi I_{ff}, \tag{5.2}$$

where I_{ff} is the bremsstrahlung intensity and I_{fb} is the radiative recombination intensity. ψ is an enhancement factor. The pure hydrogen bremsstrahlung intensity can be calculated from measured values of n_e and T_e and this can then be compared with measurements of the continuum. It is found that the gradients of the calculated and measured continuum spectra (as a function of energy) are the same, but the measured intensity is enhanced over the calculated intensity. The enhancement factor can be modelled if the impurity distribution is known. This approach has been used by [Von Goeler et al 1975] and by [Silver et al 1982].

The approach used here is to model the two contributions to the continuum separately and to compare the sum of the contributions with the measured values. We shall begin with the bremsstrahlung contribution. The method used is similar to that of [Kadota et al 1980], also described by [Foord et al 1982].

i) The number of photons emitted per wavelength interval per second per cm^{-3} due to bremsstrahlung is given by;

$$\frac{d\epsilon}{d\lambda} = \frac{\alpha}{\lambda} g_{ff} Z_{eff} \frac{n_e^2}{T_e^{\frac{1}{2}}} e^{\frac{-E}{T_e}} \; photons \; cm^{-3} \; s^{-1} \; \mathring{A}^{-1}, \tag{5.3}$$

where n_e is in cm^{-3}, E (photon energy) and T_e are in eV, and λ is in $\mathring{A}$, g_{ff} is the free-free Gaunt factor and α is a constant given by [Stratton 1965];

$$\alpha = \frac{3.3 \times 10^{-18} \chi_H^{\frac{1}{2}}}{\lambda} \; eV \; cm^3 = 9.5 \times 10^{-14} \; photons \; cm^3, \tag{5.4}$$

χ_H is the ionisation potential of hydrogen (13.6 eV), 1 $photon = 2793eV$ for the region around the Cl XVI w line.

Our measurement is a line integral measurement along a tangential chord;

$$B = \frac{2}{4\pi}\int_{a_1}^{a_2} \frac{d\epsilon}{d\lambda} dx \ photons \ cm^{-2}s^{-1} \ \mathring{A}^{-1} \ sr^{-1}, \tag{5.5}$$

a_1 is towards the plasma centre and a_2 is towards the plasma edge. For SNX plasmas the chord length observed by the curved crystal spectrometer $\approx 92cm$. A schematic of the spectrometer line of sight is shown in Figure 5.1.

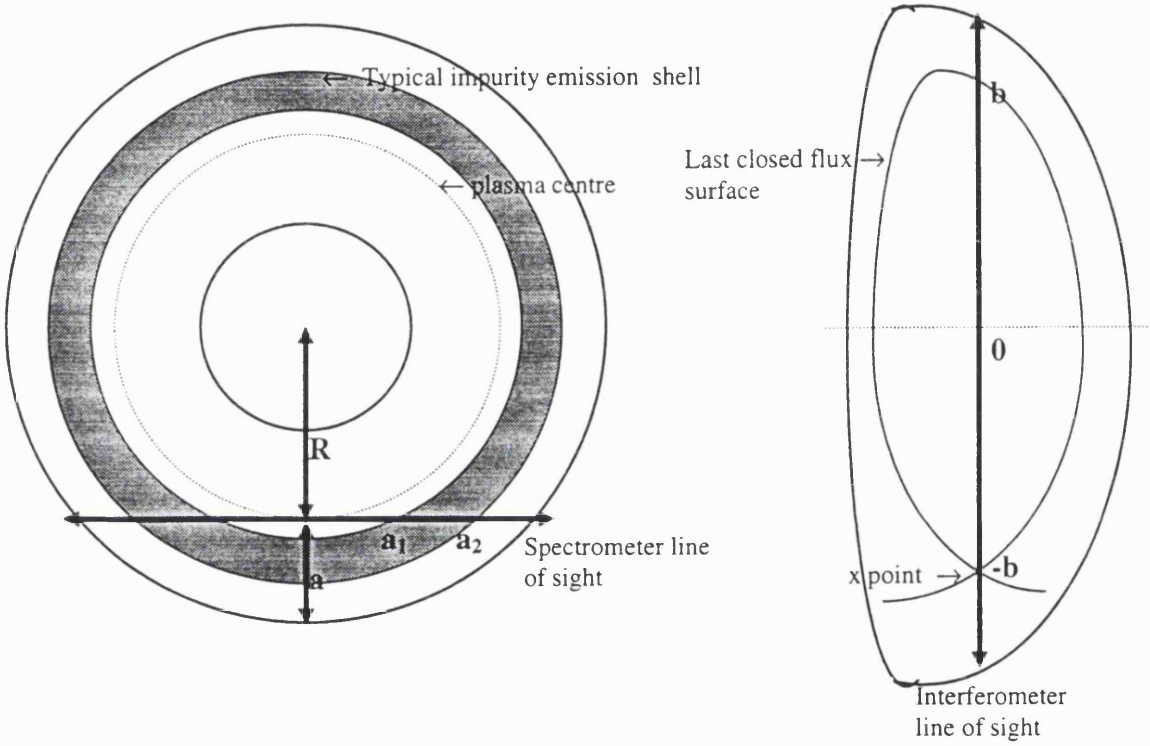

Figure 5.1: *Toroidal and poloidal cross sections of the tokamak showing the curved crystal spectrometer and interferometer lines of sight. A typical impurity emission shell (not Cl XVI) is shown in the toroidal cross section and the last closed flux surface of a single null x-point (SNX) plasma is shown in the poloidal cross section. a_1 and a_2 represent the limits of the integral in equation 5.5, a is the minor radius and R is the major radius.*

Substituting (5.3) into (5.5) gives

$$B = \frac{2}{4\pi}\frac{9.5\times10^{-14}}{\lambda}\overline{Z_{eff}}\int_{a_1}^{a_2} g_{ff}(x)\frac{n_e(x)^2}{T_e(x)^{\frac{1}{2}}}e^{\frac{-E}{T_e(x)}}dx \ photons \ \ cm^{-2}s^{-1} \ \mathring{A}^{-1} \ sr^{-1}, \tag{5.6}$$

where $\overline{Z_{eff}}$ is now the line averaged $Z_{eff}(x)$. The Gaunt factor $g_{ff}(x)$ is taken as 1 for these energies [Karzas and Latter 1961]. This a good approximation to within $\approx 20\%$.

Substituting profiles for n_e and T_e as given in chapter 1 (equations (1.3) and (1.4)), we obtain;

$$B = \frac{2}{4\pi}\frac{9.5\times10^{-14}}{\lambda}\overline{Z_{eff}}\frac{n_e(0)^2}{T_e(0)^{\frac{1}{2}}}\chi \ photons\ cm^{-2}s^{-1}\ \mathring{A}^{-1}\ sr^{-1}, \tag{5.7}$$

where χ is a profile function given by

$$\chi = \int_{a_1}^{a_2}\frac{\left[1-\frac{x^2}{a^2}\right]^2}{\left[1-\frac{x^2}{a^2}\right]}exp\left(\frac{-E}{T_e(0)\left[1-\frac{x^2}{a^2}\right]^2}\right)dx. \tag{5.8}$$

This is calculated numerically using Simpson's rule.

The density measurement is a line of sight average measurement, the central density $n_e(0)$ is assumed to be given by

$$n_e(0) = \frac{3}{4b}\int_{-b}^{b} n_e(y)dy\ cm^{-3}, \tag{5.9}$$

where $b = 24cm$ is the interferometer path length (equation (5.9) is obtained from the density profile given by equation (1.3)). The interferometer line of sight is shown in Figure 5.1. Substituting (5.9) into (5.7)we obtain;

$$B = \frac{2}{4\pi}\frac{9.5\times10^{-14}}{\lambda}\frac{9}{16b^2}\overline{Z_{eff}}\frac{\left[\int_{-b}^{b} n_e(y)dy\right]^2}{T_e(0)^{\frac{1}{2}}}\chi \ photons\ \ cm^{-2}s^{-1}\ \mathring{A}^{-1}\ sr^{-1}. \tag{5.10}$$

This is multiplied by the spectral width of the wavelength region measured to give the absolute intensity expected from bremsstrahlung alone.

ii) The volume emissivity per wavelength per second per cm^{-3} interval for radiative recombination is given by

$$\frac{d\epsilon}{d\lambda} = \frac{\alpha}{\lambda}g_{fb}\beta\frac{n_e^2}{T_e^{\frac{3}{2}}}e^{\frac{\chi_I-E}{T_e}}\ photons\ cm^{-3}\ s^{-1}\ \mathring{A}^{-1}. \tag{5.11}$$

g_{fb} is the free-bound Gaunt factor (this is again taken as 1), χ_I is the ionisation potential of each impurity ion species and β is the enhancement factor for radiative recombination, given by [Von Goeler et al 1975, Silver et al 1982]

$$\beta = \frac{n_I}{n_e}Z_s^I\frac{\xi}{n^3}\chi_I, \tag{5.12}$$

which represents recombination to the lowest n level available. Recombination to higher n levels have been ignored in the present analysis. ξ is the number of vacancies in the level n before recombination has taken place. Z_s^I is the ionic charge, n_I is the density of the recombining ion, the ionisation potential χ_I refers to the recombined ion. Following the procedure outlined above for bremsstrahlung, we obtain for radiative recombination;

$$B = \frac{2}{4\pi}\frac{9.5\times10^{-14}}{\lambda}\frac{9}{16b^2}\overline{\beta}\frac{\left[\int_{-b}^{b} n_e y dy\right]^2}{T_e(0)^{\frac{3}{2}}}\chi \; photons \;\; cm^{-2}s^{-1}\,\mathring{A}^{-1}\,sr^{-1}, \quad (5.13)$$

where the profile function χ is now given by

$$\chi = \int_{a_1}^{a_2} \frac{\left[1-\frac{x^2}{a^2}\right]^2}{\left[1-\frac{x^2}{a^2}\right]^3} exp\left(\frac{\chi_I - E}{T_e(0)\left[1-\frac{x^2}{a^2}\right]^2}\right) dx. \quad (5.14)$$

This is multiplied by the spectral width of the measurement to give the radiative recombination intensity. These intensity calculations are carried out by performing the integration for each impurity species separately taking into account the impurity concentration and the radial position of the emitting shells. The radial positions of the charge states have been estimated from the STRAHL code with typical COMPASS-D conditions.

Measurements are presented from two types of plasma conditions; high density H-mode pulses and discharges with Ne gas puffing. Figure 5.2 shows the time history of the continuum intensity measured during an H-mode discharge. The continuum is measured over a 31 pixel ($5.3m\mathring{A}$) region on the short wavelength side of the w line. This region is free from line radiation whilst much of the long wavelength side of the w line is contaminated with satellite lines from various ionisation stages.

We can model this both before and after the onset of the H-mode. We use the impurity concentrations as given in Table 5.1, He- like, H- like and fully stripped ions only are considered. The impurities used are the most abundant impurities found in COMPASS-D: the concentrations have been adjusted to fit the measured continuum values. The same values of radial position (obtained from the STRAHL code) and concentration are used for both L and H- modes: the change in the continuum value is then a measure of the change in density only. T_e is assumed to remain constant ($\approx 600eV$). In reality there is a small

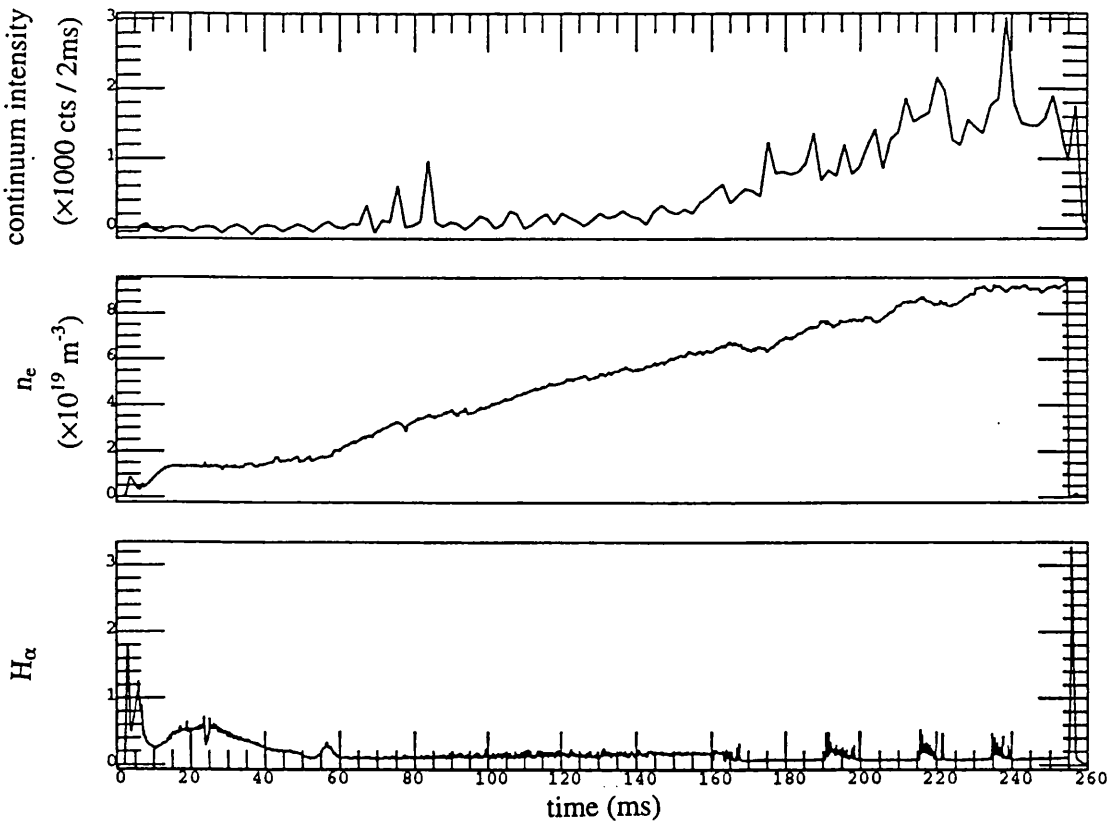

Figure 5.2: *Time history of continuum during H-mode, also shown are the density and H_α traces. An ELM free H-mode forms at 167 ms. #13460.*

decrease in T_e which would imply a small increase in Z_{eff}, see section 5.2.1. Z_{eff} with these values is 1.3. The model for these two cases is shown in Figure 5.3. It is clear that in this case bremsstrahlung dominates over radiative recombination. However if we were to add in some heavier impurities into the model, for example metals, we would expect the radiative recombination contribution to increase.

Figure 5.4 shows the increase in the measured continuum during a plasma discharge with neon gas puffing. There is a small density increase during the gas puff, but we have also added 3 % Ne into the plasma which increases the model Z_{eff} to 4.3. The model for this discharge, both before and after the gas puff is shown in Figure 5.5. The temperature here is also taken as constant at $\approx 1200eV$. As the neon enters the plasma, the modelling suggests that the large

Table 5.1: *Impurity concentrations in COMPASS-D, only the most abundant impurities are considered. Ne is used in Ne gas puffing experiments only.*

Impurity	$\frac{n_I}{n_e}$
B	4×10^{-3}
C	4×10^{-3}
O	9×10^{-4}
Cl	9×10^{-5}
Ne	3×10^{-2}

increase in the continuum signal results mainly from an increase in the radiative recombination contribution.

The exponential dependence of the continuum intensity on the electron temperature and the dependence on n_e^2 require a great deal of confidence in these measurements for this method to be used as a direct measure of Z_{eff}. In the visible region where this method is usually used, the exponential term disappears as the photon energy is small compared with the electron temperature.

5.2 Absolute Line Intensity Measurements

As described in the previous chapter Cl XVI spectra from many different plasma conditions are available for analysis. In this chapter we shall attempt to analyse the variation of spectral line intensity with the changing plasma parameters.

The line intensity is given by equation (3.1) and the excitation rate is given by equations (3.6) and (3.7). Taking into account the line of sight measurement, the resonance line intensity is given by

$$B = \frac{2}{4\pi}\int_{a_1}^{a_2} n_e n_{ClXVI} C_w(T_e) dx \ photons\ cm^{-2}\ s^{-1}\ sr^{-1}. \qquad (5.15)$$

We shall model the w line intensity only and assume that the entire intensity is due to electron impact excitation (this is a valid approximation for the w line, but would not be for the x, y and z lines, see section 3.1.1); the satellite contribution and continuum are eliminated by the line fitting procedure. We shall examine two density regimes; $\overline{n_e} = 2 \times 10^{19} m^{-3}$ and $\overline{n_e} = 1 \times 10^{20} m^{-3}$ and

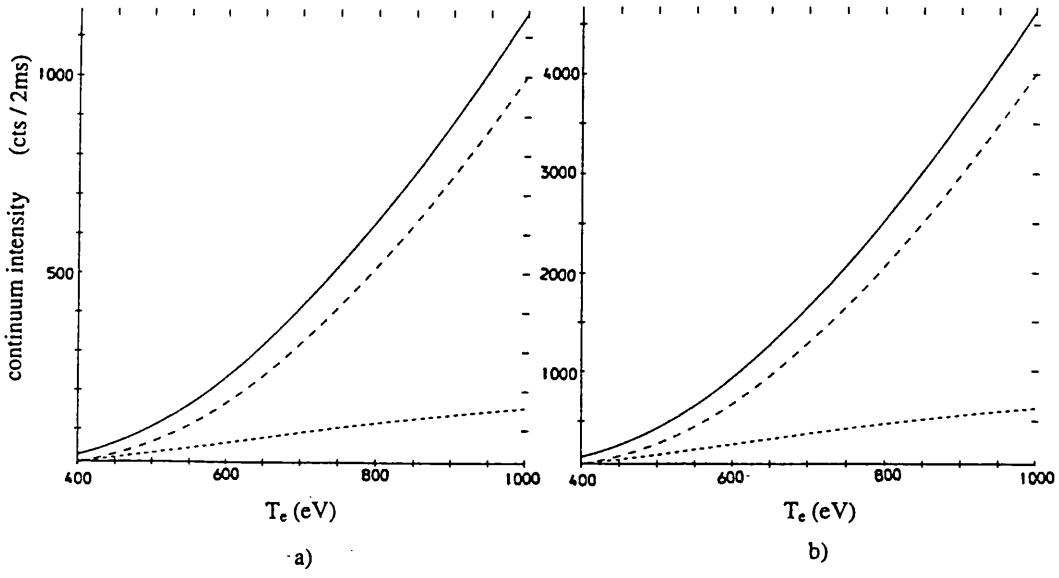

Figure 5.3: *Model of continuum during H-mode a) before the onset of the H-mode b) during the H-mode as in Figure 5.2. T_e remains constant at 600 eV during the pulse. The full lines indicate the total continuum signal, the dashed line is the bremstrahlung contribution and the dotted line is the radiative recombination contribution.*

at the higher density we can examine any differences between L and H-mode discharges and between ELM free and ELMy H-modes. Figure 5.6 is a plot of measured line intensity against electron temperature for these cases. The line intensity is taken as the area under the line, calculated from the fitted height $\times$ the fitted width $\times$ a factor given by [Tudor Davis and Vaughan 1963] which relates the height and width of a Voigt function to the area under the line.

From the figure we see that there is not very much difference in the absolute line intensity between the different density regimes, but the low density points represent higher temperatures than the high density points (see previous chapter), and we also notice for both regimes an increase in intensity with temperature. At the higher density there is no clear distinction in the Cl intensity between ELMy H-modes and L-mode plasmas, but there is a difference in the Cl

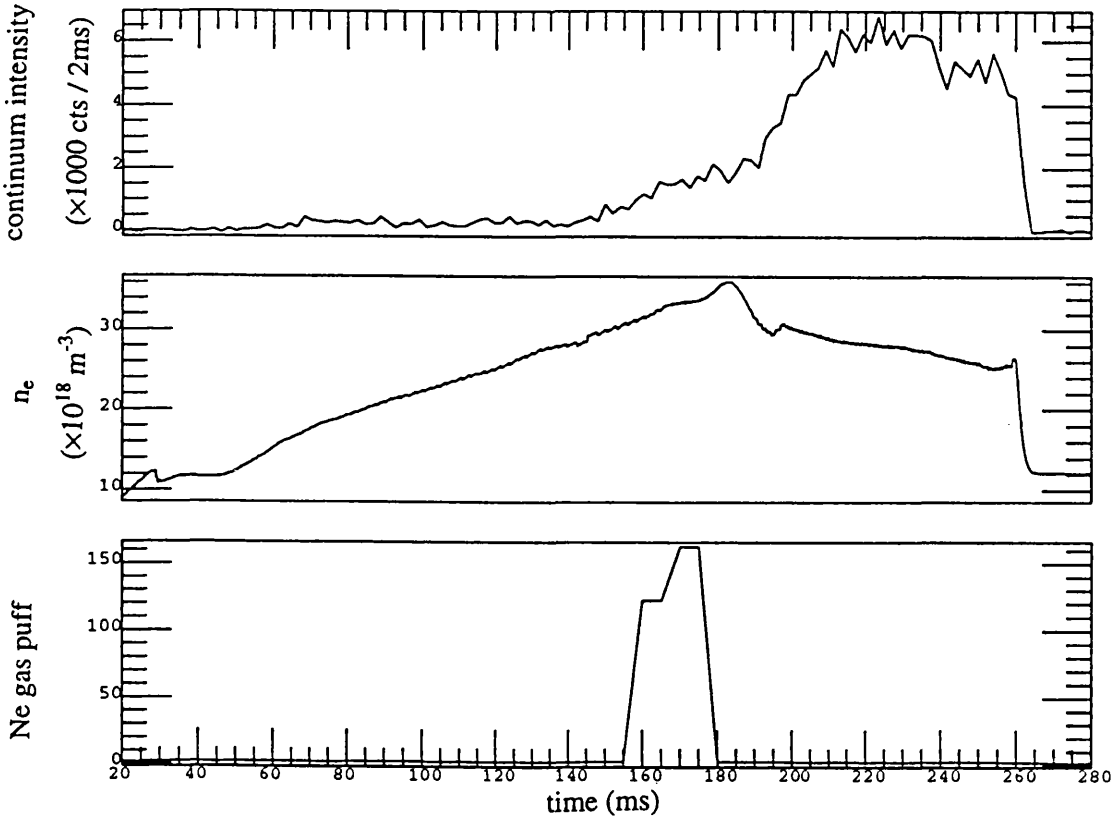

Figure 5.4: *Time history of continuum during Ne gas puff (top), the density middle) and the timing of the Ne gas puff (bottom). # 14368.*

intensity between ELM free H-modes and the other high density plasmas.

A coronal model of chlorine for these two density regimes is also shown in Figure 5.6. The model assumes that the emission shell remains centred around the magnetic axis with a constant thickness of 10 cm, and that the impurity concentration also remains constant despite the large changes in T_e. More accurate work would require a knowledge of the changes in the electron temperature profile and the resultant changes to the emission shell thickness as T_e changes. We find that we require a concentration of $\approx 5 \times 10^{-4} \times n_e$ for the lower density and a decreased concentration of $\approx 8 \times 10^{-5} \times n_e$ at the higher density in order to give the measured line intensities. This is not a surprising result as one would expect an intrinsic impurity to become more diluted as the electron density in-

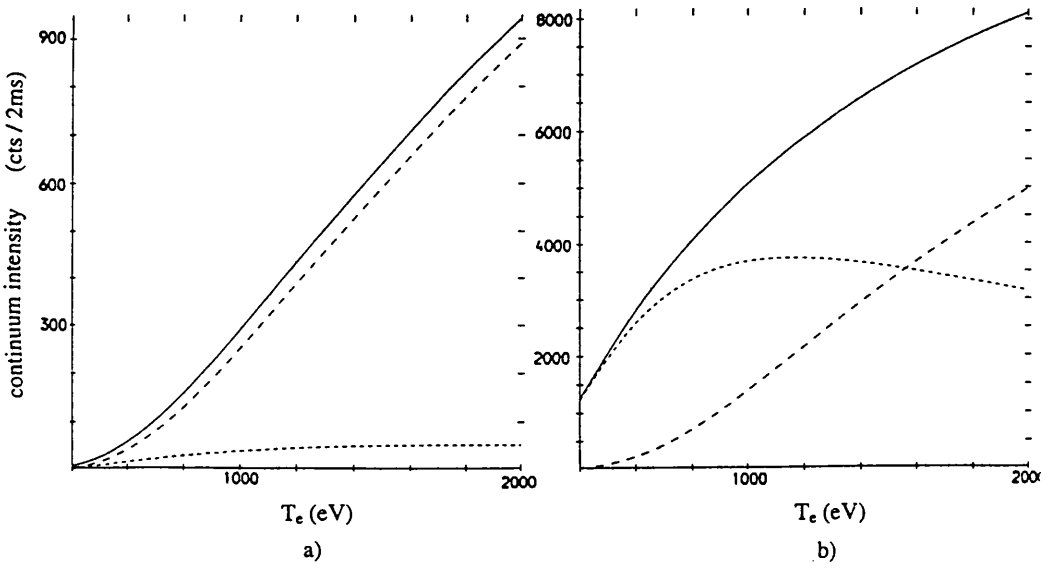

Figure 5.5: *Model of continuum during gas puffing a) before the gas puff b) after the gas puff as in Figure 5.4. T_e remains at a constant 1200 eV during the pulse. The full lines indicate the total continuum signal, the dashed line is the bremstrahlung contribution and the dotted line is the radiative recombination contribution.*

creases, the reason being that the sputtering rate from the vessel wall decreases at higher densities as the edge electron temperature decreases.

The Cl XVI levels in ELM free discharges appear to be slightly higher than the other discharges in the same density regime. One possible explanation is that the impurity concentration is greater hence showing some evidence of increased impurity confinement for these plasma discharges.

5.2.1 Temporal Behaviour of Line Intensities

Changes in the impurity concentration during a plasma pulse can be found by dividing the w line intensity by a power of the density. Dividing by $\overline{n_e}$ gives the impurity abundance whilst dividing by $\overline{n_e}^2$ gives the fractional impurity concentration (as a fraction of n_e). Accumulation is defined as an increase in the

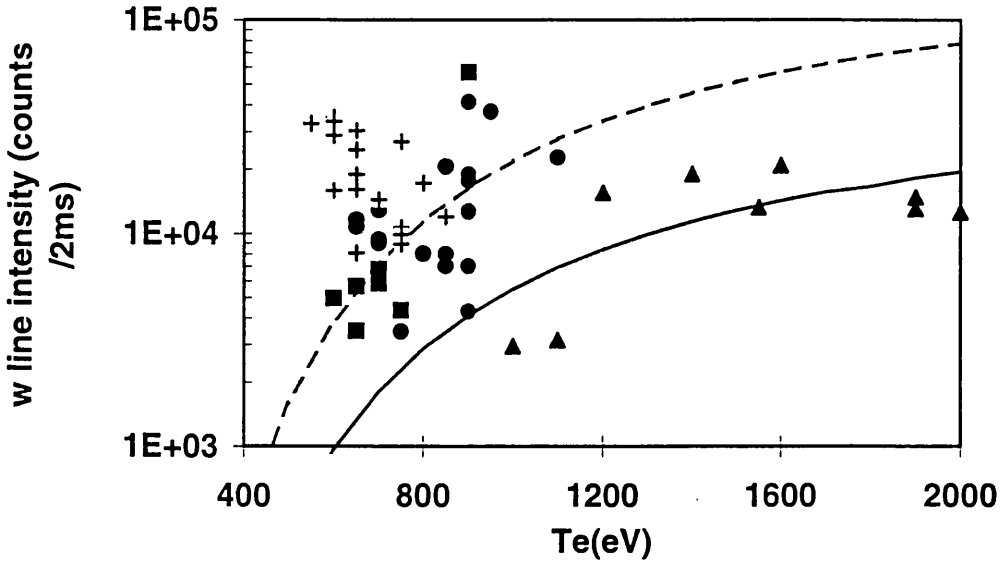

Figure 5.6: *Measured intensity of the w line for various plasma conditions. Triangles -* $\overline{n_e} = 2 \times 10^{19} m^{-3}$. *The others symbols are all at* $\overline{n_e} = 1 \times 10^{20} m^{-3}$, *but differ according to confinement regime, squares - L-mode, circles - ELMy H-mode, crosses - ELM free H-mode. Full line coronal model* $\overline{n_e} = 2 \times 10^{19} m^{-3}$, *dashed line coronal model* $\overline{n_e} = 1 \times 10^{20} m^{-3}$. *The impurity concentrations for the coronal model are* $n_{imp} \approx 5 \times 10^{-4} \times n_e$ *for the lower density and* $n_{imp} \approx 8 \times 10^{-5} \times n_e$ *at the higher density. The emission region is assumed to be the central* $10cm$ *of the plasma.*

fractional impurity concentration (assuming that the source strength remains constant). We shall examine three plasma pulses, one high density L-mode pulse, one ELMy H-mode and one H-mode with ELM free periods. In these discharges the Cl signal does not become significant until $\approx 100ms$ after the start of the plasma. It is not clear why at these densities there is such a long rise time. At lower densities the Cl begins to rise much earlier on in the pulse ($\approx 20ms$). It may be related to the observation that impurities injected into the plasma by laser ablation at these high densities also show very long rise times [Peacock et al 1995].

The three pulses are shown in Figures 5.7, 5.8 and 5.9. For each pulse, the raw w line intensity is shown with the background removed, this is then divided by $\overline{n_e}$ and then by $\overline{n_e}^2$. The other two signals shown are the line average density

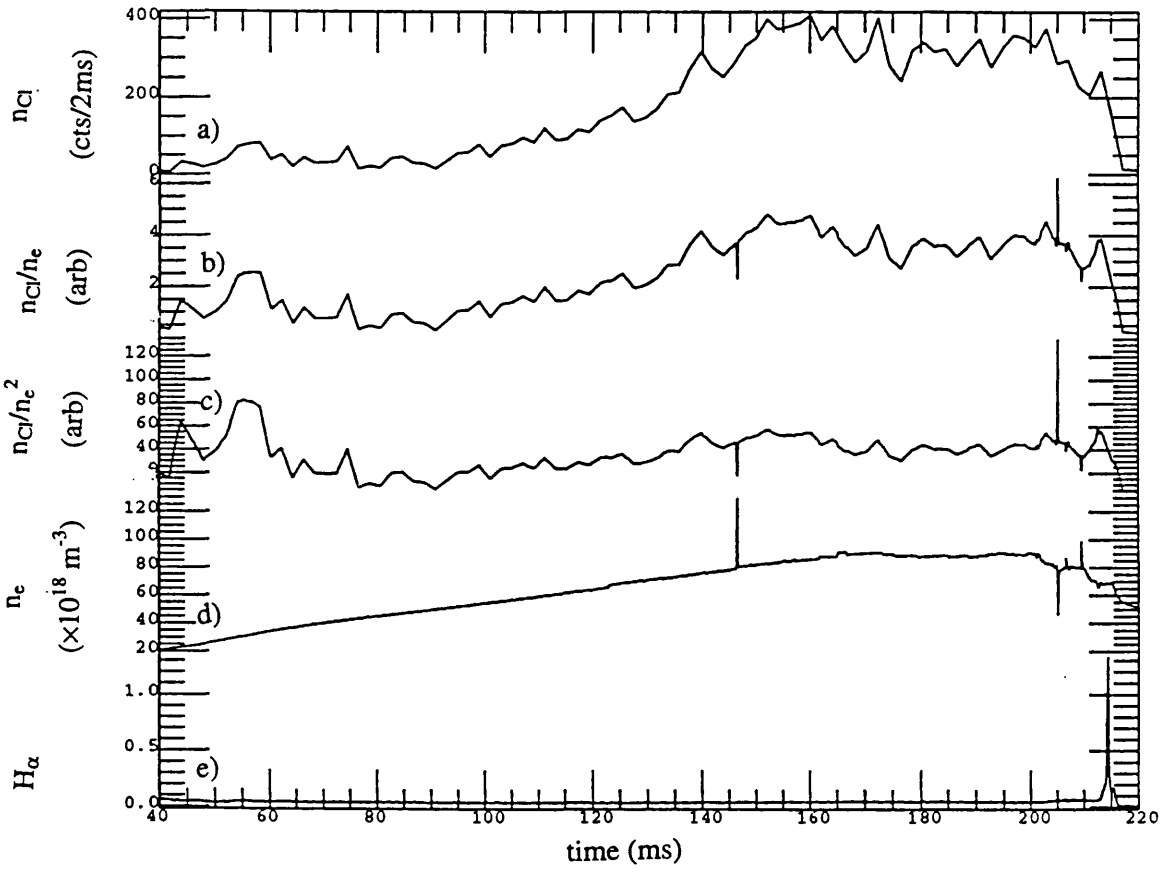

Figure 5.7: *Time history of the w line during an L-mode discharge. a) raw signal* I_w *b)* $\frac{I_w}{\overline{n_e}}$ *c)* $\frac{I_w}{\overline{n_e}^2}$ *d) the density measurement used for the above division e)* H_α*. COMPASS-D shot # 14842.*

(used for the division) and the H_α signal as the H-mode indicator.

In the L-mode discharge #14842, Figure 5.7, after the slow rise in the Cl signal, the intensity flattens off and even drops a little before the end of the pulse. After dividing by $\overline{n_e}$, $\frac{I_w}{\overline{n_e}}$ does show an increase.However $\frac{I_w}{\overline{n_e}^2}$ shows very little change throughout the discharge. This indicates that any increase in the impurity emission during this pulse is due to changes in the electron density, there does not appear to be any change in the impurity concentration. The same excercise can be repeated for the background signal. This is shown for #14842 in Figure 5.10. Here again, the raw signal rises, but when divided by $\overline{n_e^2}$ there is very little change.

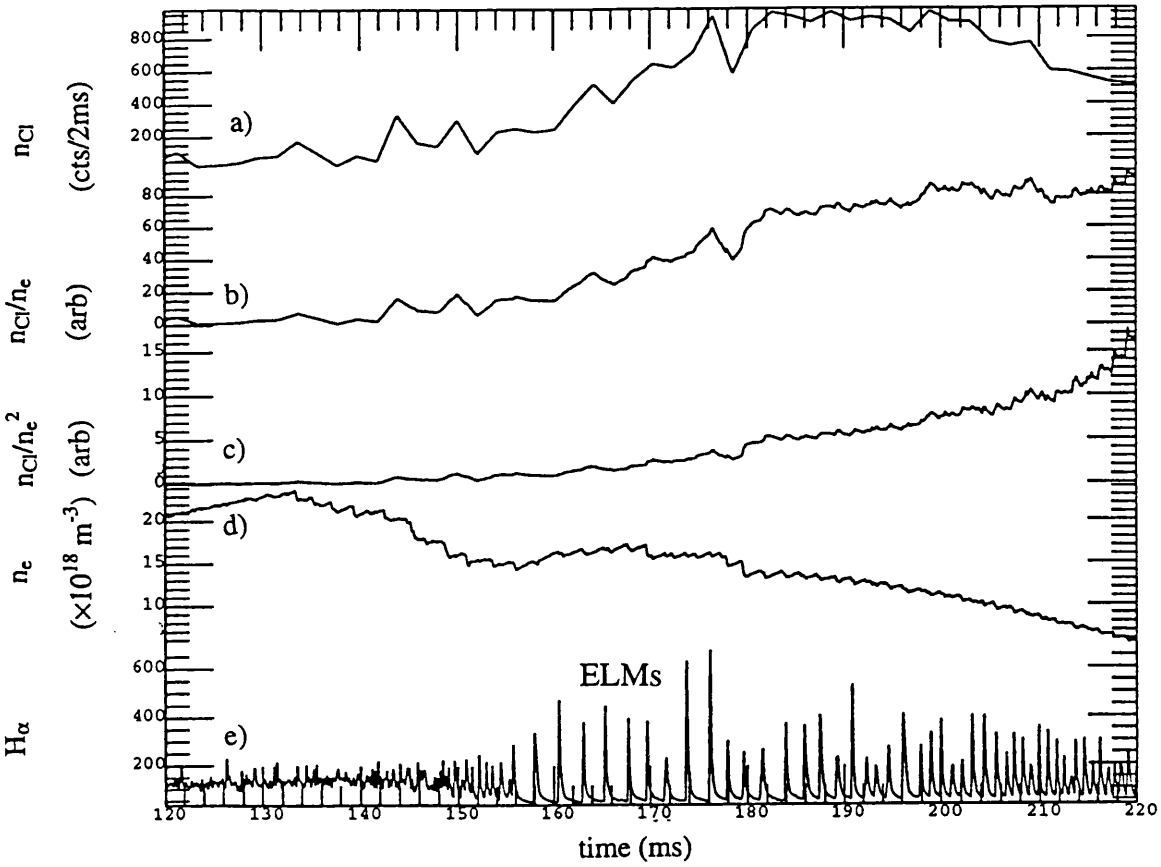

Figure 5.8: *Time history of the w line during an ELMy H-mode discharge. a) raw signal I_w b) $\frac{I_w}{n_e}$ c) $\frac{I_w}{n_e^2}$ d) the density measurement used for the above division e) H_α. COMPASS-D shot # 12546.*

We can also compare the w line intensity with the total soft x-ray signal which shows that the two signals show similar behaviour, Figure 5.13, i.e. the time variation of the Cl line emission is similar to the total soft x-ray emission from the plasma.

Plasma pulse #12546 is an ELMy H-mode discharge, Figure 5.8. The ELM frequency increases during the duration of the pulse, as the density decreases. The Cl signal begins to rise at the onset of the ELMs at $\approx 150ms$ and continues to rise for $\approx 40ms$ and then decreases while the electron density drops throughout. Initially no change is seen in $\frac{I_w}{n_e^2}$, this only increases towards the end of the pulse when the density falls off faster than the Cl signal. The background signal for

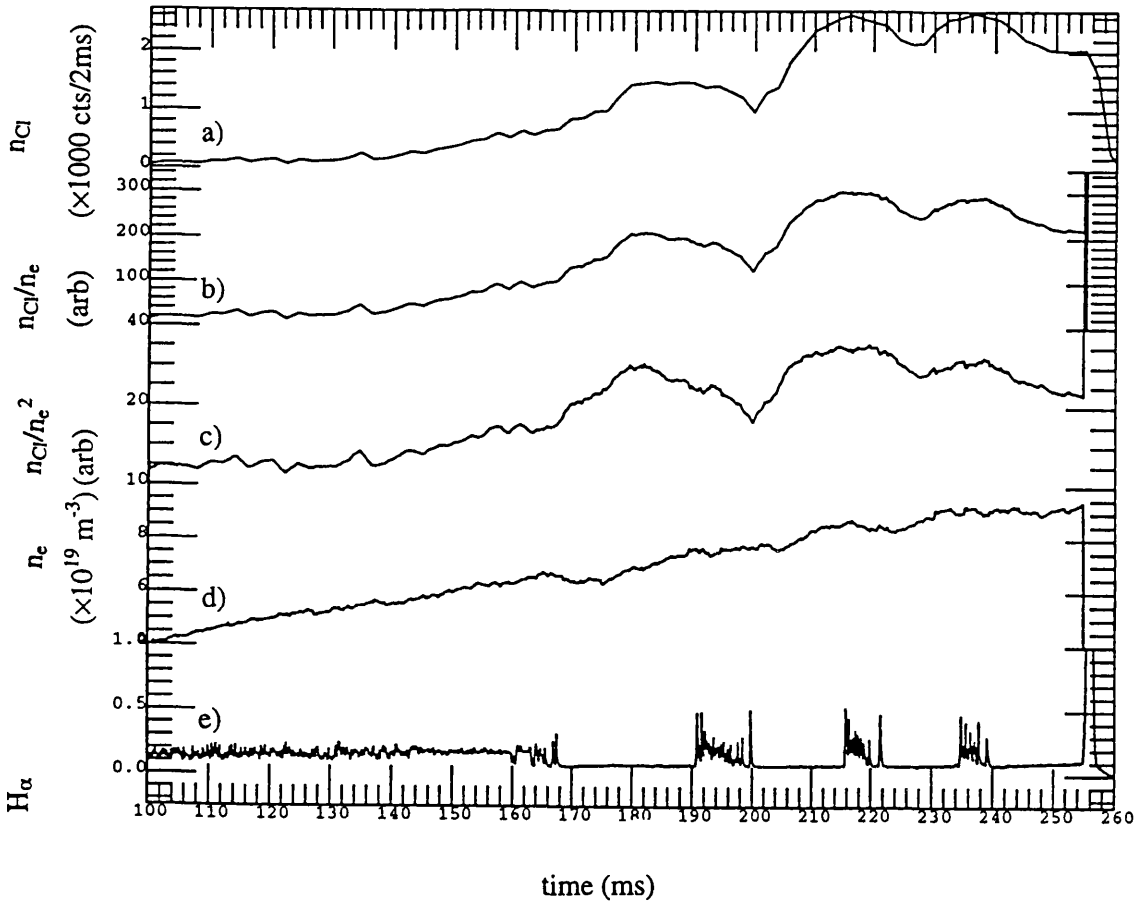

Figure 5.9: *Time history of the w line during an H-mode discharge with ELM free periods. a) raw signal I_w b) $\frac{I_w}{n_e}$ c) $\frac{I_w}{n_e^2}$ d) the density measurement used for the above division e) H_α. COMPASS-D shot # 13460.*

this pulse was too weak for any measurements so we show the background from a similar pulse # 14809, Figure 5.11, which starts with a short ELM free period and then becomes ELMy. There is a little variation in the background signal during this discharge. When divided by $\overline{n_e}^2$ there is no measurable change in the signal. Figure 5.14 shows a comparison of the Cl w line with the central soft x-ray chord, the rise and fall times are very similar.

Plasma discharge #13460 has long ELM free periods, separated by short ELMy periods, Figure 5.9. The w line intensity rises during the first three ELM free periods and then falls. However the intensity modulation is not directly correlated with the ELM behaviour. This is also true of $\frac{I_w}{n_e}$ and $\frac{I_w}{n_e^2}$. An important

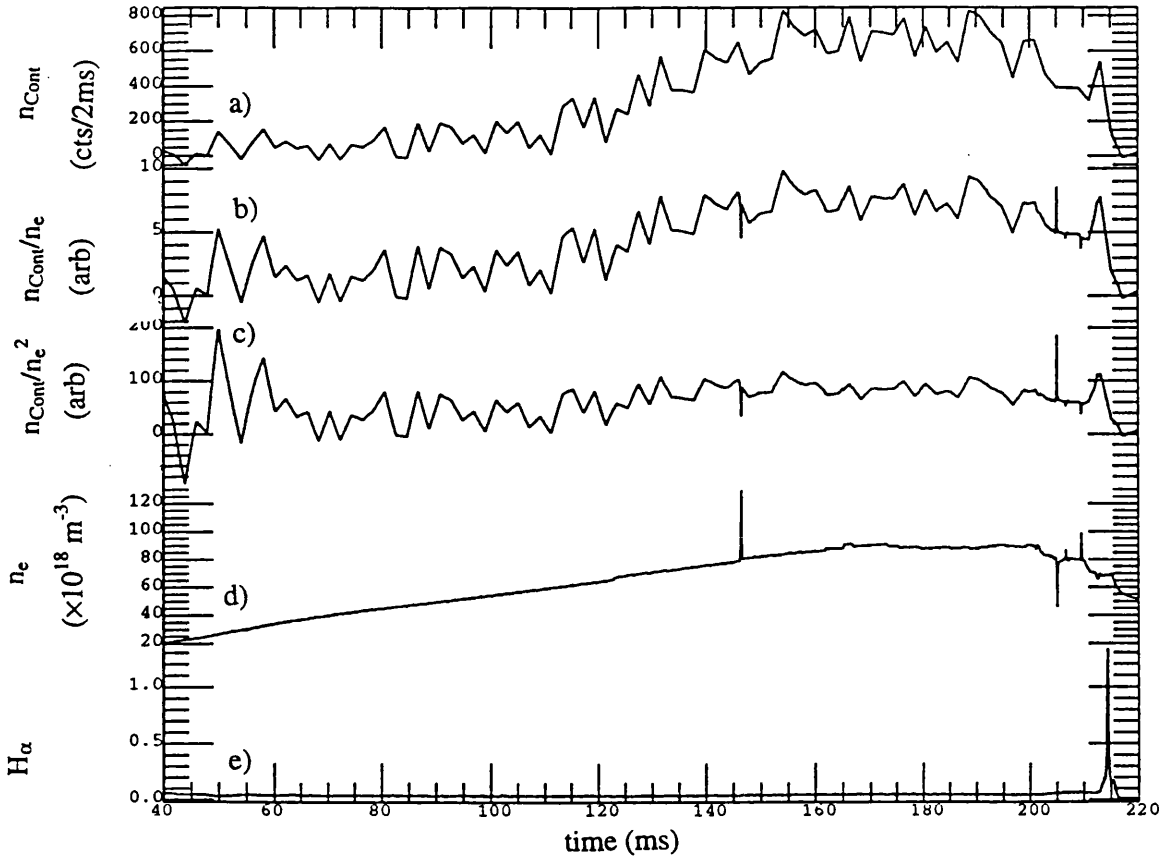

Figure 5.10: *Time history of continuum during an L-mode discharge. a) raw continuum signal $\lambda = 4.4\mathring{A}$ b) continuum divided by $\overline{n_e}$ c) continuum divided by $\overline{n_e}^2$ d) the density measurement used for the above division e) H_α. COMPASS-D shot # 14842.*

correction factor in these discharges arises from the dependence of the emissivity on T_e which is generally falling during these pulses as the density increases (e.g. see Figure 4.3), (although there is a small rise in temperature as the plasma returns to an ELM free H-mode after an ELMy period). These temperature rises of $\approx$ 5% would increase the Cl line intensity by $\approx$ 20% (see Figure 5.6). The measured change in the Cl concentration is $\approx$ 50%. During this discharge, the soft x-ray signal is saturated, but for a similar pulse #14817 we can plot the soft x-ray signal at different radii to show how the effects of the ELMs penetrate into the plasma, Figure 5.15. The edge channels, as expected, are more influenced by

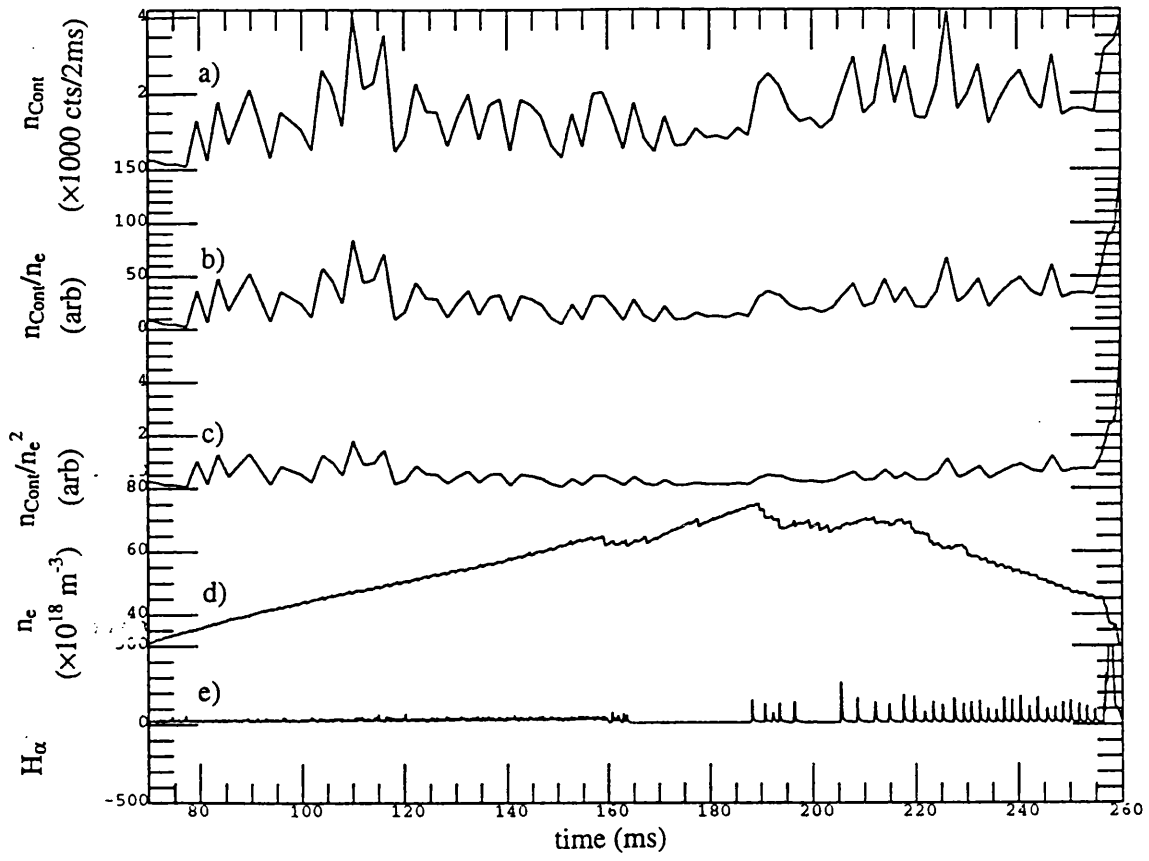

Figure 5.11: *Time history of continuum during an ELMy H-mode discharge. a) raw continuum signal $\lambda = 4.4\AA$ b) continuum divided by $\overline{n_e}$ c) continuum divided by $\overline{n_e}^2$ d) the density measurement used for the above division e) H_α. COMPASS-D shot # 14809.*

the onset of the ELMs at 192 ms and 220 ms and change occurs immediately: in the core, there is a 5 ms delay and a much smaller change. When comparing the Cl signal with the soft x-ray signal (central channel), Figure 5.16, we again find that the signals are very similar to one another. The rate of rise is the same, and both respond to the ELMs together at $\approx 196ms$. The fall in the Cl XVI signal is larger than the drop in the soft x-ray signal. The two signals begin to diverge at $220ms$ when the Cl signal begins to drop and the soft x-ray signal continues to rise and saturates. In this case, the continuum intensity when divided by $\overline{n_e}^2$ shows a small increase at the start of the first ELM free phase, but then remains

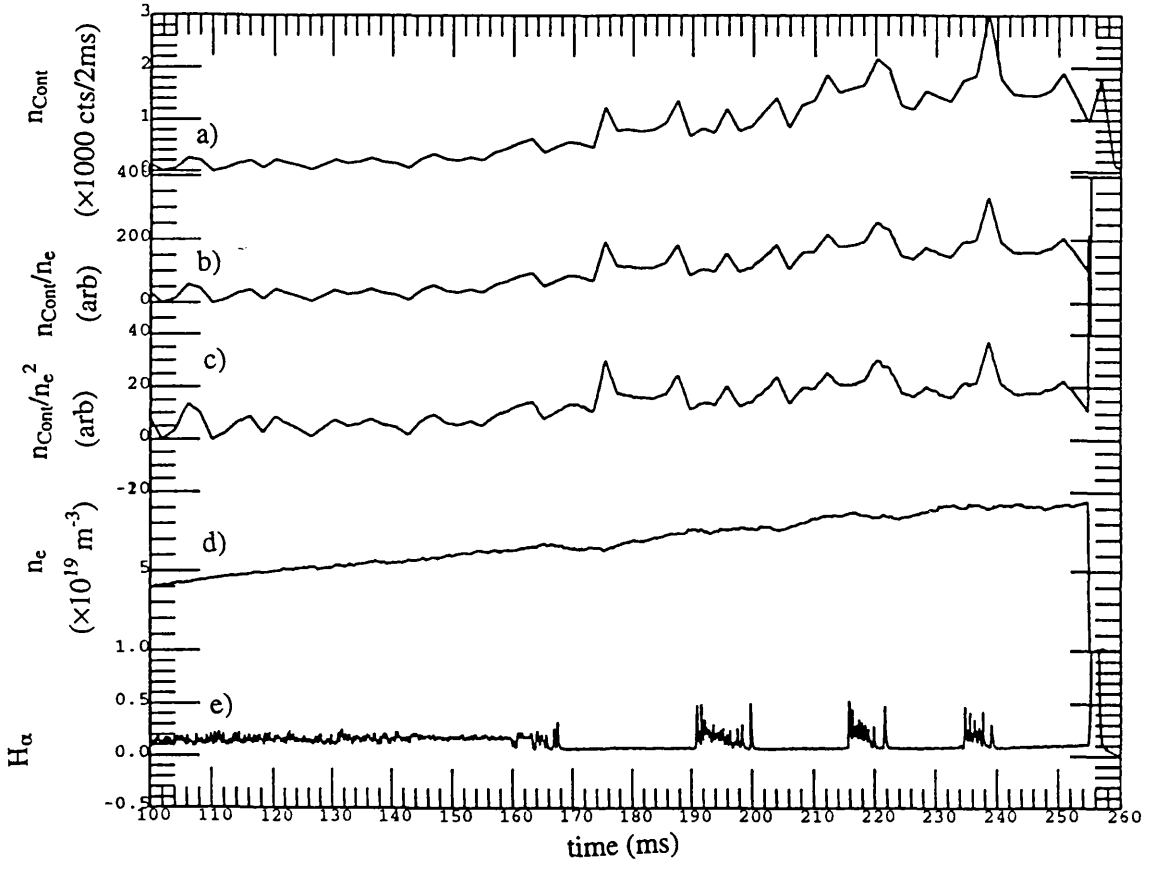

Figure 5.12: *Time history of continuum during an ELM free H-mode discharge. a) raw continuum signal $\lambda = 4.4\mathring{A}$ b) continuum divided by $\overline{n_e}$ c) continuum divided by $\overline{n_e}^2$ d) the density measurement used for the above division e) H_α. COMPASS-D shot # 13460.*

at a constant level, rather than continuing to rise as the raw signal does. The continuum does not respond to the ELMs, Figure 5.12.

The penetration into the plasma of the ELM effects on the soft x-rays as shown in Figure 5.15 is almost instantaneous for the edge channels (channels 1 to 5) and slower for the central channels. The effect seen at the edge is also much greater than that seen at the centre. The fast response at the edge channels is thought to be a direct result of the MHD activity of the ELMs whereas what happens at the centre on a *ms* timescale later is the reaction of the plasma centre to energy and transport changes at the plasma edge which occur as a result of

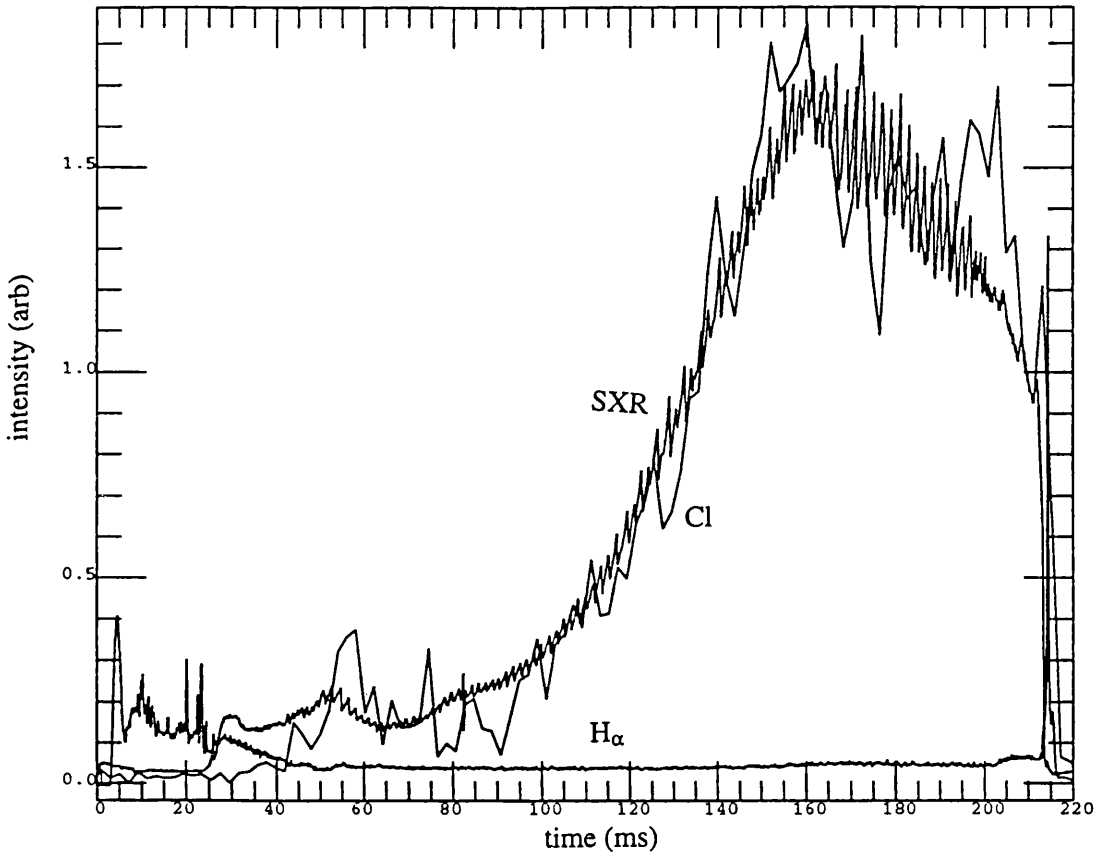

Figure 5.13: *Total soft x-ray signal (at plasma centre) compared with the Cl w line intensity. Also shown is the H_α trace. L-mode shot # 14842.*

the breakdown of the transport barrier.

At this point it would seem appropriate to add a note about the expected error bars in Figures 5.7 to 5.16. The modulations seen in the soft x-ray signals e.g. Figure 5.16 are due to sawtooth activity in the plasma. The time resolution of the curved crystal spectrometer is not fast enough to follow this. The fluctuations in the Cl signal are not thought to be related to MHD activity in the plasma, but rather are a reflection of the size of the error bars on the measurement. The fluctuations in the continuum signal are therefore greater than the fluctuations in the w line intensity.

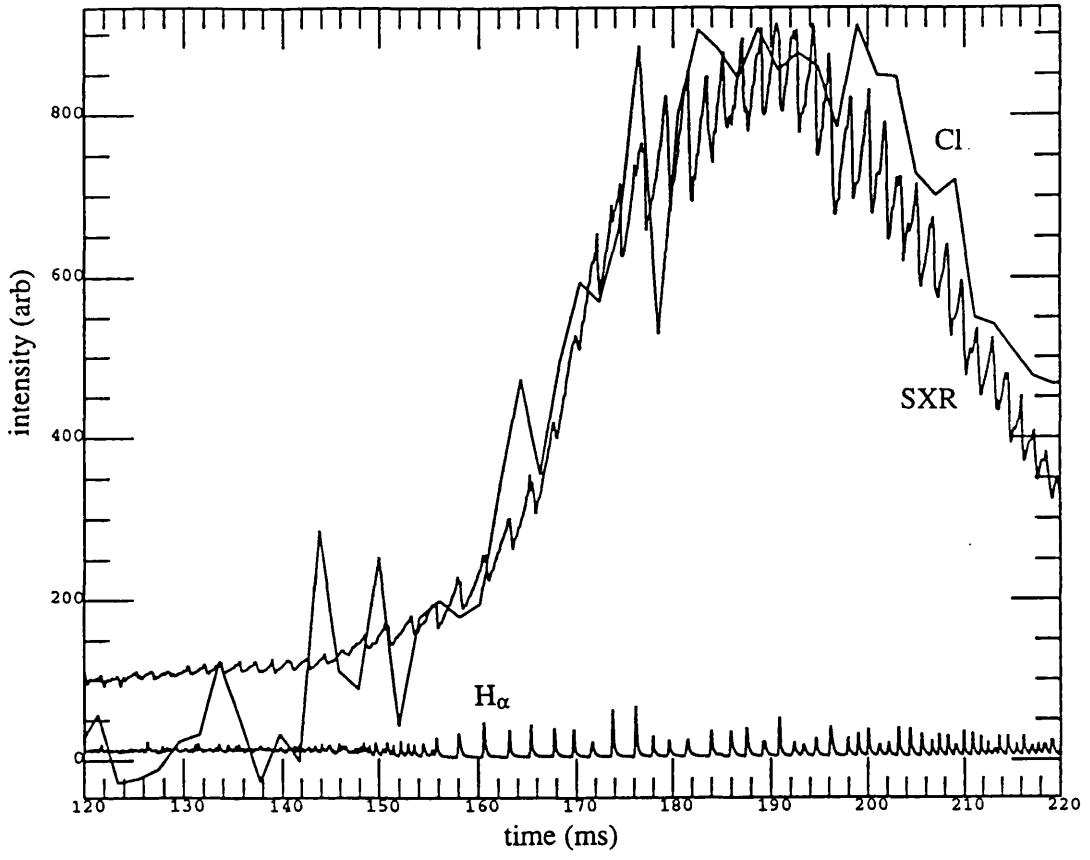

Figure 5.14: *Total soft x-ray signal (at plasma centre) compared with the Cl w line intensity. Also shown is the H_α trace. ELMy H-mode shot # 12546.*

5.3 Discussion

In neoclassical theory particle fluxes are driven by pressure gradients. The bulk ions in a typical tokamak are in the plateau regime and will tend to diffuse outwards. The heavier impurity ions are usually in the Pfirsch - Schlüter regime. Ambipolarity of the total flux is usually assumed i.e. $\sum_j Z_j \Gamma_j = 0$. The particle flux for impurities is, considering neoclassical terms only, given by [Fussman 1992];

$$\Gamma_I = -D_I \frac{\partial n_I}{\partial r} + D_I Z \left(\frac{\partial \ln n_i}{\partial r} + H \frac{\partial \ln T_i}{\partial r} \right) n_I, \qquad (5.16)$$

where H is a parameter dependent on the collisionality of the background and impurity ions and is known as the neoclassical thermodiffusion coefficient (the

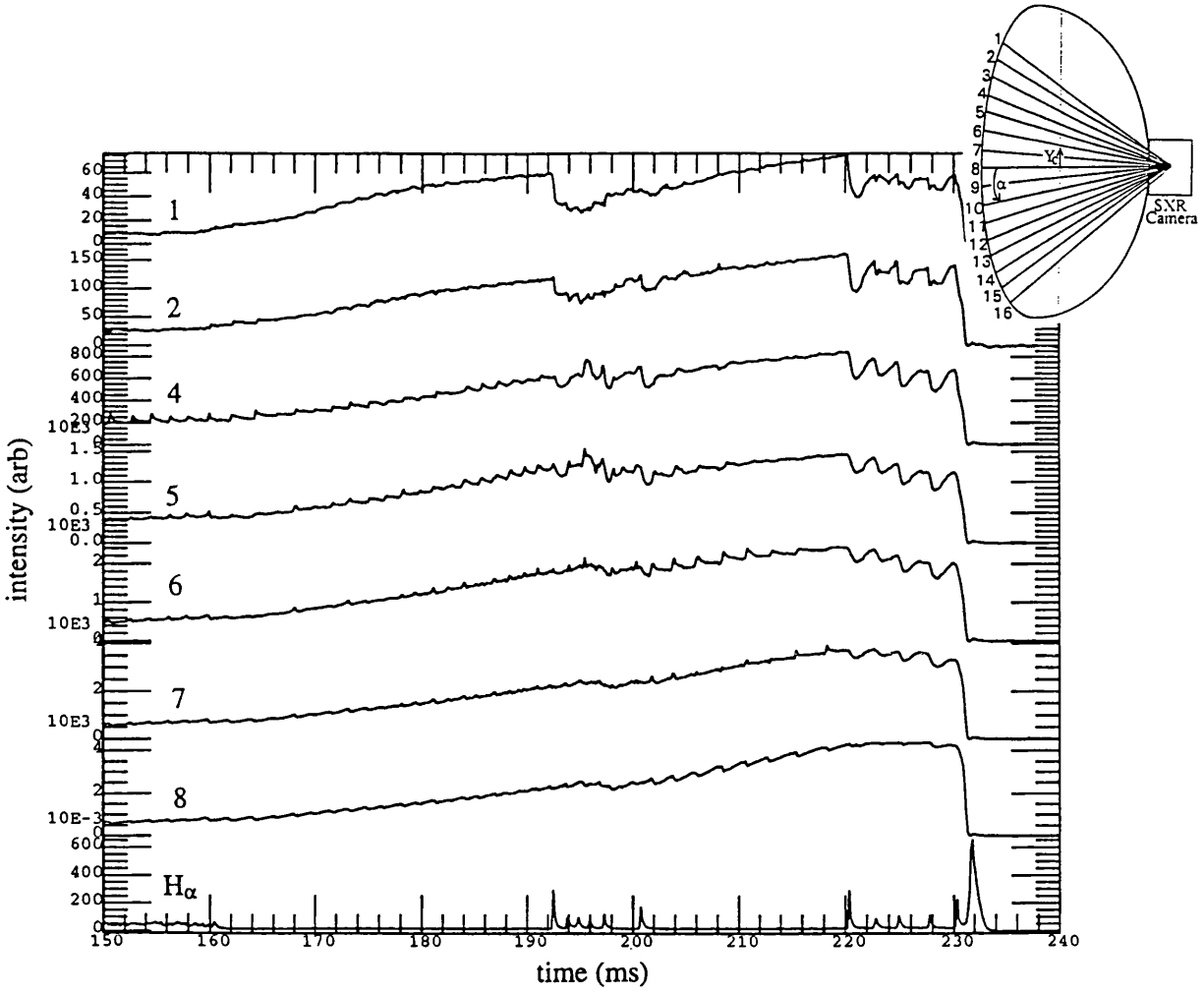

Figure 5.15: *Soft x-ray channels from the edge (1) to the centre (8) during an ELM free H-mode. The edge channels respond to the ELMs immediately whilst there is a delay of* $\approx$ *5ms in the central channels. COMPASS-D shot # 14817*

equation reflects the effects of the background ion gradients (i) on the impurity ion gradients (I)). The sign of H and hence the direction of the impurity flux is dependent on the collisionalities of the background ions and impurity ions. Values of H as given by [Fussman 1992] are shown in Table 5.3.

For steady state conditions in the absence of temperature gradient forces on the impurities, equation (5.16) becomes

$$\frac{n_I(r)}{n_I(0)} = \left(\frac{n_i(r)}{n_i(0)}\right)^{\frac{z_I}{z_i}}, \tag{5.17}$$

which represents impurity accumulation in the plasma core.

In reality, as discussed in the previous chapter, the observed diffusion is

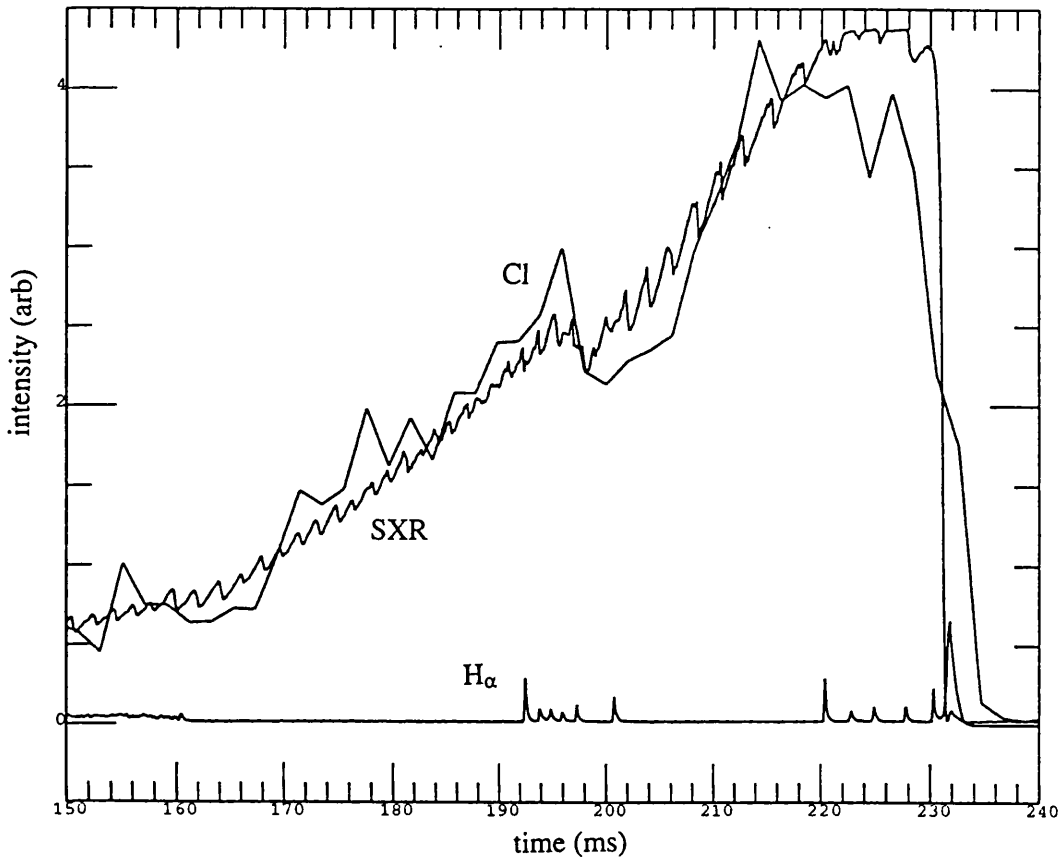

Figure 5.16: *Total soft x-ray signal (at plasma centre) compared with the Cl w line intensity. Also shown is the H_α trace. Both signals respond to the ELMs at 192 ms together with a delay of $\approx 5ms$. H-mode shot # 14817.*

anomalous. Impurity transport is modelled with anomalous diffusion and convection coefficients as in equation (1.23). D is usually in the range $0.1 < D < 1m^2s^{-1}$ and the dimensionless convection parameter $S = \frac{aV}{2D}$ is in the range $1 < S < 3$.

Taking account of anomalous transport, equation (5.17) must be modified to [Fussman 1992];

$$\frac{n_I(r)}{n_I(0)} = \left(\frac{n_i(r)}{n_i(0)}\right)\left[\left(\frac{T_i}{T_i(0)}\right)^H \left(\frac{n_i}{n_i(0)}\right)\right]^{\frac{\beta}{1+\beta}(Z-1)}, \qquad (5.18)$$

where $\beta = \frac{D_{z\ neocl}}{D_{anom}}$ ($\beta = 0.1$ - L-mode and $\beta > 1$ - H-mode). The accumulation thus depends on three parameters; the impurity charge Z; the neoclassical ther-

Table 5.2: *The neoclassical thermodiffusion coefficient as given by [Fussman 1992].*

		Background Ions		
		banana	plateau	Pfirsch-Schlüter
Impurities	banana	-0.5 to -0.1	-	-
	plateau	+1.5	+1.5	-
	Pfirsch-Schlüter	-0.5	-0.5	-0.5 to 0

modiffusion coefficient H and the ratio of the neoclassical diffussion coefficient to the anomalous diffusion coefficient β, and also on the peaking of the background ion temperature and density gradients.

The improved energy confinement during H-modes is accompanied by improved impurity particle confinement [Hawkes et al 1989]. The transport barrier is characterised by a large inwards convection at the edge. The transport parameters, D and V, are both reduced during the H-mode, except for the edge convection term which increases, and are shown for COMPASS-D in Figure 5.17. These values of D and V were calculated from laser ablation of aluminium into COMPASS-D H-mode and L-mode plasmas [Peacock et al 1994]. Those impurities outside the transport barrier do not accumulate during the H-mode, whilst those inside are prevented from being lost and hence do accumulate in the plasma. ELMs which are MHD instabilities at the plasma edge periodically deplete the plasma of impurities and hence an ELMy H-mode will not accumulate impurities. ELM control is an important research area as a fusion reactor can only be used in the H-mode if the ELM frequency is sufficient to prevent impurity accumulation.

Weak accumulation ($\approx \times 2$) has been observed in Cl XVI on COMPASS-D during ELM free H-modes, but this is not seen in the continuum. Photon statistics for the narrow region of continuum radiation viewed are much lower than those for the lines and this may hide any small variations in the intensity. Changes in the plasma pressure profile during the H-mode could increase the line of sight integral of the line intensity to give the effects seen, but if this were the

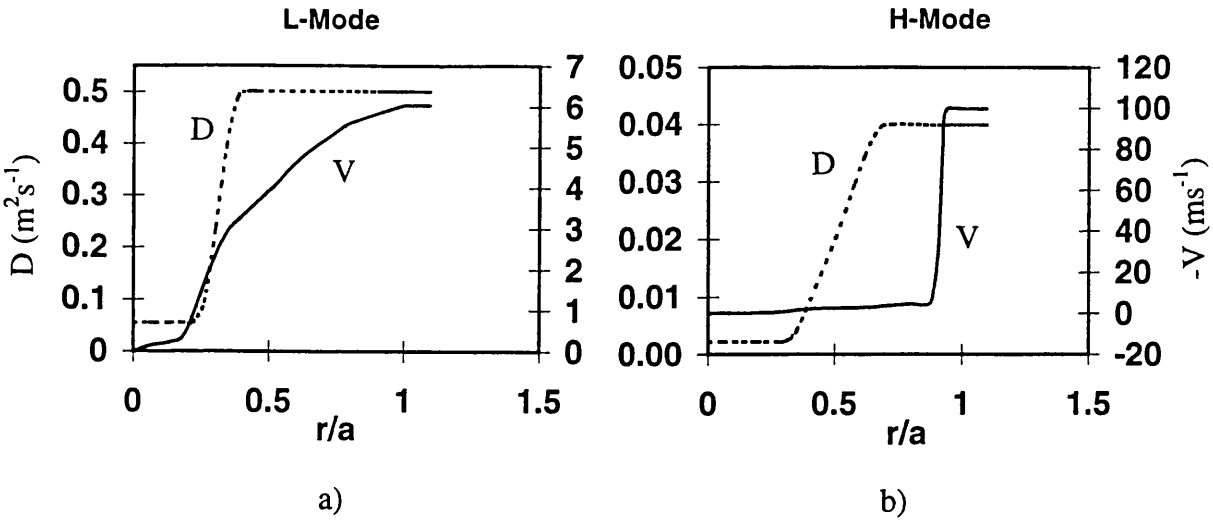

a) b)

Figure 5.17: *D and V parameters in COMPASS-D. a) Derived from L-mode shot #12016. b) Derived from H-mode shot # 12210. D is reduced during the H-mode and the transport barrier is formed by the high value of V at the plasma edge.*

case we would expect to see a similar increase in the continuum. A possible conclusion from these results is that the accumulation is confined to mid and high z elements which are only present as trace impurities whereas the continuum is dominated by the more abundant light elements which do not accumulate. The accumulation seen is believed to be related to the increased particle confinement time during H-modes. However, it is unlikely that conditions are such for neoclassical accumulation to be considered significant.

Chapter 6

Rotation Measurements

Changes of fluid motion can occur in a tokamak plasma due to the input of momentum as in the case of neutral beam injection, or due to changes in the electric field profile as in the case of the H-mode. In some cases MHD modes which are resonant on the magnetic surfaces can form magnetic islands and act as a brake on the plasma motion. The fluid equation of motion for a single species j is given by

$$m_j n_j \left[\frac{\partial \mathbf{v}_j}{\partial t} + (\mathbf{v}_j.\nabla)\mathbf{v}_j\right] = qn(\mathbf{E} + \mathbf{v}_j \times \mathbf{B}) - \nabla.\mathbf{\Pi}_j - \frac{n_i m_i \mathbf{v}_i - n_j m_j \mathbf{v}_j}{\tau}. \quad (6.1)$$

where $\mathbf{v}_j$ is the fluid velocity vector for species j, $\mathbf{E}$ is the electric field vector and $\mathbf{B}$ is the magnetic field vector.

The left hand side is the convective derivative which is the time and spatial elements of the momentum term expressed separately;

$$\frac{dv(x,t)}{dt} = \frac{\partial v}{\partial t} + \frac{\partial v}{\partial x}\frac{\partial x}{\partial t} = \frac{\partial v}{\partial t} + v\frac{\partial v}{\partial x}. \quad (6.2)$$

The first term on the right hand side consists of the Lorentz force which acts on the individual particles. The second term on the right, $\mathbf{\Pi}$, is the stress tensor, which includes the viscous forces and the pressure gradient. The final term is the friction force which is due to Coulomb collisions between particle species i and j, τ is the mean free time between collisions. A diagram showing the coordinate system used here is shown in Figure 6.1.

If we assume steady state conditions, and that the $(\mathbf{v}.\nabla)\mathbf{v}$ term is negligible as in the parallel direction it is usually much smaller than the $\frac{\partial \mathbf{v}}{\partial t}$ term and there

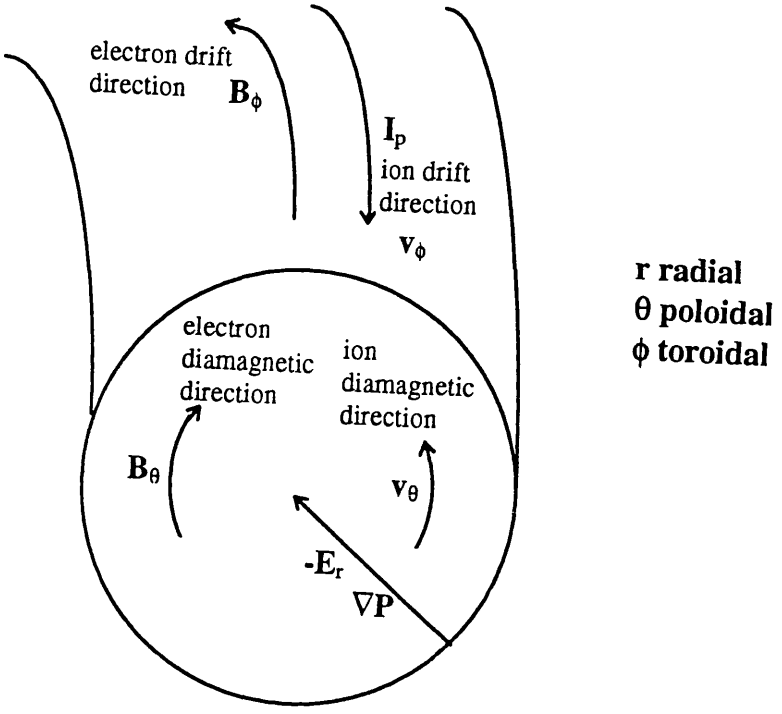

Figure 6.1: *Coordinate system showing the toroidal and poloidal directions, and the terms used in equation (6.1).*

is no contribution in the perpendicular (diamagnetic) direction. We shall ignore viscosity for the time being and only consider the pressure gradient part of the stress tensor, and we shall ignore friction. Equation (6.1) then becomes;

$$qn(\mathbf{E_r} + |\mathbf{v} \times \mathbf{B}|_r) = \frac{\partial P}{\partial r}, \tag{6.3}$$

where $\frac{\partial P}{\partial r}$ is now the pressure gradient.

Plasma fluid motion can be observed by measurement of Doppler shifts of impurity spectral lines;

$$\frac{v}{c} = \frac{\delta\lambda}{\lambda}, \tag{6.4}$$

where $\delta\lambda$ is the observed Doppler shift.

Such measurements have been made using Cl XVI lines using the curved crystal spectrometer. It must be pointed out that in the absence of absolute

calibration of the wavelength on our spectrometer only changes of rotation can be measured not the absolute value.

Measurements of plasma rotation can be made using intrinsic radiation from impurities in the plasma. In this case a line of sight integral of the spectrum is obtained. The effects of impurity pressure gradients, ion temperature gradients and toroidal velocity gradients along the line of sight can affect the measurement. The measured rotation is a weighted integral of all the separate rotations at different radii along the line of sight. The effects of the integration are minimised if the emission shell is narrow and peaked. Charge exchange spectroscopy viewing the neutral beam path during neutral beam heating can also be used to measure plasma rotation: this gives a local measurement of the rotation without line of sight effects.

The measurements reported here were made on impurity ions. Neoclassical theory predicts impurity toroidal rotation at the plasma core (close to the magnetic axis) to be against the current direction i.e. in the electron drift direction during ohmic heating and balanced neutral particle injection [Kim et al 1991]. The impurity and bulk ion rotations are predicted to be similar in the plasma core, but can differ quite considerably at the plasma edge [Kim et al 1994].

Core toroidal rotation measurements on COMPASS-D have been made during resonant magnetic perturbation (RMP) mode-locking experiments and during H-modes. Some background theory and the rotation measurements are given together with a brief discussion of the results.

6.1 Mode-Locking

Magnetohydrodynamics (MHD) is the study of the macroscopic properties of plasma fluid motion. The theory involves both electromagnetism and fluid mechanics. The MHD equations consist of Maxwell's equations (in a vacuum);

$$\epsilon_0 \nabla . \mathbf{E} = \sigma, \tag{6.5}$$

$$\nabla \times \mathbf{B} = \mu_0 \mathbf{J}, \tag{6.6}$$

$$\nabla \times \mathbf{E} = -\frac{\partial \mathbf{B}}{\partial t}, \tag{6.7}$$

$$\nabla.\mathbf{B} = 0, \tag{6.8}$$

σ is the charge density and $\mathbf{J}$ is the current density, the equation of motion (equation (6.1)), the equation of continuity;

$$\frac{\partial n}{\partial t} + \nabla.(n\mathbf{v}) = 0, \tag{6.9}$$

the equation of state,

$$p = Cn^{\gamma} \tag{6.10}$$

where p is the pressure, C is a constant, γ is the ratio of the specific heats (at constant pressure and constant volume), and the generalised Ohm's law. MHD theory is valid if the collisionality of the plasma is sufficient to allow the plasma to be treated as a single fluid, and if the scale length of MHD activity is larger than the Debye length (shielding length) such that the fluid can be considered quasi-neutral.

Two forms of the generalised Ohm's law can be considered: i) If the resistivity of the plasma can be considered negligible, Ohm's law is given by;

$$\mathbf{E} + \mathbf{v} \times \mathbf{B} = 0. \tag{6.11}$$

This is known as "ideal MHD". ii) If the resistivity cannot be ignored, Ohm's law becomes;

$$\mathbf{E} + \mathbf{v} \times \mathbf{B} = \eta\mathbf{J}, \tag{6.12}$$

where η is the resitivity, this is known as "resistive MHD".

It is found from MHD theory that the magnetic field lines are lines of constant pressure and that on such lines $\mathbf{J}$ and $\mathbf{B}$ are non-zero. Ideal MHD allows the field lines to be frozen to the plasma frame of reference leading to stable magnetic field configurations. In resistive MHD, field lines are allowed to diffuse through the plasma, thus leading to instabilities.

There are two types of magnetic surfaces in toroidal geometry; rational and irrational. Figure 6.2 shows a magnetic field line winding around the torus. It begins at point 1 and after one circuit it arrives at point 2, a poloidal angle of $\delta\theta$ away from its starting position. The surface can be described by toroidal and poloidal harmonic mode numbers m and n. The rotation transform is given by $l = 2\pi\frac{m}{n}$. If $\frac{m}{n}$ is rational, the field eventually closes in on itself and the surface

is a rational surface, if not, then the field does not close in on itself and it is an irrational surface.

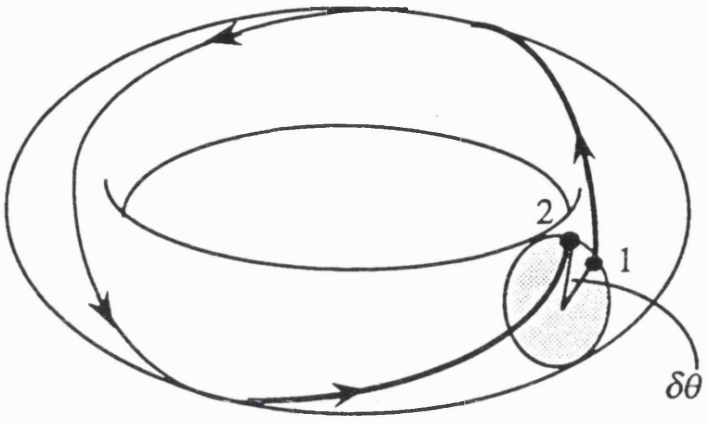

Figure 6.2: *Magnetic surfaces, the surface is rational if the field closes in on itself, if not, it is an irrational surface. From [Hopcraft 1993].*

If the plasma is perturbed; the MHD equations can be used to analyse the effects on the field lines. The perturbation in some cases will grow, and in some cases will be stabilised. The presence of a magnetic field parallel to the perturbation has a stabilising effect. In the presence of a sheared magnetic field, the perturbation is stabilised on surfaces where $\mathbf{k}$ (the wave vector of the perturbation) is parallel to $\mathbf{B}$, and grows on surfaces where $\mathbf{k}.\mathbf{B} = 0$. Such surfaces are called "resonant surfaces". If the instability has mode numbers m and n, the resonant surface will lie on the rational surface $q = \frac{m}{n}$.

Far away from the resonant surfaces, ideal MHD can be used to describe the effects of the perturbation, but close to the surface, the effects of resistivity become important and resistive MHD must be used. Within the region of resistive MHD (close to the resonant surface), the field lines can be torn and then reconnect to form "magnetic islands" around the resonant surfaces. These can lead to increased heat transport as parallel heat transport along the island field lines contributes to heat loss from the plasma core to the edge. A more detailed description of MHD theory can be found in [Hopcraft 1993].

The COMPASS-D tokamak is equipped with a set of saddle coils and RMP bars [Hender et al 1992] which can be used to stimulate errors in toroidal and poloidal magnetic field coils. Error fields occur naturally due to alignment errors in the magnetic geometry of tokamaks. The COMPASS-D saddle coils are used to stimulate MHD instabilities in order to study their effects on the plasma and also to investigate methods of error field removal. Much of the work on COMPASS-D involves (m=2, n=1) modes resonant on the $q = 2$ surface.

The viscosity and inertia of a rotating plasma can suppress the formation of a magnetic island by stabilising the mode. Once a critical RMP field strength is exceeded, the island begins to form and at a threshold island width the mode becomes locked to the plasma frame of reference, this is called "mode penetration". At this point, the plasma rotation is halted by the island. The RMP field strength required for mode penetration increases with increasing density and thus there is a density threshold for locked mode formation. In typical COMPASS-D conditions this is at $n_e \approx 1 \times 10^{19} m^{-3}$. Further details of the RMP experiments can be found in [Hender et al 1992].

A number of phenomena are associated with mode-locking. These include changes of impurity ion rotation and a decrease in sawteeth activity in the soft x-ray signals which is due to a decrease in the core electron temperature. There is a significant degradation of the plasma stored energy and the particle confinement time is reduced [Hender et al 1992].

MHD perturbations are measured with arrays of Mirnov coils, poloidal arrays to measure the poloidal mode number and toroidal arrays to measure the toroidal mode number. The changing signals as a rotating mode passes a fixed detector are measured. Fourier analysis of the poloidal and toroidal arrays enables identification of the mode numbers. COMPASS-D has three poloidal arrays of 24 Mirnov coils at separate toroidal locations. At each location there are three pick-up coils which measure the toroidal, poloidal and radial fields.

6.1.1 Rotation Measurements During Mode-Locking

Edge rotation has been measured previously during mode-locking on COMPASS-(C and D) using B IV [Hender et al 1992, Bamford 1994]. Toroidal rotation

changes of $20 - 30km/s$ are seen at the plasma edge. The rotation frequency measured at the plasma edge is about half that measured by the Mirnov coils which measure the spin up of the mode after the mode is unlocked. One proposed explanation for this discrepancy is due to shear in the velocity profile outside the $q = 2$ surface [Hender et al 1992]. The magnetic measurements are within the $q = 2$ surface $\frac{r}{a} < 0.5$ and the B IV emission shell is at $\frac{r}{a} \approx 0.8$.

Cl XVI emission is from the plasma core (see Figure 6.3). Our measurement

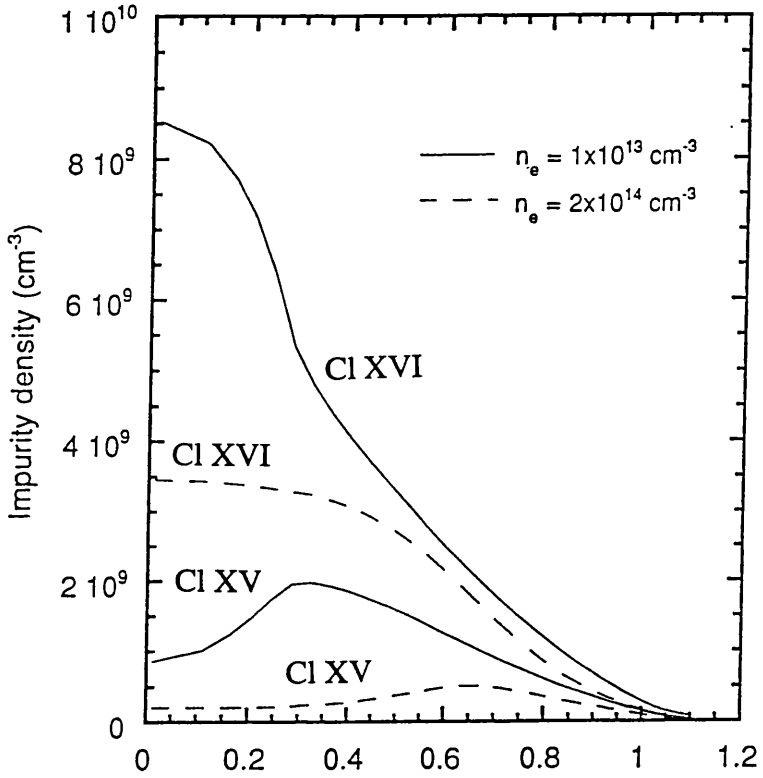

Figure 6.3: *Radial position of Cl XVI (top) and Cl XV (bottom) generated using the SANCO code, $T_e(0) = 1keV$. From [Peacock et al 1994].*

of Doppler shifts of the Cl XVI lines are therefore representative of the plasma core.

Since the density threshold for mode penetration is of the order $n_e \approx 1 \times 10^{19}m^{-3}$, photon statistics for the spectra are poor (see equation (3.1)) and the cross-correlation technique must be used to detect Doppler shifts of the spectral lines (see section 2.4.2). Results are shown from two pulses in Figures 6.4 and 6.5. The measured rotation changes are of the order of $20km/s$ which is similar in magnitude to that measured at the plasma edge from B IV, and

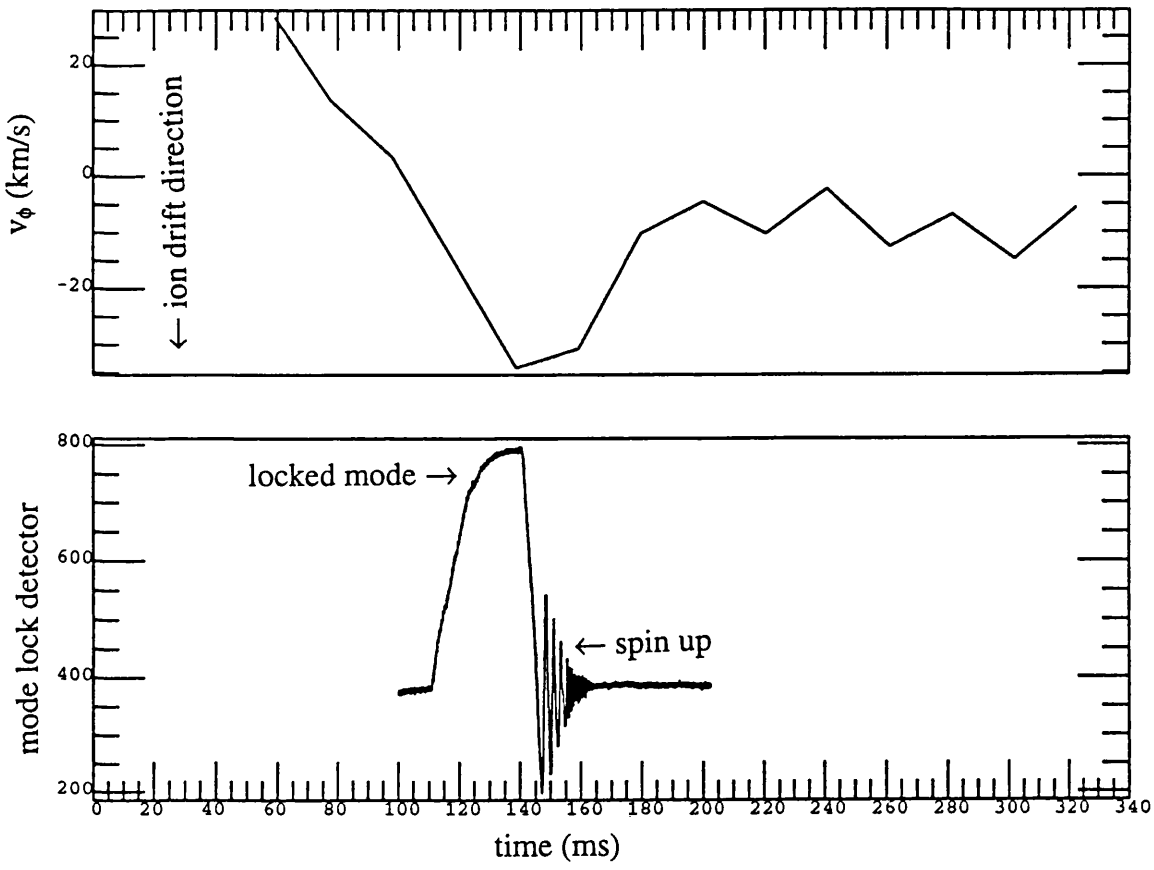

Figure 6.4: *Change of rotation during mode-locking. Also shown is the signal from the mode-lock detector. COMPASS-D #13595*

not greater as predicted [Hender et al 1992]. It is not clear how to define the errors in the measurement when using cross-correlation, but changes in plasma conditions do change the spectral shape and these changes affect the shape of the correlation function as shown in chapter 3. During these measurements the spectral shape was assumed to be the same for the duration of the discharge i.e. the same standard spectrum was used for each time point. There were no measurements available of the electron temperature for these pulses (photon statistics for the k/w line ratio were not sufficient for a fit). Given that changes of energy confinement are expected during mode-locking the errors could be of the order of the measured value (See Figure 3.8).

The plasma current in the two discharges shown are in opposite directions and the measured rotation direction is similarly reversed in the two pulses (one

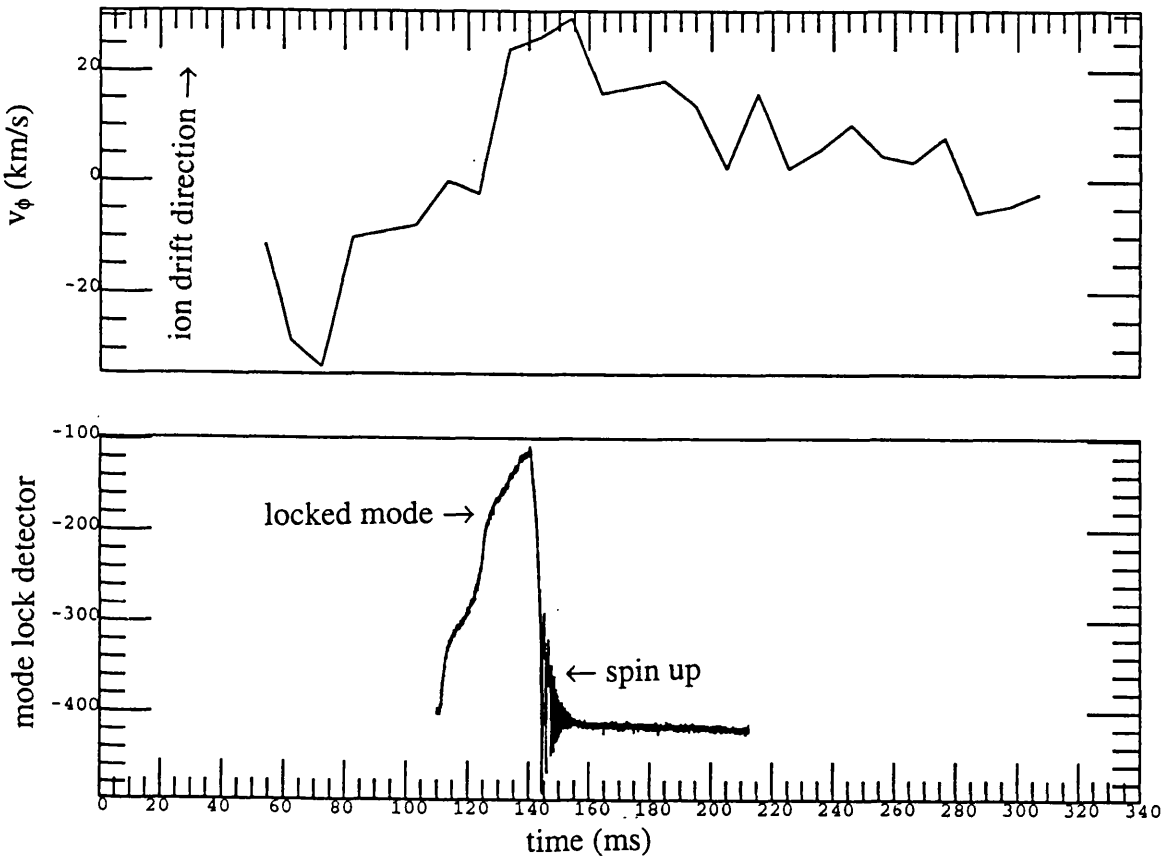

Figure 6.5: *Change of rotation during mode-locking with reversed current. Also shown is the signal from the mode-lock detector. COMPASS-D #13751*

is measured with a red shift, the other with a blue shift). In both cases the change in the plasma rotation during the mode-lock is in the ion drift direction, and then returns to the "original" value after the mode is switched off. In both cases there is a large rotation in the electron drift direction at the beginning of the discharge, it is not clear what this is due to.

6.2 H-Modes

During the H-mode there is observed to be a change in the radial electric field at the plasma edge [Field et al 1992]. It is not clear whether the change in the electric field is a cause or effect of the H-mode. These radial electric field changes necessarily imply a change in the fluid velocity or pressure gradient, see equation (6.3). Measurements of toroidal velocity, v_ϕ, on JET during beam heated H-

modes give $v_\phi > 50km/s$ at the plasma edge and $v_\phi > 200km/s$ closer to the core [Hawkes et al 1989]. There is also expected to be a change in the poloidal rotation, v_θ, at the plasma edge. At present there is some conflicting evidence between different tokamaks concerning the magnitude of the poloidal rotation and the width of the rotating sheath. The increase in the edge radial electric field is a key feature of many of the theories of the H-mode and measurement of the edge poloidal rotation is one of the key experimental measurements of it.

Ions can be lost close to the plasma edge as their guiding centre orbits take them beyond the separatrix for part of their motion, and there they are more likely to be lost from the plasma. A poloidal torque is therefore produced as those particles when just inside the separatrix will all be travelling in the same poloidal direction along their helical paths. This motion is damped by neoclassical viscous damping terms.

Changes of poloidal rotation at the L-H transition have been measured on DIII-D [Burrell et al 1989], ASDEX [Field et al 1992] and COMPASS-D [Carolan et al 1995], but no poloidal rotation has been measured on JET within the instrument resolution [Hawkes 1995]. However, all machines do report a change in the edge radial electric field E_r during the H-mode. The radial electric field is given by

$$E_r = -v_\theta B_\phi + v_\phi B_\theta + \frac{1}{Z_i n_i e} \nabla P_i, \tag{6.13}$$

which is obtained by rearranging equation (6.3). The E_r profile is flat across most of the plasma with a negative spike at the edge. In JET the main contribution to the negative spike is the steep edge pressure gradient, the contribution from v_ϕ is positive and there is no contribution from v_θ [Hawkes 1995]. In DIII-D, the impurity ion and bulk ion velocities have been measured separately (using He plasmas). Measurements of both yield the same E_r profile i.e. a negative spike at the plasma edge. For the bulk ions this is due to the negative pressure gradient, both v_ϕ and v_θ have a positive contribution. For the impurities, v_θ is in the opposite direction so has a negative contribution, but the pressure gradient contribution is decreased by a factor $\frac{Z_i}{Z_I}$ [Kim et al 1994]. The DIII-D results show a sharp increase of E_r at the L-H transition whereas the JET and ASDEX results show a more gradual change. The DIII-D measurement is multichord

with good spatial resolution ($< 1cm$) and shows that the rotating sheath is very narrow (a rotation change is seen in only one spatial channel). The ASDEX results are from a single fixed channel and show a slowly changing increase in rotation during the H-mode, this can either be due to an initially narrow rotating sheath slowly broadening during the H-mode or due to a wider sheath slowly increasing in velocity. The JET results presented in [Hawkes 1995] are multichord with a spatial resolution of $4cm$, but no rotation is seen in any of the channels. Recent improvements to the JET spectrometer with improved spatial resolution ($1cm$) still show no poloidal rotation changes [Hawkes et al 1995]. However, in both sets of results the change in E_r due to pressure gradient changes is gradual, slowly increasing during the H-mode.

In COMPASS-D toroidal and poloidal rotation at the plasma edge have been measured using B IV and C III [Carolan et al 1995]. Poloidal rotation changes of $> 10km/s$ have been measured and toroidal rotations changes of $20 - 30km/s$ have been observed. Both sets of measurements are well correlated with ELM behaviour. The change in E_r due to v_θ is estimated to be $\approx 20kV/m$ in the inward direction. It is assumed for these measurements that the pressure gradient contribution is small compared with the rotation contribution.

In all the above results (except for COMPASS-D), v_ϕ is mainly driven by momentum input from neutral beam injection. The COMPASS-D velocities are at least a factor of five smaller than the other velocities as a result. Toroidal rotation in COMPASS-D is driven by the various terms on the right hand side of equation (6.1) i.e. by changes in E_r, the pressure gradient and viscous and frictional forces. Here we present measurements of changes in v_ϕ at the plasma core during the H-mode and compare them with the edge results.

6.2.1 Rotation Measurements During H-Modes

The curved crystal spectrometer observes Cl XVI in the plasma core (Figure 6.3) and measurements have been made of the change in the core toroidal rotation during the L-H transition. Results are shown from ohmic L-modes, ELMy H-modes and ELM free H-modes and are compared with B IV measurements close to the edge. The two methods of measuring Doppler shifts, line fitting and cross

correlation are also compared.

We begin with ohmic L-mode plasmas, as already mentioned neoclassical theory predicts a small rotation of the impurity ions in the electron drift direction during ohmic plasmas. Figure 6.6 shows the measured rotation from Cl XVI in the plasma core and B IV at the edge. No significant change in v_ϕ is seen with either diagnostic during the discharge.

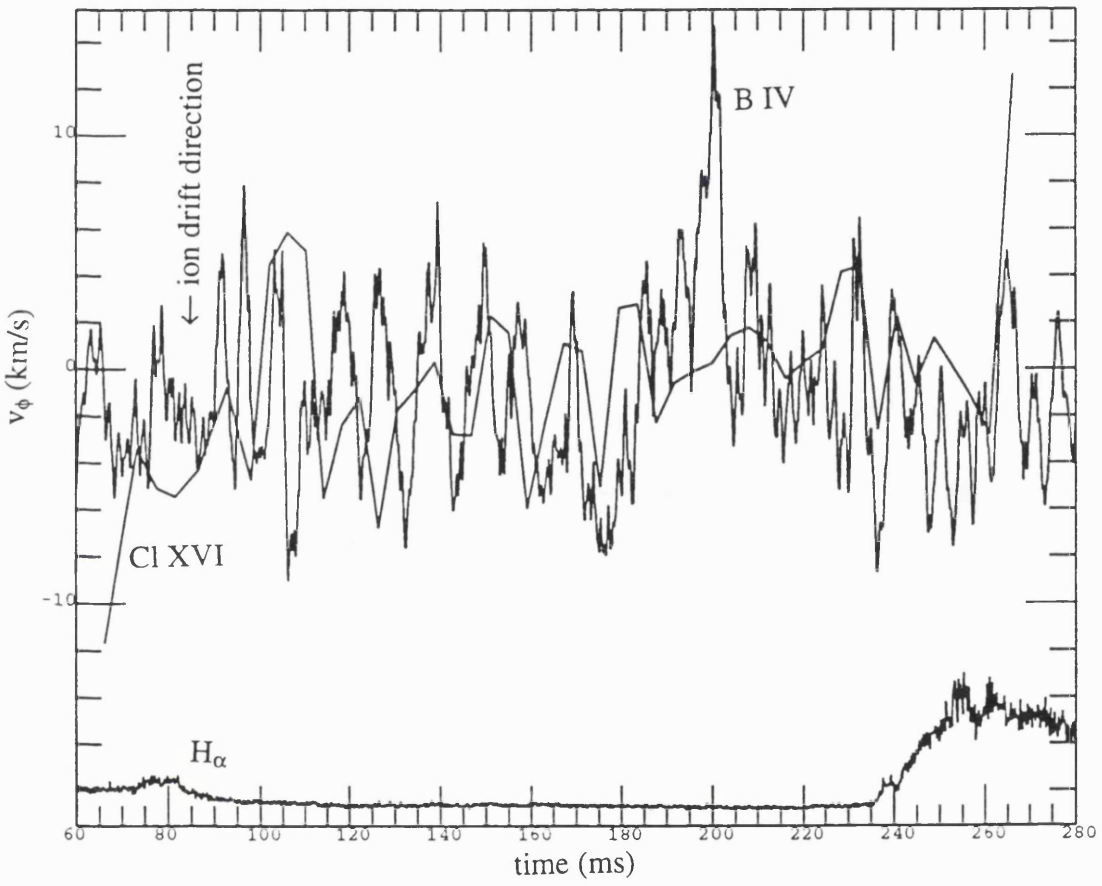

Figure 6.6: *Rotation measurement during an ohmic plasma showing the core value measured with Cl XVI and the edge value measured with B IV, the two values are shifted to a common zero. COMPASS-D #12479. The error bars of the measurements are shown by the fluctuations in the signals.*

COMPASS-D pulse #13583 is an ELMy H-mode discharge. During this pulse, shown in Figure 6.7, there is very little change ($< 5km/s$) of rotation. However, at the end of the pulse, the Cl XVI measurement shows a change of $\approx 7km/s$ in the electron drift direction which is not seen in the B IV measurement.

The Cl XVI line intensity reaches a peak at $\approx 200ms$ and then begins to decrease. At $240ms$ it has reduced to half of its peak value and then continues to decrease further.

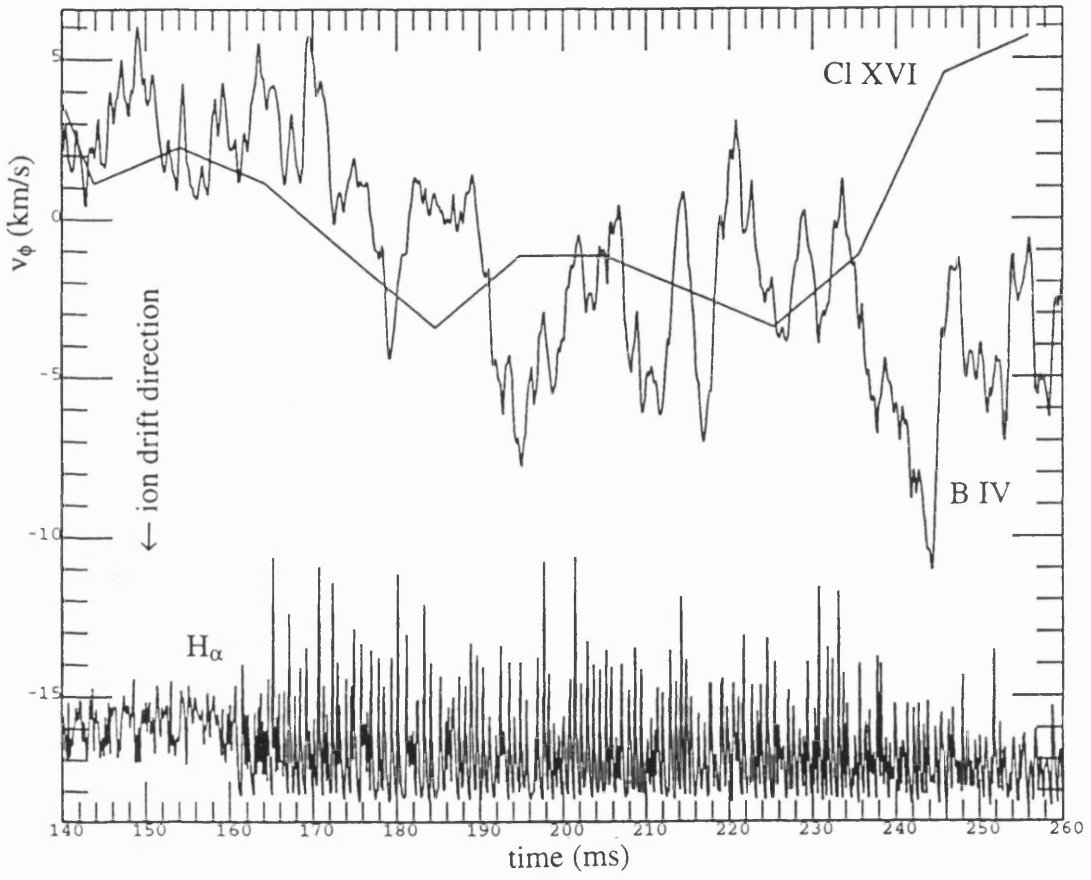

Figure 6.7: *Rotation measurement during an ELMy H-mode pulse. The change at $\approx 240ms$ is most likely to be due to a decrease in the line intensity and hence larger error bars. COMPASS-D #13583*

Figure 6.8 shows the change of rotation measured using Cl XVI at the plasma core together with the change measured with B IV at the plasma edge during an ELM free H-mode. The two values are shifted to a common value at $\approx 170ms$ just before the onset of the H-mode. Both diagnostics show a change of rotation in the ion drift direction at the beginning of the ELM free period, this then returns to its original value after the end of the H-mode. The rate of rotation increase is the same for the two measurements. For the pulse shown #12570, the core rotation and edge rotation show the same change, this tends to be true of

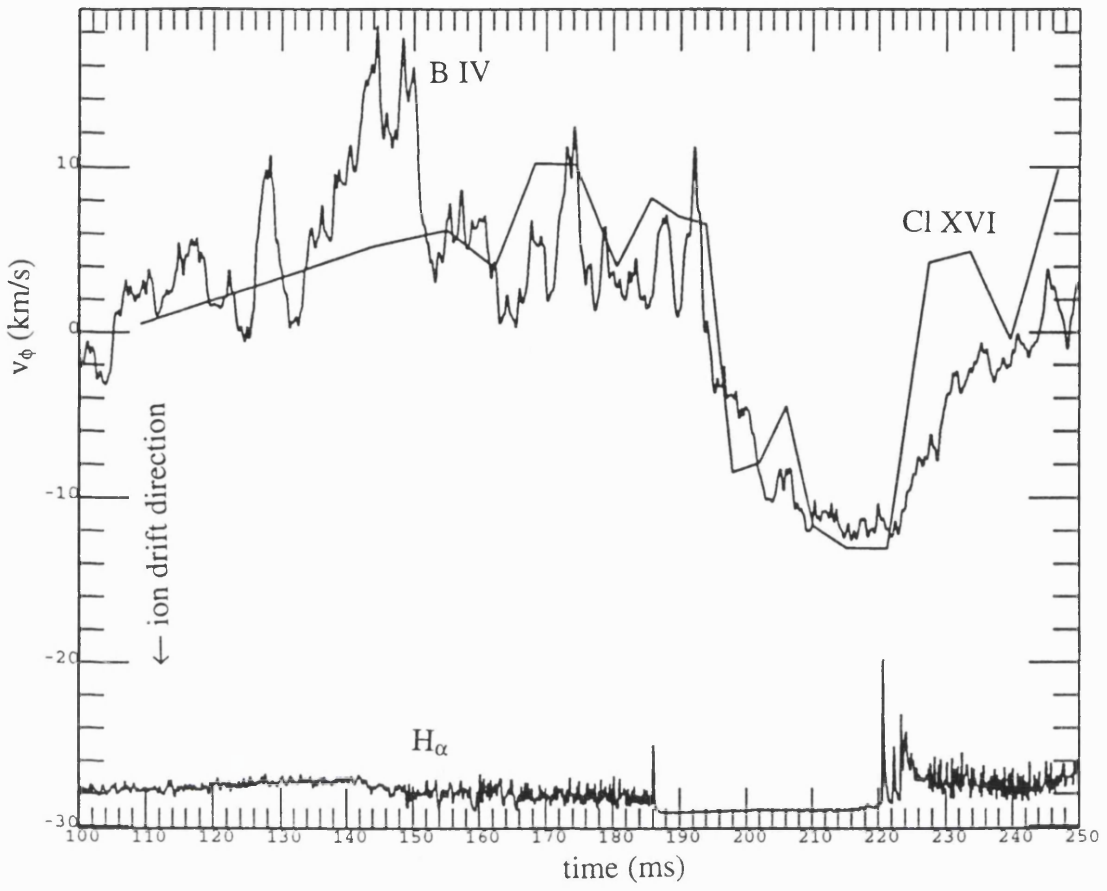

Figure 6.8: *Rotation measurement during an ELM free H-mode showing the core value measured with Cl XVI and the edge value measured with B IV, the two values are normalised at* $\approx 170ms$*, before the onset of the H-mode. COMPASS-D #12570.*

most pulses. Without any information on the absolute rotation values all that can be said is that the change of rotation across the plasma profile is roughly constant at the L-H transition, nothing can be said about the rotation profile itself. The rotation change is slow $< 1km/s/ms$ and in many cases it is even slower, it does not reach its maximum until the very end of the H-mode, and then quickly falls back to its zero value. The longer rise time of the plasma rotation and slower fall time indicate an increased momentum confinement time during the H-mode than during L-mode.

When the plasma current is reversed we see a change in the rotation direction, however, the rotation change is still in the ion drift direction. Figure 6.9 shows

such a plasma pulse. The data for this pulse was obtained from a spectrum of Al XIII using a PET crystal ($2d = 8.742\mathring{A}$), the Al was introduced into the plasma by laser ablation at $100ms$. An Al XIII spectrum is also shown in the figure. The change in rotation is again slow and there is very limited response to the ELMs.

The two techniques for Doppler shift analysis as discussed in chapters 2 and 3 can be compared. The rotation measured using a Voigt fit and using the cross-correlation technique for pulse #12570 is shown in Figure 6.10. Both methods give similar results, the rotation changes occurring together. For the cross-correlation it was assumed that the spectral shape remains constant throughout the plasma duration, in reality an electron temperature change of $\approx 200eV$ is measured during the discharge. This may explain the slight difference between the two techniques at the peak of the rotation ($210 - 220ms$). There are more data points for the cross-correlation technique as the summation of individual spectra is not required. Spectra are added together for the fitting routine to improve photon statistics.

6.3 Discussion

These results show that during ohmic L-mode plasmas there is no measurable change of rotation. Theory predicts a small rotation in the electron drift direction under such conditions which has been confirmed by experiments on the DITE tokamak [Hawkes and Peacock 1985]. These experiments cannot confirm this as there is no reference wavelength. There are no rotation changes under such conditions. During ELM free H-modes there is a large change of rotation $\approx 20km/s$ in the ion drift direction at the onset of the H-mode. The rotation then returns to its original value after the end of the H-mode. The rotation change at the L-H transition is always in the ion drift direction irrespective of the direction of the plasma current. This is true of both H-mode rotation and mode-locking.

The driving terms for the rotation can be found from analysis of equation (6.1). There is no neutral beam injection or any other input of momentum into the plasma. We assume that in the plasma core there is no significant change in

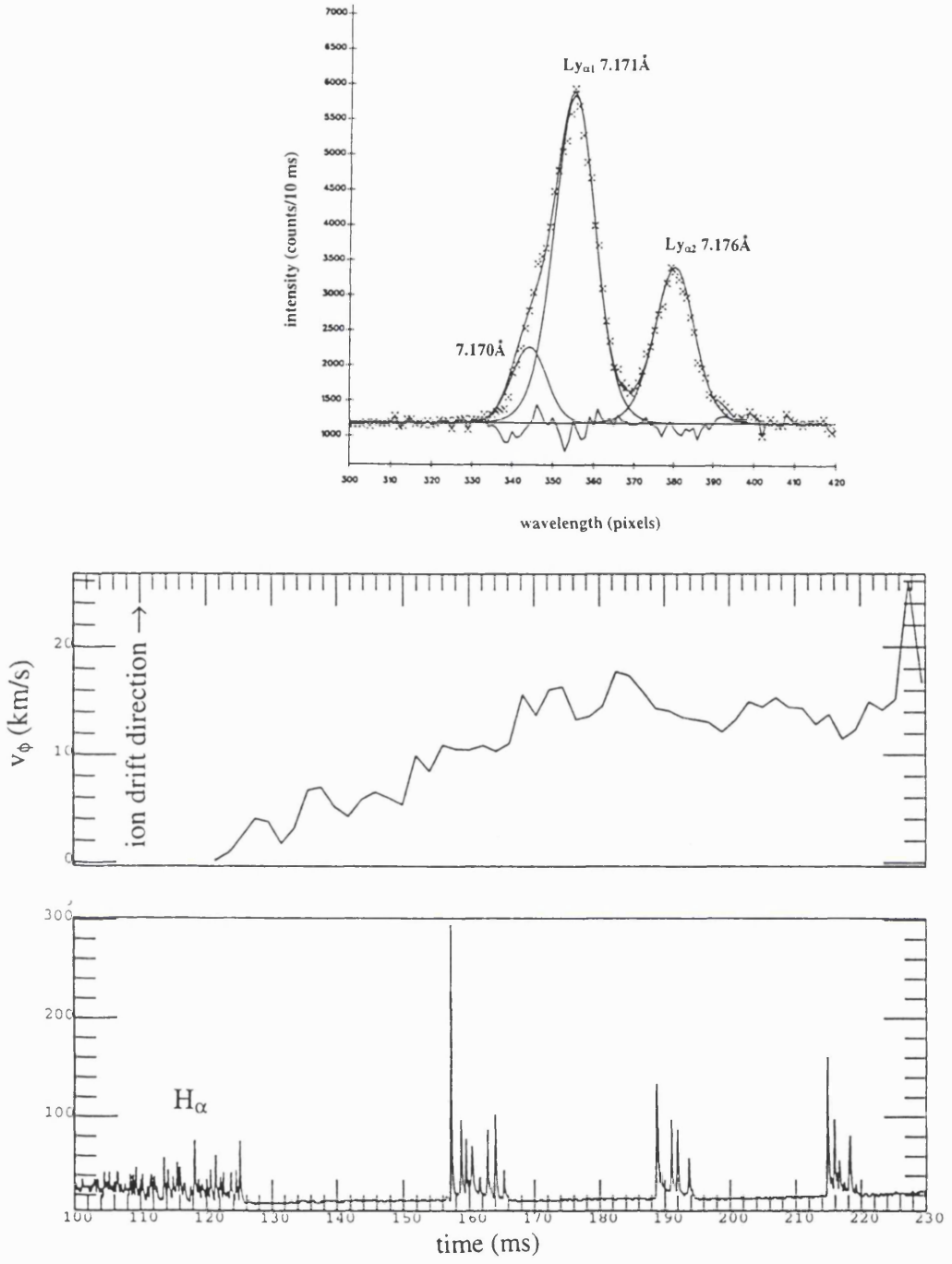

Figure 6.9: *Rotation measurement during an ELM free H-mode with reversed current showing the core value measured with Al XIII introduced into the plasma by laser ablation at* 100*ms. Also shown is an Al XIII spectrum obtained using a PET crystal. COMPASS-D #16012.*

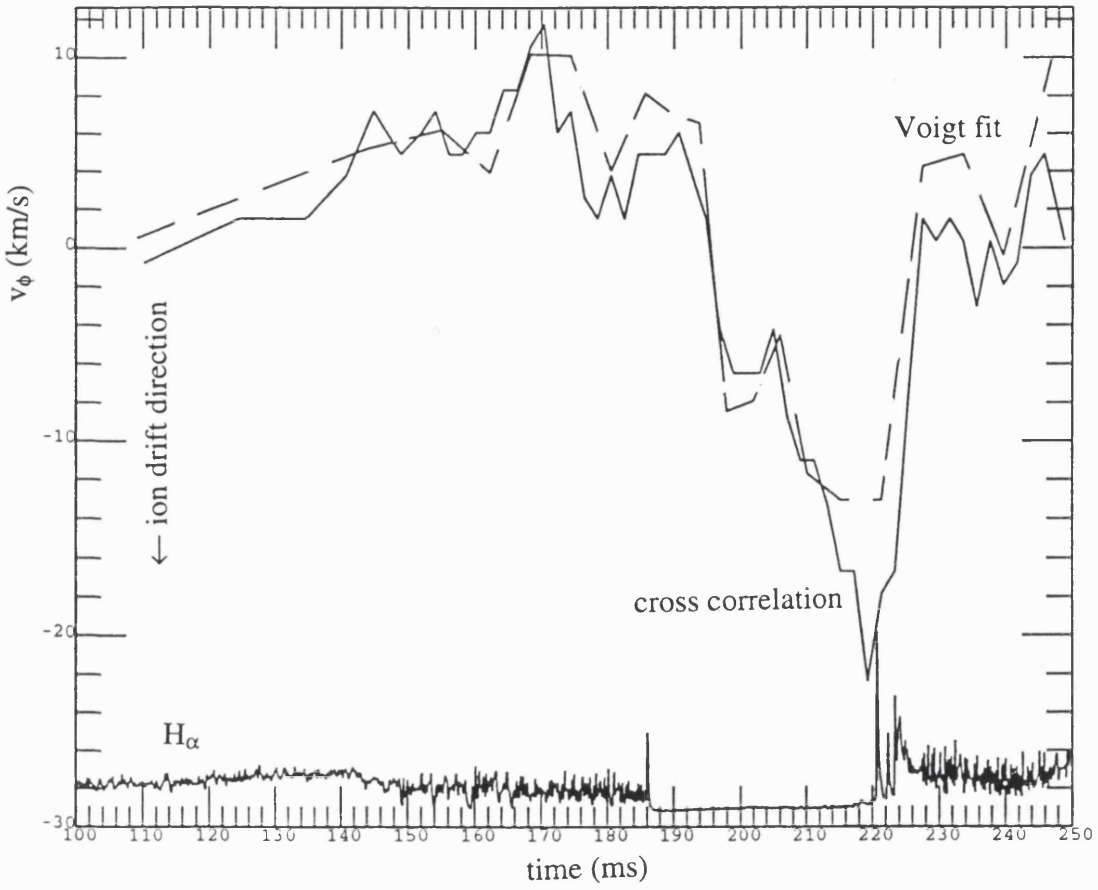

Figure 6.10: *Comparison of Voigt fitting with cross-correlation for Doppler shifts in a high density H-mode plasma. The two methods show similar results thus giving confidence to the cross-correlation method. COMPASS-D #12570.*

the radial electric field, only the edge changes at the L-H transition. The remaining terms are the pressure gradient terms and the viscous and frictional forces. In the absence of measurements of the pressure gradients, some assumptions as to how these change during the H-mode can be made, and then the effects on the rotation can be calculated. The plasma viscosity required for the measured changes of core rotation if the driving force is assumed to be the change of electric field at the plasma edge can also be estimated.

6.3.1 Velocity Changes Due to Pressure Gradients

The change of rotation due to pressure gradient changes can be estimated from neoclassical theory [Brau et al 1983, Suckewer et al 1981];

$$v_\phi = -\frac{T_i}{ZB_\theta}\left[\frac{1}{n_i}\frac{\partial n_i}{\partial r} + \frac{k}{T_i}\frac{\partial T_i}{\partial r} + \frac{Z}{T_i}\frac{\partial \phi}{\partial r}\right], \tag{6.14}$$

where k depends on the collisionality of the ions, $k = -0.17$ in the banana regime, 1.5 in the plateau regime and 2.7 in the Pfirsch - Schlüter regime. In this equation v_ϕ is in m/s, T_i is in eV, B_θ is the poloidal field in T and n_i is in m^{-3}. $\frac{\partial \phi}{\partial r}$ is the radial electric field in V/m.

We shall assume temperature and density gradients as given by equations (1.3) and (1.4) before the H-mode and that these flatten off at the plasma centre during the H-mode (in reality this may not be true, but we can obtain an upper limit to the velocity change if we assume that the profiles do flatten at the centre). We shall also assume that the bulk ions are in the plateau regime, the impurity ions are in the Pfirsh-Schlüter regime and that the electric field is constant at the plasma centre throughout the L-H transition. The Cl XVI shell fills the central 3cm of the plasma (ie $\frac{r}{a} = 0 - 0.2$). For this region, for the bulk ions we can assume the following values; $\frac{1}{T_i}\frac{\partial T_i}{\partial r} = 3m^{-1}$ and $\frac{1}{n_i}\frac{\partial n_i}{\partial r} = 2m^{-1}$, $B_\theta \approx 0.1T$, $n_i = 1 \times 10^{20} m^{-3}$, $T_i = 300eV$ and $Z_{eff} = 2$ just before the onset of the H-mode. If the gradients flatten to zero at the onset of the H-mode, then all the terms on the right hand side of equation (6.14) go to zero, so the velocity change is minus the L-mode estimate, giving $\approx +10km/s$, which is a change in the ion drift direction. This is equivalent to a radial electric field change of $1kV/m$.

For Cl XVI ions with $Z = 15$, we can assume that $\frac{1}{T_i}\frac{\partial T_i}{\partial r}$ is the same as for the bulk ions. For $\frac{1}{n_i}\frac{\partial n_i}{\partial r}$ we assume $\frac{n_I}{n_i} = 5 \times 10^{-5}$ and that the profile is as in Figure 6.3. This gives $\frac{1}{n_i}\frac{\partial n_i}{\partial r} = 0.5m^{-1}$. Keeping the other values the same gives a velocity change of $\approx +2km/s$ as the profiles flatten (without the effects of any electric field changes). This is equivalent to an electric field change of $0.2kV/m$. An additional electric field of change of $\approx 2kV/m$ would be required for a velocity change of $20km/s$.

The predicted velocity change is in the right direction to explain our results, and the B_θ dependence would explain the change of direction with change of

plasma current direction. The measured impurity velocity changes cannot be explained by the changes in the impurity pressure gradient alone; an additional electric field change would also be required. There are no other core electric field data available to either confirm or dismiss the above predictions. The electric field associated with the pressure gradient change of the core ions (equivalent to $1kV/m$) is smaller than that required to increase the velocity change of the impurity ions from $2km/s$ to $20km/s$. In the limit of flat profiles during the H-mode, the measured velocity changes could be interpreted partly in terms of the bulk ion pressure gradient. In reality where the gradients are probably not completely flat we can conclude that the pressure gradient effects contribute to the measured rotation change but are not necessarily the whole story.

6.3.2 Velocity Changes Due to Viscous Forces

Another possibility is to assume that the core rotation is driven by the plasma viscosity. For example an electric field change at the plasma edge drives the edge rotation, the rotation then moves inwards to the plasma core due to the plasma viscosity which drives the core rotation. We shall use the model of a rotary viscometer e.g. a Searle meter [Massey 1975].

Two concentric cylinders separated by a fluid can be used to measure the viscosity of the fluid. If the outer cylinder rotates, the torque on the inner cylinder can be measured and hence the viscosity of the fluid calculated. If the outer cylinder rotates with angular velocity Ω and μ is the coefficient of viscosity, then the torque, T, applied to the inner cylinder is

$$T = \frac{4\pi h a^2 b^2}{a^2 - b^2}\mu\Omega = k\mu\Omega, \tag{6.15}$$

where a is the radius of the outer cylinder, b is the radius of the inner cylinder and h is the height of the inner cylinder in contact with the fluid.

If the viscous force is the only force driving the inner cylinder, we can say

$$T = mb^2\frac{d\omega}{dt}, \tag{6.16}$$

where m is the mass of the inner cylinder and ω is its angular velocity. Equating equations (6.15) and (6.16) we obtain

$$\mu = \frac{mb^2}{k\Omega}\frac{d\omega}{dt}. \tag{6.17}$$

Substituting COMPASS-D parameters into equation (6.17), considering the central 5 cm of the plasma as the inner cylinder, $k = 0.8m^3$ ($a = 0.727m$, $b = 0.607m$, $h = 0.05m$). $m = n_i A_i m_p \times vol$, $vol = 0.03m^{-3}$. With $n_e = 1 \times 10^{20} m^{-3}$ and $\Omega = 4500 rad/s$ ($20 km/s$) at the plasma edge as measured by the omega spectrometer and $\frac{d\omega}{dt} = 5.7 \times 10^5 rad/s^2$ ($1 km/s/ms$) for the plasma core as measured by the curved crystal spectrometer (see Figure 6.8). If we assume that, at the core, the whole plasma (impurity and bulk ions) rotates as a single body, we obtain $\mu = 3 \times 10^{-7} Pa\ s$.

This model is only really appropriate for laminar flow of liquids and is for cylindrical geometry rather than toroidal geometry. However during the H-mode turbulence is suppressed and the plasma transport will be closer to neoclassical predictions. For an order of magnitude estimation, the model may be acceptable.

The plasma viscosity can also be calculated from

$$\eta = nmD, \tag{6.18}$$

where η is the plasma viscosity and D is the diffusion coefficient. The classical perpendicular ion diffusion coefficient is given by [Gross 1984];

$$D_\perp^i = 4.67 \times 10^{-23} \frac{Z^2 A^{\frac{3}{2}} n_i ln\Lambda}{B^2 T_i^{\frac{1}{2}}}\ m^2 s^{-1}, \tag{6.19}$$

where n_i is the ion density in m^{-3}, B is the toroidal field in T and T_i is the ion temperature in keV. Using the neoclassical corrections (plateau regime) as in chapter 4 and using $T_i = 300eV$ and $ln\Lambda = 16$ and the other values as above, we obtain $D_\perp \approx 3m^2 s^{-1}$. This gives $\eta_\perp = 1 \times 10^{-6} Pa\ s$ for the neoclassical coefficient of viscosity. We thus obtain

$$\frac{\eta_\perp}{\mu} \approx 3. \tag{6.20}$$

We would expect the neoclassical calculation to be a lower limit to the plasma viscosity and our model to give a higher value as the diffusion coefficient is increased due to anomalous transport. The neoclassical value given is for the total perpendicular viscosity. We need only consider those components which affect the toroidal velocity as a result of momentum transfer in the radial direction: this will reduce the effective coefficient of viscosity by a third. Additionally radial changes of $D_\perp$ have not been taken into account.

The value taken for Ω in equation (6.17) assumes that the core only starts rotating after the edge has reached its maximum velocity. This is not the case as the edge and core appear to accelerate together. The time resolution of the curved crystal spectrometer is not sufficient to resolve any delay in the core acceleration. If we assume a delay of $1ms$ (rather than the previous assumption of $20ms$), then the value of Ω will have to be reduced to $\approx 225rad/s$ $(1km/s)$, thus giving a value of $\mu = 6 \times 10^{-6} PaS$. If the delay is less than this, the viscosity will be higher. Better time resolution and improved photon statistics would be required to measure the time delay.

If the model viscosity (μ) is larger than the predicted neoclassical value (η), it would imply that the viscosity is anomalous as has been found on other tokamaks [Brau et al 1983, Hawkes and Peacock 1985]. Taking into account the above considerations, the model viscosity is larger than the neoclassical value. The simplicity of the model used and the lack of faster time resolution do not allow an estimation of the degree of the departure from the neoclassical prediction. However, it has been shown that in the limit of assuming that the entire core rotation is driven by the edge rotation after reaching its maximum value, the required viscosity is similar in magnitude to the neoclassical prediction. The effect of anomalous viscosity is then to reduce the delay of changes in the core rotation in response to changes at the edge. As such the plasma viscosity is an important driving term of the core rotation.

6.4 Summary

Core toroidal rotation has been measured using Doppler spectroscopy of Cl XVI lines in both H-mode and mode-locking conditions. During high density H-modes, Doppler shifts are found by fitting Voigt functions to the data, but during low density mode-locking experiments cross-correlation must be used. The two methods are shown to be in good agreement during high density discharges. In both cases changes in Doppler shifts corresponding to velocity changes of $\approx 20km/s$ are seen in the ion drift direction at the onset of the H-mode / mode-lock.

The core rotation does not change quickly at the L-H transition, the rise is slow. The return to the zero value at the end of the H-mode is faster. The core rotation is not affected by ELMs: faster time resolution would be required for a more detailed study of ELM behaviour.

Calculations show that changes in the pressure gradient alone are not sufficient to produce the measured rotation changes in the core. A very simple model of a viscometer shows that viscosity could be a significant term in the force balance equation.

Chapter 7

Conclusions

A high resolution Johann spectrometer has been used to observe the spectrum of He- like Cl and its satellites in the range $4.4 - 4.5\mathring{A}$ on the COMPASS-D tokamak. The diagnostic potential of the spectrometer in this wavelength range includes Doppler measurements from line profile analysis, and interpretation of line intensities and ratios in terms of population processes and plasma heat and particle transport. The spectral resolution is complemented by good temporal resolution allowing a large set of diagnostic information on a fast time scale.

The relatively low electron and ion temperatures during ohmic operation of COMPASS-D are ideally diagnosed with Cl XVI line emission: the satellite lines are well resolved and relatively intense. Higher temperature tokamaks would require a heavier impurity to be able to make diagnostic use of the dielectronic satellite line ratios.

The main technique used is to fit the spectral lines with Voigt profiles and then use the results of the fit to obtain the relevant plasma parameters. In cases where photon statistics are not sufficient for line fitting a cross-correlation technique has been used for spectral analysis.

7.1 Summary of Main Results

i) Simultaneous measurements of T_e and T_i and differences between them in different plasma conditions are interpreted in terms of neoclassical and anomalous transport coefficients. The different coefficients can be used to differentiate

between the plasma conditions.

ii) Measurement of the $\frac{q}{w}$ (Li- like / He- like) line ratio at high temperature ($T_e > 800eV$) shows that the plasma is close to coronal equilibrium conditions. In these conditions, this line ratio is used to obtain the impurity ion diffusion coefficient D. Good agreement is found between this technique and measurements using the decay time of spectral lines following laser ablation. At lower temperatures the $\frac{q}{w}$ ratio indicates an increase in the Li- like density relative to the He- like density.

iii) Measurements of the He- like ratios G and R also indicate that at high temperature the plasma is close to coronal conditions (the R ratio however is $\approx 20\%$ below the coronal prediction) and that there are departures from coronal equilibrium at lower temperatures. It is thought unlikely for recombination from the H- like state to be responsible for the non-coronal ratios at these lower temperatures. Departures from coronal balance are more likely to be related to increases in the Li- like density and hence an increase in the triplet levels due to inner shell ionisation.

iv) Absolute intensity measurements of the continuum and line radiation have been made. Modelling of the continuum shows that free-free radiation dominates over free-bound radiation if only the main low Z plasma impurities are considered. However, during neon gas puffing experiments it was found that the increase in the continuum level can only be modelled by a large increase in the free-bound contribution.

v) Measurements of the line intensities show that in L-mode and ELMy H-mode plasmas the line intensity increases as expected with the electron density and temperature. During ELM free H-mode discharges the line intensity increases faster than n_e^2 despite a reduction in T_e. This leads to speculation on impurity accumulation.

vi) Measurements of the core toroidal rotation during RMP experiments show that there is a change of rotation of $\approx 20km/s$ in the ion drift direction at the onset of mode-locking. The rotation then returns to its "zero" value after the mode is removed.

vii) The core toroidal rotation is shown to increase slowly in the ion drift direction

at the onset of an ELM free H-mode. The rotation reaches a peak of $\approx 20km/s$ and then returns to the original value after the end of the H-mode. No changes of rotation are seen during ELMy H-modes. The measured core rotation changes are in good agreement with edge measurements using B IV.

It has been shown that the combination of the spectral resolution with the atomic physics of the He- like system can be used as a successful plasma diagnostic to give information on heat and particle transport, impurity concentration and plasma rotation. In many cases the interpretation of these results leads to departure from neoclassical theory and coronal balance conditions. Coronal balance is usually assumed for the centre of tokamaks; it has been shown here that this is only true on COMPASS-D with central electron temperatures of more than $\approx 800eV$.

The study of ohmic H-mode plasmas on COMPASS-D has not shown any sudden changes of either central electron or ion temperature at the L-H transition, this could be due to limits of the instrument resolution if the changes are small. Rotation changes at the plasma core during ELM free H-modes are slow. The edge diagnostics measure a reduction of the rotation during ELMs, no such reduction is observed at the core. Increased photon statistics allowing faster time resolution is required to investigate this further. There is some evidence of impurity accumulation during ELM free H-modes.

The satellite line intensity and wavelength data of [Vainshtein and Safronova 1978, Vainshtein and Safronova 1980] have been used for the line fitting. In general good agreement with the data is found. However the wavelength of the d_{13} line has been fitted at $4.4523\mathring{A}$ rather than the quoted value of $4.4518\mathring{A}$.

Previous work on Ti XXI has shown that there is a threshold temperature of $1200eV$ above which the He- like line ratios follow coronal calculations and below which there is an enhanced G ratio related to the Li- like density [Bitter et al 1985]. In this work it has been shown that there is a similar threshold temperature for Cl XVI at $\approx 800eV$. Previous work on Cl XVI [Coffey 1993, Källne et al 1983], has not investigated electron temperatures below $800eV$.

7.2 Recommendations for Future Work

There is some scope for improved spectrometer performance. The spectral resolution is limited by the crystal diffraction width and the detector spatial resolution, but other factors such as the Johann aberrations still have room for improvement. The CCD array at present is capable of sub millisecond temporal resolution, however photon statistics have not been sufficient to run any faster than $2ms$. Photon statistics can be improved by the introduction of impurities into the plasma. A similar study of Ar XVII following Ar gas puffing would allow similar measurements but on a faster time scale.

The results presented in this thesis are derived from the fitting of spectral lines. Twenty five Voigt fits have been used in general for spectral line fitting, and for Doppler analysis a line blend has been fitted with three Voigt profiles. The accuracy of the fitting is reduced the greater the number of free parameters. It is thought that more accurate Doppler measurements on COMPASS-D could be achieved by observation of a singlet line. This would be particularly useful for study of H-modes and ELM behaviour.

A diagnostic neutral beam is due to be installed on COMPASS-D shortly which will allow visible charge exchange spectroscopy of the whole plasma profile thus giving profile information on the ion temperature and toroidal and poloidal rotation. This is a useful alternative to the previous suggestion as viewing of a different set of spectral lines will mean the loss of much diagnostic information.

There appears to be a lack of data available on various aspects of the atomic physics related to this work. There is no wavelength or intensity data available for dielectronic satellites of Cl XVI, $n \geq 4$. The large departures from coronal equilibrium of the G and R ratios at low temperatures still requires investigation. A number of possible mechanisms have been suggested [Bitter et al 1985], but the problem still remains unresolved.

Appendix A

Symbol List

a	minor radius (horizontal)
a_0	Bohr radius $= 5.292 \times 10^{-11} m$
A_a	autoionisation rate
A_i	ion mass
A_r	radiative decay rate
$A(\Delta\lambda)$	cross-correlation function
b	minor radius (vertical)
B	magnetic field vector
B_ϕ	toroidal field
$C(T_e)$	excitation rate
d	crystal lattice spacing
$D_\perp$	perpendicular diffusion coefficient
E	electric field vector
E_r	radial electric field
E_λ	plasma emissivity
g	statistical weight
H	crystal height
I_p	plasma current
J	current density
n	principle quantum number
n_e, n_i, n_I	electron density, bulk ion density, impurity ion density
n_{He}	He- like ground state density

P_{ei}	electron -ion power transfer
P_0	crystal peak reflectivity
q	safety factor
q_s	satellite intensity factor
$Q(T)$	partition function
S	ionisation rate
R	Rowland circle diameter
R	major radius
R_c	crystal integrated reflectivity
T_e, T_i	electron temperature, ion temperature
W	crystal width
v_{th}	thermal velocity
v_θ, v_ϕ	poloidal velocity, toroidal velocity
V	convective velocity
Z	ion charge
Z_{eff}	effective charge of plasma
α	recombination rate
ϵ	inverse aspect ratio
θ_B	Bragg angle
λ	wavelength
$\ln \Lambda$	Coulomb logarithm
μ	viscosity
η	neoclassical viscosity
σ	charge density
τ_E	energy confinement time
τ_{ie}	electron-ion equipartition time
τ_{imp}	impurity confinement time
χ	thermal conductivity
χ_H	ionisation potential of hydrogen

List of Publications

X-Ray Spectroscopic Study of Heat and Particle Transport in the COMPASS-D Tokamak IM Melnick, R Barnsley, IH Coffey, MG O Mullane, NJ Peacock, 21^{st} IOP Conference on Plasma Physics, Brighton (1994)

X-Ray Spectroscopic Studies of Particle Transport in the COMPASS-D Tokamak NJ Peacock, R Barnsley, IH Coffey, SJ Fielding, IM Melnick, MG O Mullane, A Patel, MA Singleton, M Valovic, 21^{st} EPS on Controlled Fusion and Plasma Physics, Montpellier, 18B 134 (1994)

COMPASS-D Ion Temperature Measurements Using the Curved Crystal Spectrometer IM Melnick, R Barnsley, NJ Peacock, DTI Milestone Report F/PL/B3.2C/CD/D1/IMM/94 (1994)

Core Rotation Measurements in Low Density Mode-Locking Plasmas on COMPASS-D IM Melnick, R Barnsley, PG Carolan, NJ Peacock, 22^{nd} IOP Conference on Plasma Physics, Oxford (1995)

Ion Transport and Impurity Accumulation during Ohmic H-Modes in the COMPASS-D Tokamak NJ Peacock, MA Singleton, R Barnsley, SJ Fielding, NC Hawkes, IM Melnick, MG O Mullane, A Patel, M Valovic, 22^{nd} EPS on Controlled Fusion and Plasma Physics, Bournemouth, (1995)

Cl XV and Cl XVI in the JET and COMPASS-D Tokamaks IH Coffey, R Barnsley, FP Keenan, IM Melnick, P McGinnity, MG O Mullane, NJ Peacock, 11^{th} International Colloquium of UV and X-Ray Spectroscopy of Astrophysical and Laboratory Plasmas, Nagoya, Universal Academy Press (1995)

Bibliography

[Abbey et al 1992] AF Abbey, R Barnsley, J Dunn, S Lea, NJ Peacock, *UV and X-Ray Spectroscopy of Laboratory and Astrophysical Plasmas* Cambridge University Press (ed E Silver and S Kahn) pp533 (1992)

[Artsimovich 1972] LA Artsimovich, Nuclear Fusion **12** 215 (1972)

[Badnell et al 1993] NR Badnell, WJ Dickson, HP Summers, DC Griffin, J Lang, Astrophys. J. Letters, **407** L91 (1993)

[Bamford 1994] RA Bamford, *Spectroscopic Measurements of Impurity Ion Drift Velocities in the COMPASS Tokamak* PhD Thesis, University of Essex (1994)

[Barnsley 1993] R Barnsley, *X-Ray Spectroscopic Diagnostics of Magnetically Confined Plasmas, Instrumentation and Techniques* PhD Thesis, University of Leicester (1993)

[Behringer 1987] JET Report JET-R(87)08 (1987)

[Bely-Dubau et al 1982a] F Bely-Dubau, J Dubau, P Faucher, AH Gabriel, Mon. Not. R. Astron. Soc. **198** 239 (1982)

[Bely-Dubau et al 1982b] F Bely-Dubau, P Faucher, L Steenman-Clark, M Bitter, S Von Goeler, KW Hill, C Camhy-Val, J Dubau, Physical Review A **26** 6 3459 (1982)

[Bitter et al 1985] M Bitter, KW Hill, M Zarnstorf, S Von Goeler, R Hulse, LC Johnson, NR Sauthoff, S Sesnic, KM Young, M Tavernier, F Bely-Dubau, P Faucher, M Cornille, J Dubau, Physical Review A **32** 5 3011 (1985)

[Book 1987] DL Book, *NRL Plasma Formulary* Naval research Laboratory, Washington DC 20375 (1987)

[Brau et al 1983] K Brau, M Bitter, RJ Goldston, D Manos, K McGuire, S Suckewer, Nuclear Fusion **23** 12 1643 (1983)

[Burek 1976] A Burek, Space Sci. Instrum. **2** 53 (1976)

[Burrell et al 1989] KH Burrell et al, Plasma Physics and Controlled Fusion **31** 10 1649 (1989)

[Caciuffo et al 1990] R Caciuffo, C Ferrero, O Francescangeli, S Melone, Review of Scientific Instruments **61** 11 3467 (1990)

[Carolan 1994] PG Carolan Private communication (1994)

[Carolan et al 1995] PG Carolan, RC O'Connel, NJ Conway, RA Bamford, J Hugill, IM Melnick 22^{nd} EPS on Controlled Fusion and Plasma Physics, Bournemouth (1995)

[Chen 1984] FF Chen, *Introduction to Plasma Physics and Controlled Fusion* Vol 1 Plenum Press (1984)

[Coffey 1993] IH Coffey, *Studies of K and L Shell Spectra of Impurity Ions in Tokamak Plasmas* PhD Thesis Queens University Belfast (1993)

[Compass-D Brochure 1994] Available from UKAEA Government Division, Fusion Directorate, Culham, Oxfordshire, OX14 3DB

[Cordey et al 1995] JG Cordey, DG Muir, SV Neadachin, VV Parail, E Springmann, A Taroni, Nuclear Fusion **35** 1 101 (1995)

[DeMichelis and Mattioli 1981] C De Michelis, M Mattioli, Nuclear Fusion **21** 6 677 (1981)

[DeSerio et al 1981] R DeSerio, HG Berry, RL Brooks, H Hardis, AE Livingstone, S Hinterlong, Physical Review A **24** 1872 (1981)

[Dickson 1993] WJ Dickson, *Metastable Resolved Collisional Radiative Modelling of Spectral Emission from Thermal Plasmas* PhD Thesis University of Strathclyde (1993)

[Doschek et al 1979] GA Doschek, RW Kreplin, U Feldman, The Astrophysical Journal **233** L157 (1979)

[Drake 1988] GW Drake, Can. J. Phys. **66** 586 (1988)

[Dunn 1990] J Dunn *High Resolution X-Ray Spectroscopy of Laboratory Plasmas* PhD Thesis University of Leicester (1990)

[Field et al 1992] AR Field, G Fussman, JV Hofmann and the ASDEX Team, Nuclear Fusion **32** 7 1191 (1992)

[Fielding et al 1994] SJ Fielding et al 21^{st} EPS on Controlled Fusion and Plasma Physics, Montpellier, **18B** 1 322 (1994)

[Foord et al 1982] ME Foord, ES Marmar, JL Terry, Review of Scientific Instruments **53** 1407 (1982)

[Fraser and Suzuki 1970] RDB Fraser, E Suzuki *Biological Applications* chapt 5 from *Spectral Analysis* ed JA Blacburn, Marcel Dekker Inc. (1970)

[Fussman 1992] G Fussman, 11^{th} European Tokamak Program Workshop, Noordwijk, Dec (1992)

[Gabriel 1972] AH Gabriel, Mon. Not. R. Astrom. Soc. **160** 99 (1972)

[Gabriel et al 1981] AH Gabriel, JL Culhane, LW Acton, E Antonucci, RD Bentley, C Jordan, LW Leibacher, AN Parmar, KJH Phillips, CG Rapley, CJ Wolfson, KT Strong, Adv. Space Res **1** 267 (1981)

[Gammow 1938] G Gammow, Physical Review **53** 59 (1938)

[Griem 1964] HR Griem, *Plasma Spectroscopy* McGraw Hill (1964)

[Grineva et al 1973] YI Grineva, VI Karov, VV Korneev, VV Krustov, SL Mandelstam, LA Vainshtein, BN Vasilysev, JA Zhitnik, Sol. Phys. **29** 441 (1973)

[Groebner 1993] RJ Groebner, Physics of Fluids B **5** 7 2343 (1993)

[Gross 1984] A Gross, *Fusion Energy* Wiley 1984

[Hall 1980] R Hall *A Quantative Description of Bragg Analysers* PhD Thesis University of Leicester (1980)

[Hawkes and Peacock 1985] NC Hawkes, NJ Peacock, Nuclear Fusion **25** 8 971 (1985)

[Hawkes et al 1989] N Hawkes, Z Wang, R Barnsley, K Behringer, S Cohen, B Denne, A Edwards, R Giannella, R Gill, G Magyar, D Pasini, NJ Peacock, V Schumacher, C Vieider, D Zasche, 16^{th} EPS on Controlled Fusion and Plasma Physics, Venice, **13B** 1 79 (1989)

[Hawkes 1995] NC Hawkes *Experimental Studies of Ion Pressure, Impurity Flows and their Influence on Transport in the JET Tokamak* PhD Thesis, University of London 1995

[Hawkes et al 1995] NC Hawkes, DV Bartlett, N Deliyanakis, N Peacock, L Porte, A Rookes, 22^{nd} EPS on Controlled Fusion and Plasma Physics, Bournemouth (1995)

[Hayward et al 1989] RJ Hayward, PJ Crawley, RT Crossland, BS Ingram, AP Pratt, RTC Smith, Proc 15^{th} Symp Fusion Tech Utrecht The Netherlands Elsevier Press North Holland **1** 361 (1989)

[Hender et al 1992] TC Hender, R Fitzpatrick et al, Nuclear Fusion **32** 12 2091 (1992)

[Henke et al 1993] BL Henke, EM Gullikson, JC Davis, Atomic Data and Nuclear Data Tables **54** 2 181 (1993)

[Henry 1981] RJW Henry, Phys. Rep. **68** 1 (1981)

[Hinton and Hazeltine 1976] FL Hinton, RD Hazeltine, Review of Modern Physics **48** 2 239 (1976)

[Hopcraft 1993] KI Hopcraft, *Magnetohydrodynamics* chapt 4 from *Plasma Physics An Introductory Course* ed RO Dendy, Cambridge University Press (1993)

[Hulse 1983] RA Hulse, Nuclear Technology / Fusion **3** 259 (1983)

[Hutchinson 1987] *Principles of Plasma Diagnostics* IH Hutchinson Cambridge University Press (1987)

[Isler 1984] RC Isler, Nuclear Fusion **24** 12 1599 (1984)

[JET Team 1988] JET Team, Plasma Physics and Controlled Nuclear Fusion Research 1988 (Proc. 12^{th} Int. Conf. Nice 1988) Vol 1, IAEA, Vienna (1989)

[Johann 1931] HH Johann, Z. Phys. **69** 185 (1931)

[Kadota et al 1980] K Kadota, M Otsuka, J Fujita, Nuclear Fusion **20** 209 (1980)

[Källne et al 1983] E Källne, J Källne, AK Pradhan, Physical Review A **27** 3 1476 (1983)

[Källne et al 1984] E Källne, J Källne, P Richard, M Stöckli, Journal of Physics B **17** L115 (1984)

[Karzas and Latter 1961] W Karzas, J Latter, The Astrophysical Journal Supplement **6** 167 (1961)

[Keenan et al 1987] FP Keenan, SM McCann, AE Kingston, Physica Scripta **35** 432 (1987)

[Kim et al 1991] YB Kim, PH Diamond, RJ Groebner, Physics of Fluids B **3** 8 2050 (1991)

[Kim et al 1994] J Kim, KH Burrell, P Gohil, RJ Groebner, YB Kim, HE St John, RP Seraydarian, MR Wade, Physical Review Letters **72** 14 2199 (1994)

[Kirz et al 1986] *X-Ray Data Booklet* Lawrence Berkely Laboratory, University of California, Berkely, California 94720 Editor D Vaughan (1986)

[Krause and Oliver 1979] MO Krause, JH Oliver, J. Phys. Chem. Ref. Data **8** 2 329 (1979)

[Kurki-Suonio et al 1992] TK Kurki-Suonio, RJ Groebner, KH Burrel, Nuclear Fusion **32** 1 133 (1992)

[Lawson 1957] JD Lawson, Proc. Phys. Soc. **70** pt 1 no 445 B 6-10 (1957)

[Massey 1975] BS Massey, *Mechanics of Fluids* Van Nostrand Reinhold (1975)

[McCarthy and Zurro 1995] KJ McCarthy, B Zurro, 22^{nd} EPS on Controlled Fusion and Plasma Physics, Bournemouth, (1995)

[McWhirter 1981] RWP McWhirter *Plasma Radiation* chapt 10 from *Plasma Physics and Nuclear Fusion Research* ed RD Gill Academic Press (1981)

[Mohr 1983] PJ Mohr, Atomic Data and Nuclear Data Tables, **29** 3 453 (1983)

[O Mullane 1994] MG O Mullane, Private communication (1994)

[Osborne 1990] TH Osborne et al, Nuclear Fusion **30** 10 2049 (1990)

[Parkinson 1972] JH Parkinson, Nature Phys. Sci. **236** 68 (1972)

[Peacock et al 1994] NJ Peacock, R Barnsley, IH Coffey, SJ Fielding, IM Melnick, MG O Mullane, A Patel, MA Singleton, M Valovic, 21^{st} EPS on Controlled Fusion and Plasma Physics, Montpellier, **18B** 1 134 (1994)

[Peacock et al 1995] NJ Peacock, MA Singleton, R Barnsley, SJ Fielding, NC Hawkes, IM Melnick, MG O Mullane, A Patel, M Valovic, 22^{nd} EPS on Controlled Fusion and Plasma Physics, Bournemouth, (1995)

[Phillips et al 1994] KJH Phillips, FP Keenan, LK Harra, SM McCann, E Rachlew-Källne, JE Rice, M Wilson, Journal of Physics B **27** 1939 (1994)

[Platz et al 1995] P Platz, M Mattioli, F Sattin 22^{nd} EPS on Controlled Fusion and Plasma Physics, Bournemouth (1995)

[Pradhan 1985] AK Pradhan, The Astrophysical Journal **288** 824 (1985)

[Salem and Lee 1976] SI Salem, PL Lee, Atomic Data and Nuclear Data Tables **18** 3 233 (1976)

[Sändstrom 1957] AE Sändstrom, *Experimental Methods of X-Ray Spectroscopy: Ordinary Wavelengths* in Handbuch der Physik, ed S Flügge, 30 78 Springer-Verlag, Berlin (1957)

[Seguin 1983] FH Seguin, R Petrasso, ES Marmar, Physical Review Letters **51** 6 455 (1983)

[Silver et al 1982] EH Silver, M Bitter, K Brau, D Eames, A Greenberger, KW Hill, DM Meade, W Roney, NR Sauthoff, S Von Goeler, Review of Scientific Instruments **53** 8 1198 (1982)

[Spitzer 1962] L Spitzer Jr., *Physics of Fully Ionised Gasses* Wiley (1962)

[Stratton 1965] TF Stratton, *X-Ray Spectroscopy* chapt 8 from *Plasma Diagnostics and Techniques* (ed RH Huddlestone and SL Leonard) Academic Press (1965)

[Stringer 1993] TE Stringer, *Transport in Magnetically Confined Plasmas* chapt 14 from *Plasma Physics An Introductory Course* ed RO Dendy, Cambridge University Press (1993)

[Suckewer et al 1981] S Suckewer, HP Eubank, RJ Goldston, J McEnerney, NR Sauthoff, HH Towner, Nuclear Fusion **21** 10 1301 (1981)

[Summers 1994] Atomic Data and Analysis Structure User manual Jet Joint Undertaking (1994)

[Thorne 1988] AP Thorne, *Spectrophysics* Chapman and Hall, Second edition (1988)

[Tudor Davis and Vaughan 1963] J Tudor Davis, JM Vaughan, The Astrophysical Journal **137** 1302 (1963)

[Vainshtein and Safronova 1978] LA Vainshtein, UI Safronova, Atomic Data and Nuclear Data Tables **21** 1 49 (1978)

[Vainshtein and Safronova 1980] LA Vainshtein, UI Safronova, Atomic Data and Nuclear Data Tables **25** 4 311 (1980)

[Van Regemorter 1962] H Van Regemorter, The Astrophysical Journal **136** 906 (1962)

[Von Goeler et al 1975] S Von Goeler, W Stodiek, H Eubank, H Fishman, S Grebenshshikov, E Hinnov, Nuclear Fusion **15** 301 (1975)

[Von Hamos 1933] L Von Hamos, Ann. Phys **17** 716 (1933)

[Wagner et al 1982] FG Wagner et al, Physics Review Letters **49** 1408 (1982)

[Wells and Pounds 1993] A Wells, K Pounds, Physics World **6** 5 32 (1993)

[Wesson 1987] *Tokamaks* J Wesson Oxford Clarendon Press (1987)

[White 1950] JE White, Journal of Applied Physics **21** 855 (1950)